
Theoretical and Computer Simulation of 2D / 3D Hard Core Mixtures

Author:

**Owen Daniel
Pandaram**

Supervisor:

Dr Giuseppe Pellicane

Submitted in fulfillment of the academic requirements for the degree of Master of Science in the
School of Chemistry and Physics, University of KwaZulu Natal, Pietermaritzburg

November 19, 2014

As the candidate's supervisor I have/have not approved this thesis/dissertation for submission.

Signed: _____

Name: Dr Giuseppe Pellicane

Date: _____

Abstract

The main focus of this research was on the numerical study of liquid-liquid phase coexistence in systems of nonadditive hard-sphere mixtures (NAHSMs) and systems of nonadditive hard-disk mixtures (NAHDMs). Many techniques for studying phase separation exist, however the Gibbs ensemble Monte Carlo (GEMC) method represents both a versatile and suitable approach to study phase separation without the bias deriving from the presence of an interface between the two co-existing phases. Application of the GEMC method to a binary hard-sphere / hard-disk mixture is not a trivial task, as it involves the extension of its algorithm to a system of interacting particles consisting of two different species, which was an endeavour successfully achieved by us in the time-frame of several months, including code testing against results reported in the scientific literature for well-known microscopic models of statistical mechanics. In the case of NAHSMs, we focused on generating an extensive set of computer simulation data over a range of size ratios and non additivity parameters. These data provide a useful benchmark for existing statistical-mechanical theories and would also function as a reference to assess future theoretical contributions. Specifically, the application of GEMC to NAHSMs allowed us to show that Integral Equation Theories (IETs), and classical Density Functional Theory (DFT) are semi quantitatively accurate, while the method of the zero of the Residual Multi-Particle Entropy when supplemented by computer simulation data is quantitatively accurate, as reported in a paper we have published in the *Journal of Chemical Physics* (**141**, 044508 (2014)). For NAHDMs, in collaboration with a research group in Italy, we adopted Monte Carlo integration methods to calculate the fifth virial coefficient and subsequently used these estimates in order to build the virial equation of state (EOS), along with scaled and modified variants. In order to assess the validity of the EOS, constant-NVT ensemble Monte Carlo simulations were performed. Finally, the GEMC method was applied for a wide range of nonadditive parameters in order to evaluate the demixing curves, and these data were used to assess the corresponding theoretical predictions obtained from the equations of state. These results

are reported in another paper, recently accepted for publication in the *Journal of Chemical Physics* (048445JCP, 2014).

Contents

List of Figures	vi
List of Tables	x
1 Introduction	1
2 Understanding the Nature of Phase Transitions	7
2.1 Phase transitions and metastable thermodynamic states	7
2.1.1 First Order Phase Transition	9
2.1.2 First Order Verses Second Order Phase Transitions	10
3 Monte Carlo Computer Simulation	12
3.1 The Monte Carlo Method	12
3.1.1 Importance Sampling and the Metropolis Method	13
3.1.2 Monte Carlo Algorithm	17
3.2 Gibbs Ensemble Monte Carlo Method	19
3.2.1 Acceptance Rules	20
3.2.2 Extension of the Acceptance Rules to a Binary Mixture	22
3.2.3 Case Study: GEMC applied to a Particles in a Square Well Potential	26
4 Building the Gibbs Ensemble Monte Carlo code	31
4.1 Particle Exchange: The Constant-NVT Ensemble Test	31
4.1.1 Symmetric mixture with non-additive parameter $\Delta = 0.2$	32

4.1.2	Asymmetric mixture with non-additive parameter $\Delta = 0.0$	34
4.2	Particle Insertion: The Constant-NPT Ensemble Test	35
4.2.1	The Chemical Potential μ and the Widom method	37
4.2.2	Relating the Constant-NPT Ensemble Monte Carlo Results to a GEMC without Volume Changes	39
4.2.3	Symmetric mixture with non-additive parameter $\Delta = 0.2$	40
5	Gibbs Ensemble Monte Carlo of Nonadditive Hard-Sphere Mixtures	41
5.1	Theory	41
5.2	Results and Discussion	46
5.3	Conclusion	66
6	EOS and GEMC of Nonadditive Hard-Disk Mixtures	67
6.1	Virial expansion	67
6.2	Monte Carlo simulation	69
6.3	Results and Discussion	70
6.4	Conclusion	81
7	Bibliography	82

List of Figures

2.1	Vapour Phase	8
2.2	A first order phase transition as depicted by a shifting in the equilibrium from one local minimum to the other	9
2.3	11
2.4	Gibbs potential verses the molar volume to show the coalescence of minima with increasing temperature T	11
3.1	Density ($\rho\sigma^3$) vs number of cycles for a temperature above the critical temperature	28
3.2	Density ($\rho\sigma^3$) vs number of cycles for a temperature at critical temperature	29
3.3	Density ($\rho\sigma^3$) vs number of cycles for a temperature below the critical temperature	29
3.4	The vapour-liquid coexistence curves for hard-sphere particles interacting with a square well potential $\lambda = 1:25$ (a), $\lambda = 1.5$ (b)	30
5.1	Fluid-fluid coexistence in the reduced total density-composition diagram for a symmetric mixture with $\Delta = 0.1$. Red circles with error bars: GEMC data - present work. Green triangles with error bars: GEMC data of Ref. [39]. Dotted line: MIX1 theory. Dashed line: EOS1N.	47
5.2	Fluid-fluid coexistence in the reduced total density-composition diagram for a symmetric mixture with $\Delta = 0.2$. Red circles with error bars: GEMC data - present work. Green triangles with error bars: GEMC data of Ref. [51]. Dotted line: MIX1 theory. Dashed line: EOS1N.	49

5.3	Fluid-fluid coexistence in the reduced total density-composition diagram for for an asymmetric mixture with $y = 0.83$, $\Delta = 0.183$. Red circles with error bars: GEMC data - present work. Green triangles with error bars: GEMC data of Ref. [39]. Dotted line: MIX1 theory. Red diamond: GEMC critical point.	50
5.4	Fluid-fluid coexistence in the reduced pressure-density diagram for for an asymmetric mixture with $y = 0.83$, $\Delta = 0.183$. Legend: see Fig. 5.3.	51
5.5	Fluid-fluid coexistence in the reduced total density-composition diagram for an asymmetric mixture with $y = 0.83$, $\Delta = 0.364$. Legend: see Fig. 5.3.	52
5.6	Fluid-fluid coexistence in the reduced total density-composition diagram for an asymmetric mixture with $y = 0.85$, $\Delta = 0.1$. Red circles with error bars: GEMC data - present work. Blue squares with error bars: zero-Residual Multi Particle Entropy ($\Delta S = 0$) of Ref. [20]. Red diamond: GEMC critical point.	54
5.7	Fluid-fluid coexistence in the reduced total density-composition diagram for an asymmetric mixture with $y = 0.75$, $\Delta = 0.1$. Legend: see Fig. 5.6.	56
5.8	Fluid-fluid coexistence in the diagram of the packing fractions of the two species for an asymmetric mixture with $y = 0.75$, $\Delta = 0.1$. Red circles with error bars: GEMC data - present work. Dashed line: MHNC theory. Dot-dashed line: RY theory. Full line: first-order thermodynamic theory. All of the theoretical results taken from Ref. [21]. Diamond: GEMC critical point.	57
5.9	Fluid-fluid coexistence in the diagram of the packing fractions of the two species for an asymmetric mixture with $y = 0.6$, $\Delta = 0.1$. Legend: see Fig. 5.6.	60
5.10	Radial distribution functions for an asymmetric mixture with $y = 0.75$, $\Delta = 0.1$, $\eta_A = 0.0905$, $\eta_B = 0.214$, as a function of reduced distance $r^* = r/\sigma$. Circles: NVT Monte Carlo simulation. Full, red line: MHNC theory. Dashed, blue line: PY theory.	61
5.11	Radial distribution functions for an asymmetric mixture with $y = 0.6$, $\Delta = 0.1$, $\eta_A = 0.061$, $\eta_B = 0.284$ as a function of reduced distance $r^* = r/\sigma$. Circles: NVT Monte Carlo simulation. Full, red line: MHNC theory. Dashed, blue line: PY theory.	62

5.12	Fluid-fluid coexistence in the diagram of the packing fractions of the two species for an asymmetric mixture with $y = 0.5$, $\Delta = 0.2$. Red circles with error bars: GEMC data - present work. Dot-dashed line: DFT of Ref. [29]. Red diamond: GEMC critical point. Blue circle: DFT critical point.	64
5.13	Fluid-fluid coexistence in the diagram of the packing fractions of the two species for an asymmetric mixture with $y = 0.5$, $\Delta = 0.3$. Legend: see Fig. 5.12.	65
6.1	The fifth virial coefficient plotted as a function of the mole fraction for positive values of the nonadditivity parameter Δ	72
6.2	Compressibility factors as a function of the total packing fraction at different values of the Δ parameter and mole fraction x . Legend: SIM represents the NVT MC computer simulation; Zvir3 represents the virial expansion incorporating the first three virial coefficients; Zvir4 represents the virial expansion incorporating the first four virial coefficients; Zvir5 represents the virial expansion incorporating the first five virial coefficients; Zsc3 represents the scaled EOS incorporating the first three virial coefficients; Zsc4 represents the scaled EOS incorporating the first four virial coefficients; Zsc5 represents the scaled EOS incorporating the first five virial coefficients	73
6.3	see Fig. 6.2	74
6.4	see Fig. 6.2	74
6.5	see Fig. 6.2	75
6.6	see Fig. 6.2	75
6.7	Phase coexistence boundary of a symmetric NAHD mixture for different values of Δ . In each panel the solid circles represent GEMC results and the diamond is the estimate of the critical density; the solid red line is the virial expansion truncated to the fifth order; the dashed blue line represents the rescaled virial expansion truncated to the fifth order [93]; the dotted green line is the prediction of the MIX1 implemented with the SPT equation of state for the reference fluid [81]; Open squares represent semigrand canonical Monte Carlo data [87].	78

6.8	Critical density ρ_c plotted as a function of Δ for a symmetric NAHD mixture. The full circles are our GEMC simulations; the cross and the triangle represent the estimate of semigrand canonical ensemble MC simulations for $\Delta = 0.2$ [87] and the estimate of a cluster algorithm for $\Delta = 0.5$ [86], respectively. The solid red line and the dashed blue line are the predictions of the virial and the rescaled virial expansion truncated to the fifth order [93], respectively; The dotted green line is the prediction of the MIX1 implemented with the SPT equation of state for the reference fluid [81].	79
7.1	Cluster Diagram representing Eq. (7.2)	90

List of Tables

4.1	$\beta P/\rho$ and radial distribution functions (g) for hard sphere mixtures with $y = \frac{\sigma_A}{\sigma_B} = 1.00$ for a system of ($N = 256$) particles	33
4.2	$\beta P/\rho$ and radial distribution functions (g) for hard sphere mixtures with $y = \frac{\sigma_A}{\sigma_B} = 1.00$ for a system of ($N = 500$) particles	33
4.3	$\beta P/\rho$ and radial distribution functions (g) for hard sphere mixtures with $y = \frac{\sigma_B}{\sigma_A} = 3.333$, where x_B is the composition of the larger sphere with the system containing ($N = 1728$) particles	34
4.4	Chemical potential $\beta\mu$ results from NPT-Ensemble Monte Carlo simulations. (Lomba et al: Phase stability of binary mixtures) and $\beta\mu$ for both box <i>I</i> and <i>II</i> from GEMC simulation without volume change (Computer Simulation).	40
5.1	GEMC coexistence reduced pressures and chemical potentials of the two species in the two boxes for $y = 0.83$ and $\Delta = 0.182$	48
5.2	GEMC coexistence reduced pressures and chemical potentials of the two species in the two boxes for $y = 0.83$ and $\Delta = 0.364$	53
5.3	GEMC coexistence reduced pressures and chemical potentials of the two species in the two boxes for $y = 0.85$ and $\Delta = 0.1$	54
5.4	GEMC coexistence reduced pressures and chemical potentials of the two species in the two boxes for $y = 0.75$ and $\Delta = 0.1$	55
5.5	GEMC coexistence reduced pressures and chemical potentials of the two species in the two boxes for $y = 0.75$ and $\Delta = 0.1$	58

5.6	GEMC coexistence reduced pressures and chemical potentials of the two species in the two boxes for $y = 0.6$ and $\Delta = 0.1$	58
5.7	GEMC coexistence reduced pressures and chemical potentials of the two species in the two boxes for $y = 0.5$ and $\Delta = 0.2$	59
5.8	GEMC coexistence reduced pressures and chemical potentials of the two species in the two boxes for $y = 0.5$ and $\Delta = 0.3$	59
6.1	The partial coefficients E_{11112} and E_{11122} for a symmetric NAHD mixture tabulated as a function of the nonadditivity parameter $\Delta > 0$. The numerical values are given in units of σ_{11}^8 . The error on the last significant figure is enclosed in parentheses.	71

Preface and Declarations

The work described by this thesis was carried out at the University of Kwazulu-Natal, School of Chemistry and Physics, Pietermaritzburg, from **the first of January 2013** until **the thirty-first of October 2014**, under the supervision of **Dr Giuseppe Pellicane**.

This thesis is entirely, unless specifically contradicted in the text, the work of the candidate, Owen Daniel Pandaram, and has not been previously submitted, in whole or in part, to any other tertiary institution. Where use has been made of the work of others, it is duly acknowledged in the text.

Declaration - Plagiarism

I, Owen Daniel Pandaram declare that

1. The research reported in this thesis, except where otherwise indicated, is my original research.
2. This thesis has not been submitted for any degree or examination at any other university.
3. This thesis does not contain other persons' data, pictures, graphs or other information, unless specifically acknowledged as being sourced from other persons.
4. This thesis does not contain other persons' writing, unless specifically acknowledged as being sourced from other researchers. Where other written sources have been quoted, then:
 - a. Their words have been rewritten but the general information attributed to them has been referenced.
 - b. Where their exact words have been used, then their writing has been placed in italics and inside quotation marks, and referenced.
5. This thesis does not contain, text, graphics or tables copied and pasted from the Internet, unless specifically acknowledged, and the source being detailed in the thesis and in the References section.

Signed:

Declaration - Publications

Details of publications that form part and/or include research presented in this thesis.

1. Title : Gibbs ensemble Monte Carlo of nonadditive hard-sphere mixtures

Authors : Giuseppe Pellicane and Owen D. Pandaram

Status : Published (*Journal of Chemical Physics* (141, 044508 (2014)); doi: 10.1063/1.4890742)

2. Title : Theoretical and computer simulation study of phase coexistence of nonadditive hard-disk mixtures

Authors : Giacomo Fiumara, Owen D. Pandaram, Giuseppe Pellicane and Franz Saija

Status : Accepted for publication in *Journal of Chemical Physics* (048445JCP, 2014)

Signed: _____

Acknowledgments

Firstly I would like to give thanks to my Lord and Saviour Jesus Christ who gave me the strength and dedication needed to embark in a MSc. in Physics program. Also much gratitude and appreciation must be given to my parents, Richard and Charmaine Pandaram who were always there to encourage me throughout my life thus far as well as inspire me to work hard as they have done their entire lives. Next I must thank my mentor / supervisor, Dr Giuseppe Pellicane who has been exceptional in grooming me to be a better post graduate student as well as highly knowledgeable in this field statistical physics and thermodynamics. Without his constant efforts towards superior guidance, the work represented in this thesis would have not being completed on time or be off the same high quality. I would also like to acknowledge Prof F. Saija from the the National Council of Research (CNR) of Italy, and Prof G. Fiumara from the University of Messina, Italy for their support and guidance during the scientific collaboration with us. Also a special mention about Claudio, Pellicano and Mariuccia. These three servers / workstations where there through it all working tirelessly to run the simulations and store all the relevant data without being corrupted or crashing. Another special mention is given to the staff of the UKZN physics department in Pietermaritzburg. All the academic and support staff have contributed considerably to my personal development and have been most helpful whenever they are called upon for assistance or advice. Last but not least, I give the utmost thanks to National Institute of Theoretical Physics (NITheP) for financial support throughout my Honours and MSc. years. The prestigious backing and support gave me a sense of belonging as well as inspired me to contribute to the available knowledge in the fields of theoretical and computational physics.

Chapter 1

Introduction

The study of the phase behavior of fluid mixtures is of great importance. From designing separations in the pharmaceutical and chemical industry, to understanding climate change and fundamental biological processes. Despite having a good availability of experimental data [1] for systems that consist of more than one component, these results are published for limited ranges of temperature, pressure and composition only. If we consider that experiments can also be time-consuming and expensive, we understand the reason why so more often than not we turn to the aid of computer simulation when studying phase coexistence of fluid systems.

Before the advent of computer simulation, determining the structural and thermodynamic properties of a system consisting of many atoms / molecules was based on formulating a microscopic theory for the selected model of particle interactions. Theoretical applications providing an exact analytical or numerical solution are however limited to a very few specialized cases (eg: Ideal gas, lattice models). A basic model for liquids is the hard-sphere model, that at the beginning was extensively studied also with the aid of mechanical simulation of steel ball bearings [2, 3, 4]. With the advent of electronic computers, it became possible to look for an exact numerical solution to any model of particle interactions, at least in principle. This paved the way to the study of dense liquids, and the first computer simulation of the hard-sphere model was carried out by Metropolis, Rosenbluth, and Teller on the MANIAC computer at Los Alamos laboratories [5] in 1953. The Metropolis Monte Carlo method, which made use of a weighted random walk, was introduced for

the first time. Monte Carlo (MC) methods together with Molecular Dynamics (MD) have since been the techniques of choice when simulating liquid systems.

With the aid of computer simulation we could compare exact results for the chosen model to those as obtained from the direct experiment of the system to which the model is referred to. If there were any discrepancies, the model could then be adjusted. However, any new theory is seldom applied to a realistic model of particle interactions without first testing it against computer simulation for more simplified models. The reason is that a statistical-mechanical theory always provides an approximate prediction for the structural and thermodynamic properties of the model, whereas computer simulation gives an exact result for them within the chosen model and statistical error as originated from, respectively, the finite duration of the simulation and size of the system (total number of particles adopted).

The structural properties of real dense fluids depend mainly on short ranged repulsive intermolecular forces, which are adequately accounted for by hard-core models. In these models, molecules do not interact at separations larger than the hard sphere diameter and experience infinite repulsion if their separation is less than that distance. Two simple but still not trivial models of interest for binary fluids that we will consider in this thesis are hard-sphere mixtures as well as hard-disk mixtures. Both of them are an important reference system for perturbation theories [6], which treat attractive long-range interactions as a perturbation [7], and they can be used to model the behaviour of many real phenomena.

The hard-sphere model can be easily generalized to binary mixtures, consisting of two components with different diameters [8]. When the distance of closest approach between different species is not equal to the trivial average of the diameters of the two species, the model system is called a nonadditive hard-sphere mixture (NAHSM). When there is an extra-repulsion between the two species, i.e. when the distance of closest approach between unlike species is larger than the arithmetic mean, and for a high enough density of the mixture, a NAHSM is known to demix into two phases at different compositions of the two species. For this model, temperature becomes an irrelevant parameter and phase separation occurs when the mixed state is entropically disfavored so that the free-energy minimum (entropy maximum) is only attainable for a demixed state. The NAHSM

model is particularly relevant to ionic systems [9], metallic systems [10], aqueous electrolyte solutions [11], mixtures of colloidal particles and polymers [12, 13], and rare-gas mixtures in extreme thermodynamic conditions [14, 15]. Obviously, the NAHSM represents a highly idealized model to understand the effect of crossed interactions between different species of a fluid mixture beyond the geometrical distances imposed by steric interactions. These interactions are captured by the model only in terms of their extra-repulsive range (positive nonadditivity) or extra-attractive magnitude (negative nonadditivity), while their nature and specific details depend on the considered system.

Besides its relevance to experimental systems, the binary NAHSM is a basic model mixture of statistical physics able to exhibit a fluid-fluid phase separation. Then, it is not surprising that it has been intensively studied since the late sixties, when an analytical solution for its correlation functions was obtained for the first time by Lebowitz and Zomick within the Percus-Yevick theory [16, 17]. Demixing in NAHSMs has been widely studied theoretically by using integral-equation theories [18, 19, 20, 21, 22], scaled particle theory [23, 24], analytical equations of state [28, 56, 25, 26, 27], classical density-functional theory [30, 29], or effective depletion potentials [31, 21]. Phase transitions of NAHSMs had also been investigated in a number of confined geometries, including slit-pores [32, 33], cylindrical pores [34], and random pores [35, 36, 26, 37]. Even demixing in ternary NAHSMs was investigated by the means of integral-equation theories [38]. Given the importance of the NAHSM binary model in statistical physics, one would expect that a proper amount of computer simulation data are reported in the literature in order to allow a fair assessment of liquid-state theories, especially when it comes at phase coexistence properties. In fact, fluid-fluid phase coexistence was extensively investigated for *symmetric* binary NAHSMs, i.e. for two species having the same diameter, with Gibbs ensemble Monte Carlo (GEMC) [39], semi-grand ensemble Monte Carlo (SGCMC [40, 41]), and by using the zero of the one-phase residual multi-particle entropy (zero-RMPE) [19, 42, 20]. On the other hand, demixing in the asymmetric regime, i.e. when the two species possess different diameters, was never investigated thoroughly, and only a few cases were considered in the literature for medium [39] and extremely high size asymmetry [43]. The zero-RMPE approach was also applied to *asymmetric* mixtures, but since its predictions are not based on a true computer simulation of phase coexistence, they also need to

be assessed against a method explicitly taking into account the free energies of the two coexisting phases.

The nonadditive hard-disk mixture (NAHDM) is a model relevant to fluid mono-layers. Phase separation has been observed experimentally in mixtures of rare-gases physisorbed on graphite [67, 68, 69]. In colloidal science, it has been shown that the interaction of two water-solvated polymers can be mapped onto a nonadditive hard-disk model [70]. The phenomenon of inhibition of asphaltene flocculation was also showed to be captured by the same model [71]. In very recent years, NAHDMs have been successfully applied to model mono / bi-layers of ganglioside / phospholipid lipid mixtures [72]. While for NAHDMs there are plenty of results published in the literature, only a few theoretical and computational studies were reported even for symmetrical NAHD mixtures. Dickinson [58, 59] reported molecular dynamics simulations of NAHD mixtures in which he computed the compressibility factor and the radial distribution functions for a few size ratios and some nonadditivities. A scaled-particle theory (SPT) was devised by Tenne and Bergmann [73], and that was subsequently improved by Bearman and Mazo [74] and successfully applied to describe fluid-fluid phase coexistence for the case of extra-repulsion between unlike species [75, 76]. The modified SPT equation of state (EOS) for a two-dimensional model mixture of hard-soft spheres [77] was also assessed against MD and MC computer simulations. Another self-consistent EOS for NAHDMs was assessed against MD data in a wide range of ratios of hard-disk diameters (1 to 4 [78, 79]). However, in the latter case the theoretical EOS proved to be reliable only in the additive case and for relatively small values of extra-repulsion between the two chemical species. The MIX1 approximation, that is a first-order thermodynamic perturbation theory, was found reliable for symmetric nonadditive hard-sphere mixtures [80], and also adopted to predict fluid-fluid phase separation for a limited number of selected values of extra-repulsion between unlike species [20]. A comprehensive theory for the characterization of the EOS of nonadditive hard-spheres for an arbitrary number of species (and also for arbitrary dimension, i.e. 2D, 3D, etc.) was reported by Santos *et al.* [82]. More recently, the fourth virial coefficient of *symmetric* NAHDMs was reported by Saija [83]. The same author also provided some predictions of the fluid-fluid coexistence curves by exploiting the calculated virial coefficient and assessed them against the available computer

simulation data reported in the literature. In a more recent article the fourth virial coefficient in the asymmetric case (size ratio $y = \sigma_2/\sigma_1$ different from unity) was used to assess the merits and limitations of some theoretical approaches. The GEMC method has been extensively applied to symmetric NAHD mixtures to predict fluid-fluid phase separation [85, 84] in the symmetric case only (no extra-repulsion between different species), as well as an application of a cluster algorithm within it, which allowed the author to study systems consisting of an extremely large number of particles [86]. However, the mentioned studies were accomplished in a limited range of extra-repulsion between unlike species, and for relatively high values of it. Another computer simulation study of fluid-fluid phase separation was conducted by Munoz-Salazar and Odriozola within the semigrand canonical ensemble MC and for a single value of extra-repulsion [87].

The chapters to come are structured as follows. Chapter 2 introduces the reader to the theory and basic scientific principles concerning phase transitions. Phase diagrams are explained in detail with differentiation between first order and second order phase transitions. In chapter 3 we adopt statistical mechanics to relate the basic way in which particles interact to various thermodynamic quantities, when the system is in thermodynamic equilibrium. The basic principle behind MC computer simulation is discussed as well as how it is adapted to the case of phase coexistence in the framework of the GEMC method. A case study of GEMC applied to hard-sphere particles interacting with a square well potential is used to demonstrate the GEMC method as well as its effectiveness. Chapter 4 deals with construction of a GEMC code applied to a binary hard-sphere system and the various stages of testing in the framework of different statistical ensembles as to ensure that the code output was in good agreement with data reported in the literature. In chapter 5, the goal was to provide novel GEMC data mainly for asymmetric NAHSMs, and assess the performance of some theoretical results available in the literature for the fluid-fluid phase coexistence. Our effort resulted in the production of some important benchmarks for improvements of some well-known or potentially new statistical-mechanical theories. Finally in the last chapter, following reduction of the dimension of the system to two in the code, we used GEMC computer simulations to study the fluid-fluid phase separation of a *symmetric* NAHD mixture for a number of values of the nonadditivity parameter Δ , where the latter is used to quantify the degree of extra-

repulsion between the two different species (see next chapters). At the same time, in collaboration with Prof.s S. Saija and G. Fiumara, we calculated the computation of the fifth virial coefficient evaluating numerically - by using integration MC methods - the independent irreducible cluster integrals. From the knowledge of these coefficients, the virial expansion can be resummed so that a new equation of state is constructed, that was separately assessed against novel NVT MC simulations. Then, starting from the EOS the Helmholtz free energy of the model can be easily calculated analytically, and by applying the standard thermodynamic conditions of phase coexistence to it, the fluid-fluid phase separation boundaries and the location of the critical points as a function of Δ can be predicted. Finally, these predictions were assessed against GEMC results.

Chapter 2

Understanding the Nature of Phase Transitions

2.1 Phase transitions and metastable thermodynamic states

A phase transition is defined as a precipitous change in the properties of a substance. Hence there is a definite loss of homogeneity of the substance. An example of this would be liquid water at room temperature and atmospheric pressure. If it experiences a change in temperature such that it is cooled below 273.15 K, it will solidify. Likewise if liquid water is heated above a temperature of 315.15 K, it evaporates. There is also a modification in the properties of a material if it undergoes changes in pressure or some other thermodynamic parameter. This is again seen in ice where high pressure causes phase transitions from one solid structure to another one. We distinguish these water phases by their thermodynamic properties such as the molar heat capacity and compressibility, as well as their different crystal structures. When looking at the thermodynamic potential as a function of the related thermodynamic parameters (e.g. Helmholtz free energy versus molar volume or Gibbs free energy versus thermodynamic pressure), we can easily view phase transitions as boundaries of regions of a thermodynamic diagram (e.g. P versus V or T versus particle density ρ) in which there is a failure of the thermodynamic stability criteria. We will see in the next section that the two phases that form on either end of a first order phase

transition are distinct, and found at separate regions of the thermodynamic plane. To understand

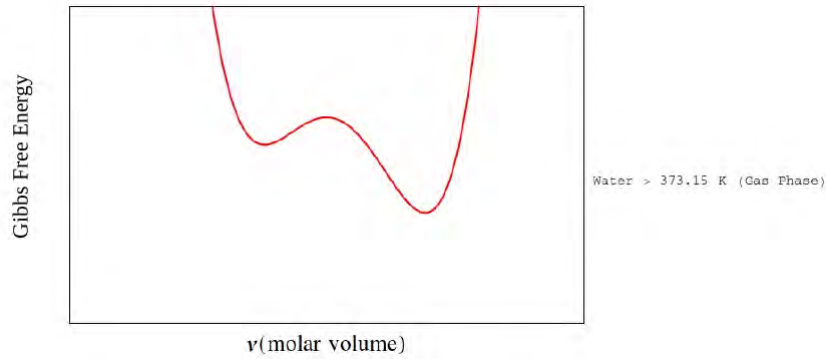


Figure 2.1: Vapour Phase

a phase transition by the thermodynamic point of view, let us examine a system that consists of a vessel of water vapour at a pressure of 1 atmosphere and a temperature above 373,15 K (that is above the boiling point of water). For the sake of clarity, we shall consider the subsystem to consist of a spherical region of water vapour that is equivalent to a small quantity of water. Then, this small subsystem will have its temperature and pressure equal to the corresponding values of the remaining (and much larger) amount of water in the vessel, which will be equivalent to a pressure and thermal reservoir. We note that for a system in contact with a pressure and thermal reservoir, the condition of equilibrium is that the Gibbs potential ($G(T, P, N)$) be a minimum, where the Gibbs potential is dependent on the temperature, pressure and number of particles of the system. For the given subsystem the Gibbs potential has the form as seen in Fig. 2.1, where the system is stable for the lower minimum which corresponds to the vapour phase. From the inspection of Fig. 2.1, the absolute minimum corresponds to a larger volume (smaller density) as compared to the local minimum. If we were to introduce an instantaneous perturbation into the subsystem, the intensive parameter represented by the pressure would act as a restoring force that would drive the system back to homogeneous state. This is because the slope of the curve in Fig. 2.1 is the pressure. Consider a perturbation that is large enough to overcome the local maximum and bring the system in the region of the secondary local minimum (metastable state). The counterpart of this metastable state in the reality can be seen in gases when high density droplets occur for a limited time lapse, before vanishing. The reason for this is the shallow difference in the energy

barrier, which makes it likely to be frequently overrun by small perturbations, forcing the system to return to the more stable state corresponding to the lower, absolute minimum.

2.1.1 First Order Phase Transition

Suppose we lower the temperature of the system. The shift in the equilibrium from one local minimum to the other constitutes a first order phase transition which is determined either by a change in temperature or some other thermodynamic parameter. This mechanism is sketched in Fig. 2.2 where we report the Gibbs free energy as a function of the molar volume of the system. It is important to note how the Gibbs potential modifies when the temperature of the system is changed. At the higher temperature T_5 , we see that the vapour phase is the thermodynamically stable phase (absolute minimum), however as we decrease the temperature to T_4 , we note that the depth of the minimum corresponding to the vapour phase (local minimum) decreases whilst the depth of the liquid phase increases until we reach a condition of equal depth at temperature T_3 . T_3 is the temperature at which a phase transition occurs. As the vapour is gently cooled, its free energy changes so as to make it metastable (below T_3 the nature of the vapour minimum changes from global to local one), and at temperatures much lower than T_3 the free energy barrier separating the two minima will be so high that a new thermodynamic stable state will occur with the forming of a condensed liquid. The latter could, for instance, correspond to temperature T_1 , where the free energy minimum of liquid phase is much lower than the one of the vapour phase.

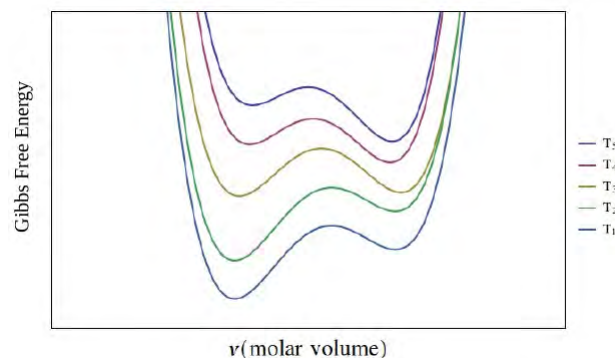
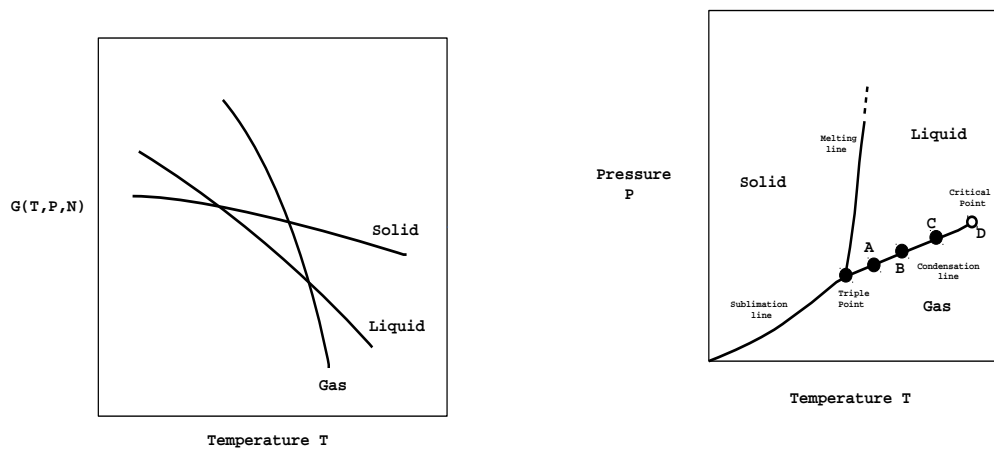


Figure 2.2: A first order phase transition as depicted by a shifting in the equilibrium from one local minimum to the other

2.1.2 First Order Verses Second Order Phase Transitions

When we plot the values of the Gibbs potential at its minima against the temperature, the following observations can be made. The thermodynamically stable phase in Fig. 2.3a corresponds to the lower envelope of the Gibbs potential curves because that is the condition for the system to be in thermodynamic equilibrium. Then, the discontinuities in the slope of the Gibbs free energy corresponding to the thermodynamically stable phase are just discontinuities in the entropy of the system (the entropy is the partial derivative of the Gibbs potential with respect to the temperature). The sketch shown in Fig. 2.3a represents just a section of the full Gibbs free energy surfaces for the different phases (Gas, Liquid, Solid) at a given pressure. If we imagine to add an additional dimension to that figure so to include also the dependence of the Gibbs free energy on the pressure, the intersection points of the different phases would become lines in the G-T-P cartesian space, and the projection of these curves into the pressure-temperature plane, would give us the phase diagram as seen in Fig. 2.3b. Phase diagrams are representations of regions of a thermodynamic plane where a substance is in a thermodynamically stable phase. The different phases are partitioned by first order phase transition lines which indicate regions in which the system is coexisting into two distinct phases. Phases are indicated by their names and special points of note are called the triple point and critical point. At a first order phase transition, the molar Gibbs potentials are equal, and all the other molar potentials are in general discontinuous across the transition, since the discontinuity in the first-order derivatives of the thermodynamic potentials is the defining attribute of first order phase transitions. However, even if the equality of molar potentials is unlikely, it can still occur by coincidence. Consider moving across the liquid-gas coexistence curve (condensation line) away from the solid phase. As Fig. 2.4 shows, the discontinuities in the molar volume and molar energies become smaller as the temperature increases. Finally at the critical point, the two phases become indistinguishable and the first order transition degenerates into a second order phase transition. When a second order phase transition is reached, the second order partial derivatives of the Gibbs free energy become discontinuous since they can be directly related to the discontinuity / divergence of thermodynamic quantities as the specific heat at constant pressure c_P , the coefficient of thermal expansion α , or the isothermal compressibility at constant

pressure χ_T .



(a) Phase diagram of water in the pressure-temperature representation

(b) Minima of the Gibbs potential as a function of the temperature depicting a first order phase transition

Figure 2.3

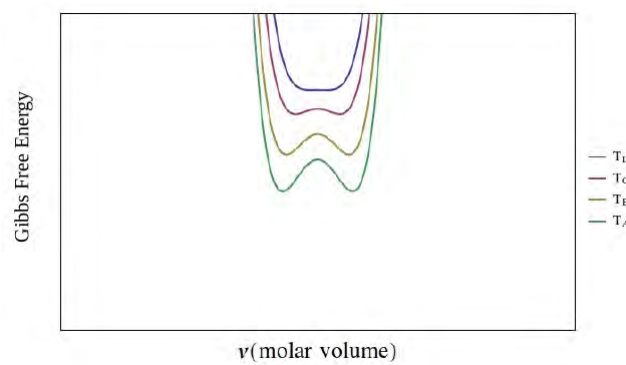


Figure 2.4: Gibbs potential versus the molar volume to show the coalescence of minima with increasing temperature T

Chapter 3

Monte Carlo Computer Simulation

3.1 The Monte Carlo Method

With the previous chapter in mind, it is our aim to provide some comments about how thermodynamic quantities, which are linked to particle interactions by the means of statistical mechanics, can be determined in computer simulations of classical fluids. The two most common, computer simulation techniques are Molecular Dynamics (MD) and Monte Carlo (MC). The basis of MD simulations is that time averages are measured in an ensemble where the energy and momentum are constants of motion. This ensemble is commonly the microcanonical ensemble, however MD simulations can be extended to other ensembles, as e.g. those at constant temperature or constant pressure. MC simulations generate random walks in weighted regions of phase space as to calculate the ensemble averages, where some of the most commonly used ensembles include the canonical (constant-NVT), grand canonical, isobaric-isothermal and Gibbs ensemble. Depending on the ensemble adopted, both MD and MC simulations will have tiny differences in the statistical averages of the thermodynamic quantities computed because of the different magnitude of the associated mean-square fluctuations in finite-size systems. Since MC is our method of choice, we will next explain the basic principles behind it by considering it within the standard constant-NVT ensemble, where N is the total number of particles, V is the volume, and T is the temperature of the statistical ensemble of systems.

The partition function of the constant-NVT ensemble is given by

$$Q = \frac{1}{h^{3N} N!} \int \int d\mathbf{p}^N d\mathbf{r}^N \exp[-H(\mathbf{r}^N, \mathbf{p}^N)/k_B T]. \quad (3.1)$$

Where \mathbf{p}^N and \mathbf{r}^N are the position and momenta of all N particles. $H(\mathbf{r}^N, \mathbf{p}^N)$ is the Hamiltonian of the system which is used to describe the total energy of the system in terms of the kinetic (K) and potential (U) energies:

$$H = K + U \quad (3.2)$$

Suppose we wanted to calculate any statistical average, let us say in this case for some observable A declared in terms of momenta and coordinates. That would be given by

$$\langle A \rangle = \frac{\int d\mathbf{p}^N d\mathbf{r}^N A(\mathbf{r}^N, \mathbf{p}^N) \exp[-\beta H(\mathbf{r}^N, \mathbf{p}^N)]}{\int d\mathbf{p}^N d\mathbf{r}^N \exp[-\beta H(\mathbf{r}^N, \mathbf{p}^N)]}. \quad (3.3)$$

Where $\beta = \frac{1}{k_B T}$. Since H is dependent on K which is in turn a quadratic function of the momentum p , the analytical calculation of the integral involving the momenta is easily computed. The complication is the evaluation of averages of the function $A(\mathbf{r}^N)$ since carrying out multidimensional integration is exceptionally difficult and there are a very few cases in which there is an exact analytical solution. Let us assume that we have to use a numerical technique to evaluate the above function. A simplistic method of calculating the above integral by numerical quadrature seems like a possible solution. If we want to evaluate the integrand for a network (mesh) of points in the $3N$ hyperspace configuration. Even for 100 particles the total number of points would become astronomical (10^{300}) and computations this large cannot be performed. The solution to this problem lies in noting that the Boltzmann factor is essentially zero in most of the configurational space of the system. Thus sampling the entire hyperspace would be a wasteful task. So by sampling configurations where the probability density is very high and the Boltzmann factor is substantially different from zero yields a sound strategy. A sound technique to achieve such *Importance* sampling is the Metropolis Method.

3.1.1 Importance Sampling and the Metropolis Method

If we want to calculate the integral of

$$i = \int_a^b g(y) dy. \quad (3.4)$$

Where i denotes an average of $g(y)$ that is unweighted over the one-dimensional continuation / interval between end points a and b . In conventional MC, the above integral would be evaluated by choosing randomly many y values in the $[a, b]$ interval, and then determining the value of $g(y)$ at each of these points. Let us assume that function $g(y)$ is non-zero only on some regions of the interval $[a, b]$. In the light of evaluating integrals as the one reported in Eq. (3.3), this is equivalent to the aim of sampling a small region of the configurational space, where the Boltzmann factor is considerably different from zero. In the case of Eq. (3.4), we want to sample points distributed in a non-uniform manner according to some weighting function $h(y)$, instead of randomly selecting y values. Then we can rewrite Eq. (3.4) as

$$i = \int_0^1 dy h(y) \frac{g(y)}{h(y)}. \quad (3.5)$$

If we assume that $h(y)$ is a derivative of a normalized, positive, and non-decreasing function $v(y)$, then i becomes

$$i = \int_0^1 dv \frac{g(y(v))}{h(y(v))}. \quad (3.6)$$

Applying the above method to the integrand in Eq. (3.3), we would have to choose $h(y)$ such that the Boltzmann factor is proportional to it. With this in mind, it is unfortunate that the above described technique fails for multidimensional integrals over configuration space due to failure to build a weight function such that the Boltzmann factor is proportional to it. Metropolis *et al*, noted that even if we do not know the absolute probability density

$$\mathcal{N}(\mathbf{r}^N) = \frac{\exp[-\beta U(\mathbf{r})^N]}{Z}, \quad (3.7)$$

where \mathcal{N} is the probability density of a system with a configuration \mathbf{r}^N and Z is the configurational part of the partition function Q :

$$Z = \int d\mathbf{r}^N \exp[-\beta U(\mathbf{r})^N], \quad (3.8)$$

we can always calculate the relative probability of two arbitrary configurations for the system, since that will be just given by the ratio of the two absolute probability densities Eq. (3.7), i.e. the Boltzmann factor of the energy difference between the new and the old configurations. This happenstance provides us with the possibility to calculate integrals as the one reported in Eq. (3.3). In order to better understand why this becomes feasible, let us consider for the sake of illustration the example of measuring the dept of the Nile by means of a conventional quadrature scheme and by an importance-weighted random walk. This illuminating example is reported in the Frenkel and Smit textbook [103]. In conventional quadrature the value of the integrand is measured at a predetermined set of points. Many of these points are situated in regions where the integrand is zero. (i.e. not sampling the Nile river). However, using an Importance weighted random walk / Metropolis method, a trial move is rejected if it takes you out of the water or accepted otherwise. In our case, we should assume that the system is in a particular configuration \mathbf{r}^N that has a nonzero Boltzmann factor. Let us denote this configuration by o (old). Thus we represent the Boltzmann factor for this system as $\exp[-\beta U(o)]$. Then we generate a new trial configuration n (new) for the system by implementing a small random displacement of a particle in configuration o . Next we decide on whether accepting or rejecting this trial move to the new configuration. The major constraint being that on average the new configuration n must be proportional to the probability density $\mathcal{N}(n)$. With this in mind we must determine a scheme that allows us to determine the transitional probability ($\pi(o \rightarrow n)$) in moving from an old configuration o to a new configuration n . If we simultaneously attempt to run a large quantity, say M , of MC simulations, we make the assumption total number of accessible configurations must be less than M . On average for say a configuration o , we wish to have the number of generated points ($m(o)$) to be proportional to $\mathcal{N}(o)$. For this to be true, at equilibrium, if we consider all the accepted trial moves in changing a system from configuration o to any new configuration n , these trial moves will be exactly equal to all the accepted trial moves in changing a system from these configurations n to configuration o . We specify the above requirement as the condition of detailed balance which is expressed as:

$$\mathcal{N}(o)\pi(o \rightarrow n) = \mathcal{N}(n)\pi(n \rightarrow o). \quad (3.9)$$

Previously it was stated that there are two steps in a MC move. Initially a particle displacement which consists of a trial move in displacing a particle such that the system changes from a configuration o to a new configuration n . We introduce the quantity α (underlying matrix of the Markov chain) which represents the transition matrix which is related to the probability of undergoing a trial move from one configuration to another. After attempting the particle displacement trial move, we must decide on whether it is feasible to accept it, else we will reject it. We use acc to represent the acceptance probability in going from one configuration to another. Clearly the transitional probability ($\pi(o \rightarrow n)$) in moving from an old configuration o to a new configuration n is

$$\pi(o \rightarrow n) = \alpha(o \rightarrow n) \times acc(o \rightarrow n). \quad (3.10)$$

However, if we make the reasonable assumption that α is a symmetric matrix ($\alpha(o \rightarrow n) = \alpha(n \rightarrow o)$), Eq. (3.10) simplifies to

$$\frac{acc(o \rightarrow n)}{acc(n \rightarrow o)} = \frac{\mathcal{N}(n)}{\mathcal{N}(o)} = \exp[-\beta[U(n) - U(o)]]. \quad (3.11)$$

Provided probabilities do not exceed one, many choices satisfy the above condition. The one performed by Metropolis *et al.* was the following one:

$$acc(o \rightarrow n) = \begin{cases} \mathcal{N}(n)/\mathcal{N}(o), & \text{if } \mathcal{N}(n) < \mathcal{N}(o). \\ 1, & \text{if } \mathcal{N}(n) \geq \mathcal{N}(o). \end{cases} \quad (3.12)$$

Using the latter we can decide whether a trial move is accepted or rejected using the following deductive reasoning. Provided $U(o) < U(n)$, If we were to generate a trial move from an old configuration o to a new configuration n , with the help of Eq. (3.12), the above trial move should be accepted provided

$$acc(o \rightarrow n) = \exp[-\beta[U(n) - U(o)]] < 1. \quad (3.13)$$

Next we generate a uniformly distributed random number (Rand) in the interval $[0, 1]$. If $\text{Rand} < acc(o \rightarrow n)$, then the trial move is accepted else it is rejected. No bias will be introduced unless

the random number generator is not generating uniformly distributed numbers between 0 and 1, and we can safely conclude that the probability of accepting a trial move from configuration o to new configuration n is equal to the acceptance probability $acc(o \rightarrow n)$.

3.1.2 Monte Carlo Algorithm

While MD codes are versatile and multi-purpose since they can be easily adapted to any kind of particle interactions, MC codes change considerably depending on the specific purpose and application. With this in mind, the goal of this dissertation involves calculating some thermodynamic equilibrium properties of hard-core mixtures in two and three dimensions, with a special focus on phase coexistence. In the previous section, it was established that a basic Monte Carlo method involving a Metropolis scheme consists of a Markov process involving a random walk as to sample a particular configuration with a probability directly proportional to the Boltzmann factor. A Metropolis scheme can be implemented easy according to the following steps:

1. Randomly selecting a particle and calculating the energy of the configuration ($U(o)$)
2. Randomly displace the particle by some amount Δ . Make a energy calculation of the new configuration $U(n)$
3. Choose whether or not to accept the move from the old configuration to the new with acceptance

$$acc(o \rightarrow n) = \exp[-\beta[U(n) - U(o)]], \quad \text{if } U(o) < U(n). \quad (3.14)$$

Along with the above algorithm, many other computational tricks are required in order to build an efficient and operational Monte Carlo simulation program. One such trick is that of periodic boundary conditions. In fact, due to the limitations determined by the available computer processing power, the size of the system (number of degrees of freedom, e.g. number of particles) has to be much less than the typical number of atoms / molecules in a macroscopic sample (Avogadro number), and only structural and thermodynamic properties of a few hundred to a few thousand particles can be simulated on ordinary machines. So the choice of boundary conditions has an important impact as the consequences of this relates to direct effects on the systems thermody-

dynamic properties. Take the example of N particles in a system in three dimensional space with free boundaries. There will be a proportionality of the order of $N^{-1/3}$ which represents the proportion of all particles situated at / near the surface of the system. So, in order to (partially) remove the finite-size effect due to the presence of the system-empty space boundary, we have to select periodic boundary conditions such that our N particle system is surrounded by an infinite *bulk*. What this means is that we treat the volume, e.g. a cube, containing the N particles as a primitive cell, and the latter is, for example in the case of cubic periodic boundary conditions, replicated along all of the directions of the Cartesian space an infinite number of times. In line of principle, each particle (i) experiences interactions from all the particles within this periodic system including its own periodic image. The total potential energy of the system would then be calculated as follows

$$U_{Total} = \frac{1}{2} \sum_{l,m,\mathbf{n}} 'u(|\mathbf{r}_{lm} + \mathbf{n}L|). \quad (3.15)$$

L represents the box length, \mathbf{n} is a vector comprising of three integers and the prime ($'$) is included as to indicate that if we have the condition that $\mathbf{n} = 0$, the term having $l = m$ must be excluded. Upon examination of the above equation, one may think that periodic boundary conditions aren't very useful due to the fact that an infinite sum of terms represents the entire potential energy of the system. However, we quite often consider systems of particles interacting with short-range pairwise potentials (like in our case), so we do not really have to calculate all of the contributions reported in the sum above. Then, the code speed-up can be attained by the use of neighbour lists (e.g. Verlet lists) which represent data structures containing all the particles interacting within a certain cutoff distance r_{cut} .

Another trick when building a Monte Carlo simulation program is that of reduced units. A unit of suitable convenience is chosen for length, mass and energy and all the other thermodynamic quantities used in the simulation are then expressed in terms of these reduced units. In Chapters that follow a representation of a quantity with reduced units is normally denoted with an asterisk superscript $*$. The main reason for the use of reduced units is that it facilitates comparisons among different systems. Another preliminary aspect we need to consider in order to start a MC computer simulation is the initialization of the system. This consists in assigning initial positions

to all the particles, and distributing them according to the value of some initial thermodynamic parameters, e.g. packing fraction or composition. With this in mind, we will discuss in detail the Gibbs ensemble Monte Carlo and its relative algorithm in the subsequent section.

3.2 Gibbs Ensemble Monte Carlo Method

Studying first order phase transitions in experiments is a fairly straightforward procedure in general. At a specific temperature and density, you detect a clear loss of homogeneity of the system because of the appearance of two or more distinct phases, with a definite interface separating these phases. Computer simulation differs from this as follows. In order to locate a first order phase transition we need to compute the thermodynamic properties of the separate phases and then locate points where intensive thermodynamic quantities, such as the pressure and chemical potential are equal in both phases. Again, there is a definite interface between the two distinct phases however the following problem arises. A large non negligible portion of the particles in the simulation shall be residing at or near the interface that divides the two separate phases. In fact, the fraction of particles found at or near the interface is directly proportional to $V^{\frac{2}{3}}$, meaning that as the number of particles in the system is increased, the fraction of particles at the interface becomes smaller (it scales as $V^{-\frac{1}{3}}$). This means that in order to calculate reliable coexistence data, we would need to study relatively large systems, that can easily be exceeding the computational constraints available to us with state-of-the-art computers. That is because large systems require long equilibrium times especially in a system where different molecular species are present as for the binary models we considered in this thesis. It wasn't until the mid 1980's that Panagiotopoulos [106] devised the Gibbs ensemble Monte Carlo (GEMC) method which overcame the problem arising from the presence of an interface. By using the GEMC method, simulations of two coexisting phases are carried out in two separate simulation boxes, where the boxes are kept at constant temperature, the total volume of the two boxes is fixed, and a fixed number of particles are distributed over the two boxes. Since the two boxes are not in physical contact, there is no interface and the bulk properties of the two coexisting phases can be obtained directly from simulation.

3.2.1 Acceptance Rules

At equilibrium the pressure, chemical potentials and temperatures of each of the coexisting phases need to be equal. With this in mind, you would assume that a constant- μ PT ensemble is better suited to study phase coexistence. However the practical implementation of this ensemble is problematic since all of the extensive parameters would be unbounded. In the previous section, it was stated that GEMC consists of simulating a fixed number of particles, at a fixed temperature while the total volume (sum of the volumes of the two boxes) is kept constant. We begin considering the partition function for a system of N particles distributed over two volumes V_1 and V_2 such that $V_2 = V - V_1$ with the particles in both boxes experiencing the same intermolecular interactions. We define scaled coordinates $\mathbf{s}_k^N = \frac{\mathbf{r}_k^N}{V_k^N}$, where $k = 1, 2$. The partition function of such system is given by:

$$Q_G(N, V, T) = \sum_{n_1=0}^N \frac{1}{V \Lambda^{3N} n_1! (N - n_1)!} \int_0^V dV_1 V_1^{n_1} (V - V_1)^{N - n_1} \times \int d\mathbf{s}_1^{n_1} \exp[-\beta U(\mathbf{s}_1^{n_1})] \int d\mathbf{s}_2^{N - n_1} \exp[-\beta U(\mathbf{s}_2^{N - n_1})] \quad (3.16)$$

From this, it follows that the probability of finding a configuration such that you have n_1 particles with positions $\mathbf{s}_1^{n_1}$ in box 1 and n_2 particles with positions $\mathbf{s}_2^{N - n_1}$ in box 2 is

$$\mathcal{N}(n_1, V_1, \mathbf{s}_1^{n_1}, \mathbf{s}_2^{N - n_1}) \propto \frac{V_1^{n_1} (V - V_1)^{N - n_1}}{n_1! (N - n_1)!} \exp[-\beta [U(\mathbf{s}_1^{n_1}) + U(\mathbf{s}_2^{N - n_1})]], \quad (3.17)$$

where we did not state the dependence of N on V_2 explicitly since $V_2 = V - V_1$ and the total volume V is constant. Using Eq. (3.17) we can now derive the acceptance rules for the various trial moves of a GEMC. The trial moves are as follows:

1. Randomly select a particle and displace it.
2. Volume change such that the total volume V remains constant.
3. Particle exchange by transfer of a randomly selected particle from a box to another one.

We begin by looking at the condition of detailed balance (Eq. (3.9)). For the particle displacement we expect that the acceptance rule should be the same as that of the constant-NVT ensemble. If

we assume that a configuration n is obtained after a displacement of a particle from configuration o in box 1, then the ratio of probability densities of these two states is given by

$$\frac{\mathcal{N}(n)}{\mathcal{N}(o)} = \frac{\exp[-\beta U(\mathbf{s}_n^{n_1})]}{\exp[-\beta U(\mathbf{s}_o^{n_1})]}, \quad (3.18)$$

and substitution of this into the condition of detailed balance yields

$$acc(o \rightarrow n) = \min(1, \exp[-\beta[U(\mathbf{s}_n^{n_1}) - U(\mathbf{s}_o^{n_1})]]), \quad (3.19)$$

which as suspected is identical to that used in the constant-NVT ensemble. If we were to assume that a configuration n is obtained after a displacement of a particle from configuration o in box 2, then we would find that the above derived acceptance rule changes such that n_1 would be replaced by $N - n_1$. This is due to the fact that we have $N - n_1$ particles in box 2 as opposed to n_1 particles in box 1. For derivations that follow we will only focus on box 1, as the formulas are symmetric with respect to the box label.

For the volume change acceptance rule, we consider a change ΔV , according to $V_1^n = V_1^o + \Delta V$. Here we find that the ratio of probability densities of the new and old states is given by

$$\frac{\mathcal{N}(n)}{\mathcal{N}(o)} = \frac{(V_1^n)^{n_1} (V - V_1^n)^{N-n_1} \exp[-\beta U(\mathbf{s}_n^N)]}{(V_1^o)^{n_1} (V - V_1^o)^{N-n_1} \exp[-\beta U(\mathbf{s}_o^N)]}. \quad (3.20)$$

Imposing the condition of detailed balance then yields

$$acc(o \rightarrow n) = \min\left(1, \frac{(V_1^n)^{n_1} (V - V_1^n)^{N-n_1}}{(V_1^o)^{n_1} (V - V_1^o)^{N-n_1}} \exp[-\beta[U(\mathbf{s}_n^N) - U(\mathbf{s}_o^N)]]\right). \quad (3.21)$$

For particle exchange we consider processes of a particle being removed as well as it being added to box 1. We start with the former and assume that we remove a particle from box 1 and place it in box 2 thus changing the configuration in box 1 from state o to n . Then the ratio of probability densities is given by

$$\frac{\mathcal{N}(n)}{\mathcal{N}(o)} = \frac{n_1!(N - n_1)!V_1^{n_1-1}(V - V_1)^{N-(n_1-1)}\exp[-\beta U(\mathbf{s}_n^N)]}{(n_1 - 1)!(N - (n_1 - 1))!(V_1)^{n_1}(V - V_1)^{N-n_1}\exp[-\beta U(\mathbf{s}_o^N)]}. \quad (3.22)$$

Imposing the condition of detailed balance leads to the acceptance rule:

$$\overline{acc}(o \rightarrow n) = \min\left(1, \frac{n_1(V - V_1)}{(N - n_1 + 1)V_1} \exp[-\beta[U(\mathbf{s}_n^N) - U(\mathbf{s}_o^N)]]\right). \quad (3.23)$$

For the sake of completion we now will derive the acceptance rule for the process of adding a particle to box 1 after it has been removed from box 2. The ratio of probability densities become

$$\frac{\mathcal{N}(n)}{\mathcal{N}(o)} = \frac{V_1^{n_1+1}(V - V_1)^{N-n_1-1}n_1!(N - n_1)! \exp[-\beta U(\mathbf{s}_n^N)]}{V_1^{n_1}(V - V_1)^{N-n_1}(n_1 + 1)!(N - n_1 - 1)! \exp[-\beta U(\mathbf{s}_o^N)]}. \quad (3.24)$$

The resulting acceptance rule for the process of adding a particle to box 1 after it has been removed from box 2 is

$$\overline{acc}(o \rightarrow n) = \min\left(1, \frac{V_1(N - n_1)}{(V - V_1)(n_1 + 1)} \exp[-\beta[U(\mathbf{s}_n^N) - U(\mathbf{s}_o^N)]]\right). \quad (3.25)$$

3.2.2 Extension of the Acceptance Rules to a Binary Mixture

For a binary mixture containing particles of species A and species B , we have $N = N_A + N_B$ particles distributed over two volumes V_1 and V_2 such that $V_2 = V - V_1$ with the particles in both boxes experiencing the same intermolecular interactions. It follows from Eq. (3.16) that the partition function for a binary mixture with fixed volume V is given by:

$$\begin{aligned} Q_G(n_A, n_B, V_1, N_A - n_A, N_B - n_B, V - V_1, T) &= \sum_{n_A=0}^{N_A} \sum_{n_B=0}^{N_B} \frac{1}{V \Lambda^{3(N_A+N_B)} n_A! n_B! (N_A - n_A)! (N_B - n_B)!} \\ &\int_0^V dV_1 (V_1)^{n_A+n_B} (V - V_1)^{N_A+N_B-n_A-n_B} \times \int d\mathbf{s}^{n_A} d\mathbf{s}^{n_B} \exp[-\beta(U_A(\mathbf{s}^{n_A}) + U_B(\mathbf{s}^{n_B}) + U_{AB}(\mathbf{s}^{n_A}, \mathbf{s}^{n_B}))] \\ &\int \mathbf{s}^{N_A-n_A} \mathbf{s}^{N_B-n_B} \exp[-\beta(U_A(\mathbf{s}^{N_A-n_A}) + U_B(\mathbf{s}^{N_B-n_B}) + U_{AB}(\mathbf{s}^{N_A-n_A}, \mathbf{s}^{N_B-n_B}))], \end{aligned} \quad (3.26)$$

From this we can establish that the probability density is given by

$$\begin{aligned} \mathcal{N}(n_A, n_B, V_1, N_A - n_A, N_B - n_B, V - V_1, T) &\propto \frac{V_1^{n_A+n_B} (V - V_1)^{N_A+N_B-n_A-n_B}}{n_A! n_B! (N_A - n_A)! (N_B - n_B)!} \times \\ &\exp[-\beta(U_A(\mathbf{s}^{n_A}) + U_B(\mathbf{s}^{n_B}) + U_{AB}(\mathbf{s}^{n_A}, \mathbf{s}^{n_B}) + U_A(\mathbf{s}^{N_A-n_A}) + U_B(\mathbf{s}^{N_B-n_B}) + U_{AB}(\mathbf{s}^{N_A-n_A}, \mathbf{s}^{N_B-n_B}))], \end{aligned} \quad (3.27)$$

We need to develop acceptance rules for the three trial moves of the GEMC method however for a binary mixture, we have to deal with the trial moves (particle displacement and particle exchange specifically) of each species separately. With regards to particle displacement, consider the situation in which a state n is obtained when a state o experiences a displacement of a particle of species A in box 1. It follows from Eq. (3.27) that the ratio of the probability densities of the two states is:

$$\frac{\mathcal{N}(n)}{\mathcal{N}(o)} = \frac{\exp[-\beta[U_A(\mathbf{s}_n^{nA}) + U_{AB}(\mathbf{s}_n^{nA}, \mathbf{s}_n^{nB})]]}{\exp[-\beta[U_A(\mathbf{s}_o^{oA}) + U_{AB}(\mathbf{s}_o^{oA}, \mathbf{s}_o^{oB})]]}, \quad (3.28)$$

giving us the following acceptance rule for when a particle of species A is displaced within box 1:

$$acc(o \rightarrow n) = \min(1, \exp[-\beta[U_A(\mathbf{s}_n^{nA}) + U_{AB}(\mathbf{s}_n^{nA}, \mathbf{s}_n^{nB}) - U_A(\mathbf{s}_o^{oA}) - U_{AB}(\mathbf{s}_o^{oA}, \mathbf{s}_o^{oB})]]). \quad (3.29)$$

Suppose now we consider the case in which a particle of species B is displacement in box 1 such that the configuration in box 1 changes from a state o to a new state n . Applying the same method to calculate the ratio of the probability densities for the case when a particle of species B is displaced within box 1 yields the acceptance rule:

$$acc(o \rightarrow n) = \min(1, \exp[-\beta[U_B(\mathbf{s}_n^{nB}) + U_{AB}(\mathbf{s}_n^{nA}, \mathbf{s}_n^{nB}) - U_B(\mathbf{s}_o^{oB}) - U_{AB}(\mathbf{s}_o^{nA}, \mathbf{s}_o^{nB})]]), \quad (3.30)$$

To derive the acceptance rules for the volume change, we consider an alternate method as proposed for a single component system and then extend this to a two component system. Suppose for we look back at equation Eq. (3.16) and we decide to make a random walk in $\ln[V_1/(V - V_1)]$ instead of in V_1 so as to avoid abrupt changes to the density, which could potentially bring to rejecting 100 % of the volume changes. With this choice for the random walk in $\ln[V_1/(V - V_1)]$, the partition function Q_G can be written as:

$$Q_G = \frac{1}{\Lambda^{3N} N!} \sum_{n_1=0}^N \binom{N}{n_1} \int_{-\infty}^{\infty} d\ln\left(\frac{V_1}{V - V_1}\right) \frac{V_1(V - V_1)}{V} V_1^{n_1} (V - V_1)^{N-n_1} \times \int d\mathbf{s}^{n_1} \exp[-\beta U(\mathbf{s}^{n_1})] \int d\mathbf{s}^{N-n_1} \exp[-\beta U(\mathbf{s}^{N-n_1})], \quad (3.31)$$

The probability density of a configuration \mathbf{n} with volume V_1 is proportional to

$$\mathcal{N}(n) \propto \frac{V_1^n (V - V_1)^{N-n_1+1}}{V n_1! (N - N_1)!} \exp[-\beta U(\mathbf{s}_n^N)] \quad (3.32)$$

Extending the above equation to a mixture containing species A and species B gives us the following probability density for a configuration \mathbf{n} in volume V_1 that has undergone a volume change ΔV according to $V_1^n = V_1^o + \Delta V$.

$$\mathcal{N}(n) \propto \frac{V_1^{n_A+n_B+1} (V - V_1)^{N_A+N_B-n_A-n_B+1}}{n_A! n_B! (N_A - n_A)! (N_B - n_B)!} \times \exp[-\beta [U_A(\mathbf{s}_n^{N_A}) + U_B(\mathbf{s}_n^{N_B}) + U_{AB}(\mathbf{s}_n^{N_A}, \mathbf{s}_n^{N_B})]], \quad (3.33)$$

Imposing the condition of detailed balance, we determine that the ratio of the probability densities of the two states \mathbf{n} and \mathbf{o} is given by:

$$\frac{\mathcal{N}(n)}{\mathcal{N}(o)} = \frac{(V_1^n)^{n_A+n_B+1} (V - V_1^n)^{N_A+N_B-n_A-n_B+1} \exp[-\beta [U_A(\mathbf{s}_n^{N_A}) + U_B(\mathbf{s}_n^{N_B}) + U_{AB}(\mathbf{s}_n^{N_A}, \mathbf{s}_n^{N_B})]]}{(V_1^o)^{n_A+n_B+1} (V - V_1^o)^{N_A+N_B-n_A-n_B+1} \exp[-\beta [U_A(\mathbf{s}_o^{N_A}) + U_B(\mathbf{s}_o^{N_B}) + U_{AB}(\mathbf{s}_o^{N_A}, \mathbf{s}_o^{N_B})]]} \quad (3.34)$$

this gives us the acceptance rule associated with volume change

$$\begin{aligned} \text{acc}(o \rightarrow n) = \min\left(1, \frac{(V_1^n)^{n_A+n_B+1} (V - V_1^n)^{N_A+N_B-n_A-n_B+1}}{(V_1^o)^{n_A+n_B+1} (V - V_1^o)^{N_A+N_B-n_A-n_B+1}} \right. \\ \left. \exp[-\beta [U_A(\mathbf{s}_n^{N_A}) + U_B(\mathbf{s}_n^{N_B}) + U_{AB}(\mathbf{s}_n^{N_A}, \mathbf{s}_n^{N_B}) - U_A(\mathbf{s}_o^{N_A}) - U_B(\mathbf{s}_o^{N_B}) - U_{AB}(\mathbf{s}_o^{N_A}, \mathbf{s}_o^{N_B})]]\right], \end{aligned} \quad (3.35)$$

To derive the acceptance rules for the particle exchange we again start with the probability density Eq. (3.31) for a two component system. We generate a configuration \mathbf{n} from a configuration \mathbf{o} ($(n_A + n_B)$ particles in box 1) by removing a particle of species A from box 1 and inserting this particle in box 2. The ratio of the probability densities of the two states are as follows:

$$\begin{aligned} \frac{\mathcal{N}(n)}{\mathcal{N}(o)} = \frac{V_1^{n_A+n_B-1} (V - V_1)^{N_A+N_B-n_A-n_B+1} (n_A - 1)! n_B! (N_A - n_A + 1)! (N_B - n_B)!}{V_1^{n_A+n_B} (V - V_1)^{N_A+N_B-n_A-n_B} n_A! n_B! (N_A - n_A)! (N_B - n_B)!} \\ \times \exp[-\beta [U_A(\mathbf{s}_n^{N_A}) + U_B(\mathbf{s}_n^{N_B}) + U_{AB}(\mathbf{s}_n^{N_A}, \mathbf{s}_n^{N_B}) - U_A(\mathbf{s}_o^{N_A}) - U_B(\mathbf{s}_o^{N_B}) - U_{AB}(\mathbf{s}_o^{N_A}, \mathbf{s}_o^{N_B})]], \end{aligned} \quad (3.36)$$

Simplifying the above expression gives us the acceptance rule for when a particle of species A is removed from box 1 and placed in box 2.

$$acc(o \rightarrow n) = \min\left(1, \frac{n_A(V - V_1)}{(N_A - n_A + 1)V_1} \exp[-\beta[U_A(\mathbf{s}_n^{N_A}) + U_B(\mathbf{s}_n^{N_B}) + U_{AB}(\mathbf{s}_n^{N_A}, \mathbf{s}_n^{N_B}) - U_A(\mathbf{s}_o^{N_A}) - U_B(\mathbf{s}_o^{N_B}) - U_{AB}(\mathbf{s}_o^{N_A}, \mathbf{s}_o^{N_B})]]\right) \quad (3.37)$$

Following the same procedure as above, we try to generate a configuration n from a configuration o by removing a particle of species B from box 1 and inserting this particle in box 2. The acceptance rule for this particle exchange is

$$acc(o \rightarrow n) = \min\left(1, \frac{n_B(V - V_1)}{(N_B - n_B + 1)V_1} \exp[-\beta[U_A(\mathbf{s}_n^{N_A}) + U_B(\mathbf{s}_n^{N_B}) + U_{AB}(\mathbf{s}_n^{N_A}, \mathbf{s}_n^{N_B}) - U_A(\mathbf{s}_o^{N_A}) - U_B(\mathbf{s}_o^{N_B}) - U_{AB}(\mathbf{s}_o^{N_A}, \mathbf{s}_o^{N_B})]]\right). \quad (3.38)$$

We also consider the process of adding a particle of either species to box 1 from box 2. Generating a configuration n in box 1 from a configuration o by adding a particle of species A from box 2 and following the same processes as above, gives us the following acceptance rule:

$$acc(o \rightarrow n) = \min\left(1, \frac{V_1(N_A - n_A)}{(V - V_1)(n_A + 1)} \exp[-\beta[U_A(\mathbf{s}_n^{N_A}) + U_B(\mathbf{s}_n^{N_B}) + U_{AB}(\mathbf{s}_n^{N_A}, \mathbf{s}_n^{N_B}) - U_A(\mathbf{s}_o^{N_A}) - U_B(\mathbf{s}_o^{N_B}) - U_{AB}(\mathbf{s}_o^{N_A}, \mathbf{s}_o^{N_B})]]\right). \quad (3.39)$$

Finally, the acceptance rule for generating a configuration n in box 1 from a configuration o by adding a particle of species B from box 2 is :

$$acc(o \rightarrow n) = \min\left(1, \frac{V_1(N_B - n_B)}{(V - V_1)(n_B + 1)} \exp[-\beta[U_A(\mathbf{s}_n^{N_A}) + U_B(\mathbf{s}_n^{N_B}) + U_{AB}(\mathbf{s}_n^{N_A}, \mathbf{s}_n^{N_B}) - U_A(\mathbf{s}_o^{N_A}) - U_B(\mathbf{s}_o^{N_B}) - U_{AB}(\mathbf{s}_o^{N_A}, \mathbf{s}_o^{N_B})]]\right). \quad (3.40)$$

3.2.3 Case Study: GEMC applied to a Particles in a Square Well Potential

Typically, a computer simulation is organized according to cycles. In the case of the GEMC, each cycle consists of N attempts of displacing a particle, an attempted volume change, and a number of attempts to exchange particles between the two boxes. N is usually equal to the total number of particles that make up the system. On average, nearly 1 – 5% of the attempted particle swaps are expected to be successful, as this is an empirical golden rule for getting a good sampling of the phase space of the system. Throughout the computer simulation, the condition of microscopic reversibility must be maintained. To that aim, the execution of the trial GEMC moves should be performed randomly, i.e. by selecting each of the three possible moves randomly. One of the disadvantages of performing the GEMC moves in a sequential manner is that it may make a difference at what point in the program the measurements of the thermodynamic properties are being gathered. When we are safe with regards to getting a working algorithm (see next section for the testing and building of a working GEMC code), we should verify whether the simulation has produced reliable results or not. The conditions for phase coexistence at thermodynamic equilibrium are as follows:

- The equality of the chemical potentials as evaluated in the two boxes.
- The pressure in each box must be equal.

Upon examination of the statistical averages for the pressures and chemical potentials, we expect that their values in one of the two boxes should be within the range of the statistical error of the values in the other box. In order to develop an operative understanding of a GEMC simulation it was decided to first perform a case study on a GEMC simulation applied to hard-sphere particles interacting with a square well potential. The purpose of this preliminary study was to learn how to analyze the statistical data as well as understand how to identify a genuine phase coexistence condition. The potential energy $U(r)$ for a pair of hard-spheres particles separated by a distance r , and interacting with a square-well potential is given as follows:

$$U(r) = \begin{cases} +\infty & \text{if } r < \sigma \\ -\epsilon & \text{if } \sigma \leq r < \lambda\sigma \\ 0 & \text{if } r \geq \lambda\sigma \end{cases}$$

where σ is the hard-sphere diameter of the particle, λ is the reduced range of the potential well, and ϵ is its depth. At the start of the simulation, we randomly place an equal number of particles each in box 1 and box 2 respectively. When thermodynamic equilibrium is reached in the two-phase region, we expected one box to contain the vapour phase, whilst the other one the liquid phase. During the course of the simulation the volumes and the number of particles in each of the two boxes are allowed to vary such that the temperature, total number of particles and total volume of the system remain constant. It is possible to show that the GEMC acceptance rules automatically ensure that the pressures P_1 and P_2 and the chemical potentials μ_1 and μ_2 in the two boxes are equal (we did not show it explicitly in the body of this thesis because the theory was extensively reported elsewhere [106, 103]); the temperatures in the two boxes are equal since this is the way we initialise the simulation (by specifying the reduced temperature in the two boxes to be the same). Then, when the chosen temperature is located below the critical point of the model, thermodynamic fluctuations will force the subsystems into regions of phase space representing the two coexisting phases. Actually, instead of performing a single computer simulation for a large enough number of GEMC cycles, it is customary in MC simulations to break the run in a finite number of blocks in order to minimize the statistical error [103]. The errors in the average properties of interest were estimated by calculating the standard deviations over 10 blocks. Once the system was equilibrated (total energies stabilize in the two boxes), the final particle configurations obtained from the previous block were then used as the starting point of simulations for the subsequent block. The same procedure was used in order to provide an initial configuration at a lower temperature by using the final configuration at the closest, higher considered temperature. By repeating the simulations for a series of temperatures and potential ranges, the vapour-liquid coexistence curves were finally determined. The input parameters we chose in the initial setup were just the total

volumes and number of particles in the two boxes. Verlet neighbour lists were used to speed up the simulation [103]. Initially, we ran the GEMC simulation for a temperature expected to be much higher than the critical temperature. It was observed that the densities in the two boxes were similar and the average values overlapped within the calculated statistical error. When we decreased the temperature nearby the critical temperature, we observed large density fluctuations in the two boxes. This generated the phenomenon of box inversion, i.e. within the duration of the simulation run we observed that the nature of the phase present in one of the two boxes was exchanged for a number of times with the one present in the other box. Finally, at a temperature well below the critical temperature, we observed a clean phase separation into two distinct phases, which would settle until the end of the simulation in either the two boxes: one corresponding to the liquid phase whilst the other to the vapour phase.

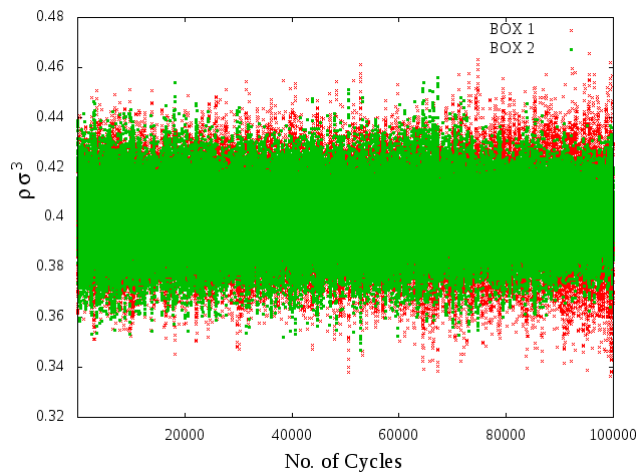


Figure 3.1: Density ($\rho\sigma^3$) vs number of cycles for a temperature above the critical temperature

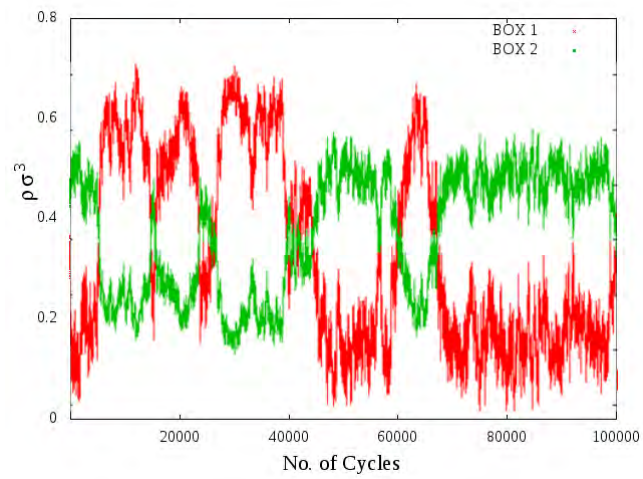


Figure 3.2: Density ($\rho\sigma^3$) vs number of cycles for a temperature at critical temperature

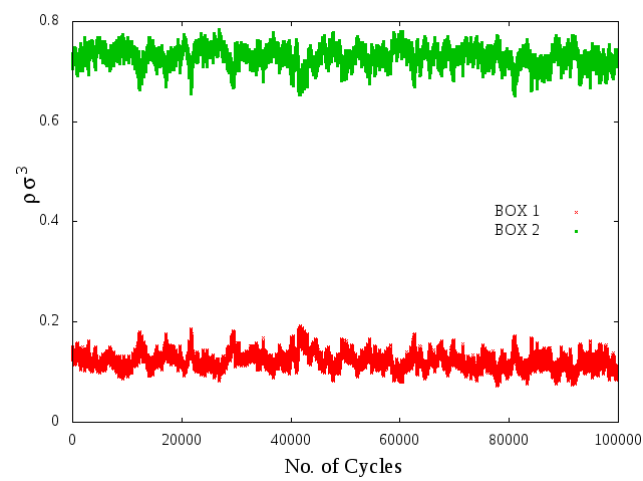


Figure 3.3: Density ($\rho\sigma^3$) vs number of cycles for a temperature below the critical temperature

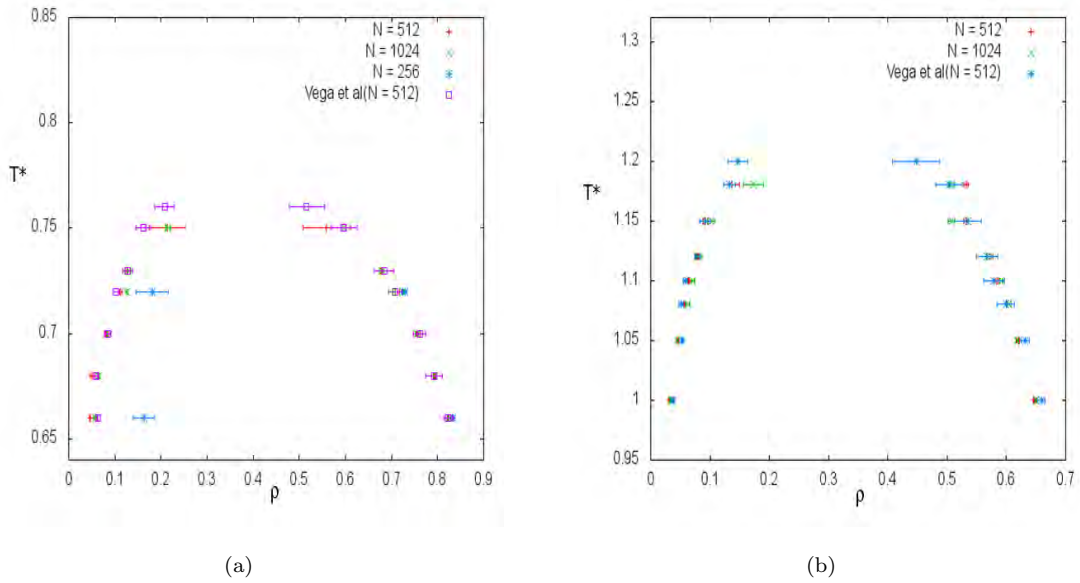


Figure 3.4: The vapour-liquid coexistence curves for hard-sphere particles interacting with a square well potential $\lambda = 1.25$ (a), $\lambda = 1.5$ (b)

For the vapour-liquid coexistence corresponding to $\lambda = 1.25$ (Fig. 3.4a), we ran simulations for three different system sizes ($N = 256, 512, 1024$). This was then compared to the results as reported in Vega *et al.* For a system size corresponding to $N = 512$ particles, we find that our results compare favourably with those reported in Vega *et al.* as can be seen by the overlapping errorbars associated with the density ρ . When the system size is increased to $N = 1024$ particles, a similar trend is observed however small differences in the values of thermodynamic quantities measured are observed due to the bigger size of the system. Finally when the system size is reduced to $N = 256$ particles ($\lambda = 1.25$), the size was too small to get quality results since in some of the simulations the number of particles in either box 1 or box 2 would go down to zero. A similar issue was observed for a similar system size corresponding to $\lambda = 1.5$. Thus, no coexistence curve is reported for $N = 256$ particles when $\lambda = 1.25$. When comparing the results of the larger systems $N = 512, 1024$ with that of Vega *et al.* (Fig. 3.4b), we again note overlapping of the errorbars and good agreement for a number of values of temperature.

Chapter 4

Building the Gibbs Ensemble

Monte Carlo code

4.1 Particle Exchange: The Constant-NVT Ensemble Test

As discussed in the previous chapter, The GEMC method consists of three trial moves. These being the particle displacement, volume change and particle exchange between the two boxes. However if we are to switch off two of the three trial moves, we can effectively run the computer simulation as a constant-NVT ensemble. This is achieved by switching off the volume change and the particle exchange, so that the resulting code reduces to a MC computer simulation in the constant-NVT ensemble, which is executed independently inside two separate boxes. Then, while building the full GEMC code and to determine if it was starting to produce the correct simulation results for the intensive parameters, it was decided to run it in the constant-NVT ensemble and compare the pressure and contact values for the radial distribution function to the ones reported in literature for a variety of different interaction and thermodynamic parameters.

Obviously, the chosen model for testing the code was the one we were interested to study later within the GEMC method. The fluid model is a nonadditive binary mixture of spheres (say species A and B) of diameter σ_A , σ_B , and $\sigma_A \leq \sigma_B$, so that the size ratio y is defined as $y = \sigma_A/\sigma_B$ (in what follows $\sigma = \sigma_A$ is the unit of length). The particles interact via hard-sphere pair potentials

$$\begin{aligned}
u_{ii}(r) &= \begin{cases} \infty & r < \sigma_i \\ 0 & \text{otherwise,} \end{cases} \\
u_{AB}(r) &= \begin{cases} \infty & r < (1 + \Delta) \frac{(\sigma_A + \sigma_B)}{2} \\ 0 & \text{otherwise,} \end{cases}
\end{aligned} \tag{4.1}$$

with $i \equiv A, B$, r the center-to-center distance between a pair of particles, and Δ the non-additivity parameter. For $\Delta > 0$, the model of Eq. (4.1) exhibits a fluid-fluid type transition [41]. Since the hard-sphere potential is infinite when particles interpenetrate and zero otherwise, the configurational energy is always zero and therefore for this model the free energy contains only the entropic term. The parameters we changed to test the code included the non-additivity parameter, composition, symmetry and density / packing fraction of the system.

As a reminder, in the constant-NVT ensemble the probability of finding the system in a particular new configuration (n) from a previous configuration (o) after a particle displacement is given by Eq. (3.11), and the acceptance rule is reported in Eq. (3.13). The generalization of these formulas to the case of binary mixtures coincides with the result that we achieved in the previous section when considering particle displacements for the two different species in one of the two boxes within the Gibbs ensemble (see Eq. 3.35-40). Now, we compare the results of our constant-NVT computer simulation with some of them available in the literature. One of which being the results produced by Jung *et al* [56] in which he also investigated the structural aspects and the equation of state of a system of nonadditive hard-sphere (NAHS) mixtures. We will also compare our results with the MC computer simulation results by Barošová *et al* [108], in which they also define a method called the Scaled Particle theory-Monte Carlo (SP-MC) method for calculating the chemical potentials of hard-sphere fluids up to very high densities.

4.1.1 Symmetric mixture with non-additive parameter $\Delta = 0.2$

We begin our comparison by simulating two small systems of $N = 256$ and $N = 500$ particles, respectively. Our results for the compressibility factor ($\beta P/\rho$) compare favourably with those of

		Jung <i>et al</i>		NVT simulations		
$\rho\sigma^3$	$\beta P/\rho$	g_{AA}	g_{AB}	$\beta P/\rho$	g_{AA}	g_{AB}
0.1	1.341(10)	1.236	1.161	1.341(10)	1.232	1.145
0.2	1.815(10)	1.582	1.329	1.811(15)	1.588	1.328
0.3	2.462(10)	2.128	1.465	2.471(30)	2.115	1.476
0.4	3.256(20)	2.889	1.443	3.262(35)	2.865	1.461

Table 4.1: $\beta P/\rho$ and radial distribution functions (g) for hard sphere mixtures with $y = \frac{\sigma_A}{\sigma_B} = 1.00$ for a system of ($N = 256$) particles

		Jung <i>et al</i>		NVT simulations		
$\rho\sigma^3$	$\beta P/\rho$	g_{AA}	g_{AB}	$\beta P/\rho$	g_{AA}	g_{AB}
0.1	1.330(0.0001)	1.215	1.109	1.340(10)	1.254	1.154
0.2	1.821(0.0010)	1.623	1.326	1.811(14)	1.624	1.308
0.3	2.454(0.0010)	2.131	1.445	2.461(23)	2.113	1.465
0.4	3.241(0.0010)	2.910	1.408	3.251(27)	2.912	1.419

Table 4.2: $\beta P/\rho$ and radial distribution functions (g) for hard sphere mixtures with $y = \frac{\sigma_A}{\sigma_B} = 1.00$ for a system of ($N = 500$) particles

Jung *et al.* for all the considered values of the density. It is observed that as density increases, so does the relative error of the calculated values of $\beta P/\rho$. This is due to the fact that as the box becomes more packed, the phase space to be sampled in MC simulations becomes larger, i.e. the number of available particle configurations of the system increase to the point that longer MC simulations would be needed in order to get the same statistical error. Our simulations were equilibrated for not less than 2×10^5 MC blocks, where a block in the NVT ensemble is just defined as a number of attempts to displace a particle equal to the total number of particles of the system. Then, we accumulated the averages and related errors of quantities of interest for 8 MC blocks.

Upon the inspection of the radial distribution function, we see that the discrepancy between the literature data [56] and our simulations is of the order of 1 % percentage. Aside from the error introduced by the finite length of our MC simulation, another source of error is in the way we calculated the contact values of the radial distribution functions, by performing an extrapolation of the numerical data for distances greater than the hard-sphere diameter. For such purpose, we adopted a third-order polynomial extrapolation by using the MC data for $g(r)$ available on the first four bins beyond the hard-sphere diameter. Unfortunately, in the paper by Jung *et al* the technical details of their MC simulations were not specified, including how many blocks were used, and the method adopted to calculate the contact values for the radial distribution functions. This prevented us from doing a more critical assessment of the tiny discrepancies observed from their data.

4.1.2 Asymmetric mixture with non-additive parameter $\Delta = 0.0$

		Barošová et al				NVT simulations			
η	x_2	$\beta P/\rho$	g_{AA}	g_{AB}	g_{BB}	$\beta P/\rho$	g_{AA}	g_{AB}	g_{BB}
0.3	0.0625	2.790(15)	1.92	2.22	3.55	2.781(10)	1.92	2.22	3.50
0.4	0.0625	4.410(22)	2.58	3.18	5.93	4.390(30)	2.59	3.19	5.88

Table 4.3: $\beta P/\rho$ and radial distribution functions (g) for hard sphere mixtures with $y = \frac{\sigma_B}{\sigma_A} = 3.333$, where x_B is the composition of the larger sphere with the system containing ($N = 1728$) particles

For the asymmetric mixture, the results produced by our computer simulation and the ones presented in the literature were in excellent agreement. This can be seen for both the compressibility factor ($\beta P/\rho$) as well as for the contact values of the radial distribution functions. In fact, in most of the cases the statistical errors of our data overlapped with those reported in the literature. However, it worth to note that the higher discrepancies were observed for the contact values of the radial distribution function of the larger sphere (BB) interactions. This is not surprising since at the composition ($x_2 = 0.0625$) we considered in the comparison, big spheres are considerably diluted

in comparison to small spheres, which makes it particularly important to sample the configuration space of the system in long simulations. However, we used the same equilibration-cumulation parameters as defined before for the asymmetric systems, whereas Barošová *et al.* simulated their system in 5 MC equilibration blocks and 40 cumulation blocks. Since each block consisted of 3.5×10^6 MC cycles, we conclude that their estimates for the contact values of the radial distribution functions are far more accurate, and this explains the small discrepancies observed for the contact values of g_{BB} (less than 1.5 %).

4.2 Particle Insertion: The Constant-NPT Ensemble Test

As we understood in the previous sections, the preliminary check when building a GEMC simulation code is to assess the results obtained with the Gibbs ensemble trial moves against those produced by computer simulation results as reported in the literature for other ensembles. For instance to test particle displacement we compared the results of the pressure and contact values of the radial distribution function as produced in our GEMC simulation to values found in the literature for the constant-NVT ensemble. Then, in order to check that the particle exchange trial move in our GEMC simulation code was functioning correctly, we compared our simulation results for the chemical potential to some of them reported in the literature in the NPT ensemble. This is the ensemble of choice since in reality most experiments are also carried out under conditions of constant pressure and temperature. It is also useful for determining the equation of state of a system even if the virial expression for the pressure (considered in detail in chapter 6) cannot be evaluated. To derive the acceptance rules for the constant-NPT ensemble, let us begin with its partition function. If we assume that we have a system of N identical atoms then the partition function can be written as

$$Q(N, V, T) = \frac{1}{\Lambda^{3N} N!} \int_0^L \dots \int_0^L d\mathbf{r}^N \exp[-\beta U(\mathbf{r}^N)]. \quad (4.2)$$

Assuming that the system is contained within a cubic box, let us introduce scaled coordinates \mathbf{s}^n such that

$$\mathbf{r}_i = L\mathbf{s}_i \quad \text{for } i = 1, 2, 3, \dots, N. \quad (4.3)$$

The partition function then becomes

$$Q(N, V, T) = \frac{V^N}{\Lambda^{3N} N!} \int_0^L \dots \int_0^L d\mathbf{s}^N \exp[-\beta U(\mathbf{s}^n; L)], \quad (4.4)$$

where $U(\mathbf{s}^n; L)$ indicates that U is also dependent on the system size. The Helmholtz free energy of the system is given by

$$\begin{aligned} F(N, V, T) &= -k_B T \ln Q \\ &= -k_B T \ln \left(\frac{V^N}{\Lambda^{3N} N!} \right) - k_B T \ln \int \mathbf{s}^N \exp[-\beta U(\mathbf{s}^n; L)] \\ &= F^{id}(N, V, T) + F^{ex}(N, V, T), \end{aligned} \quad (4.5)$$

with the two contributions from the Helmholtz free energy coming from the ideal gas expression (F^{id}) and the excess part, respectively (F^{ex}). Assume that the system is separated by a piston from an ideal gas reservoir and let V_o equal to the total volume of the system plus reservoir. If we let the total number of particles equal to M , then the partition function of the system is simply the product of the one of $M - N$ ideal gas molecules and the partition function of M particles:

$$Q(N, M, V, V_o, T) = \frac{V^N (V - V_o)^{M-N}}{\Lambda^{3M} N! (M - N)!} \int d\mathbf{s}^{M-N} \int d\mathbf{s}^N \exp[-\beta U(\mathbf{s}^n; L)]. \quad (4.6)$$

Since the integral over the scaled coordinates of the ideal gas is equal to 1, the total energy of the system is equal to $F^T - k_B T \ln Q(N, M, V, V_o, T)$. If the piston is not static and hence free to move, the volume of the subsystem can then fluctuate. It will do so that the free energy of the system be minimized. The probability density that the N particle subsystem has a volume V is represented by

$$\mathcal{N}(V) = \frac{V^N (V_o - V)^{M-N} \int d\mathbf{s}^N \exp[-\beta U(\mathbf{s}^n; L)]}{\int_0^{V_o} dV' V'^N (V_o - V')^{M-N} \int d\mathbf{s}^N \exp[-\beta U(\mathbf{s}^n; L)]}. \quad (4.7)$$

If we take the limit as the size of the reservoir tends to infinity, the large system will work as a manostat for the small system. This means that in the limit, a volume change of the small system does not change the pressure of the larger system. Then Eq. (4.6) and Eq. (4.7) become

$$Q(N, P, T) = \frac{\beta P}{\Lambda^{3N} N!} \int dV V^N \exp(-\beta PV) \int d\mathbf{s}^N \exp[-\beta U(\mathbf{s}^n; L)], \quad (4.8)$$

since in the limit $\frac{V}{V_o} \rightarrow 0$, $(V_o - V)^{M-N} = V_o^{M-N} [1 - (V/V_o)]^{M-N} \rightarrow \exp(-(M-N)V/V_o)$ and as $M-N \rightarrow \infty$, $\exp(-(M-N)V/V_o) \rightarrow \exp(-\rho V)$, where we also used the fact that the reservoir is an ideal gas and $\rho V = \beta P$. Hence the probability density becomes

$$\mathcal{N}_{N,P,T}(V) = \frac{V^N \exp(-\beta PV) \int d\mathbf{s}^N \exp[-\beta U(\mathbf{s}^n; L)]}{\int_0^{V_o} dV' V'^N \exp(-\beta PV') \int d\mathbf{s}^N \exp[-\beta U(\mathbf{s}^n; L)]}, \quad (4.9)$$

with

$$\mathcal{N}(V, \mathbf{s}^N) \propto V^N \exp(-\beta PV) \exp[-\beta U(\mathbf{s}^n; L)] \quad (4.10)$$

$$= \exp[-\beta U(\mathbf{s}^n, V)] + PV - N\beta^{-1} \ln V. \quad (4.11)$$

From this we can now derive the acceptance rule for the attempted change of the volume from V to $V' = V + \Delta V$.

$$acc(o \rightarrow n) = \min(1, \exp[-\beta U(\mathbf{s}^n, V') - U(\mathbf{s}^n, V) + P(V' - V) - N\beta^{-1} \ln(V'/V)]). \quad (4.12)$$

4.2.1 The Chemical Potential μ and the Widom method

In general, it is not possible to directly measure the free energy of a statistical-mechanical model of interaction. When sampling the phase space of a system, the free energy cannot be written as a simple average of a microscopic functions of coordinates and momenta of particles of the system.

The chemical potential of a species in a mixture is defined as the change of the free energy of the system when a particle of that species is added or removed to / from the mixture, while the number of the other particles species remains constant. The chemical potential μ_a of a species a can be written as the partial derivative of a thermodynamic potential as follows:

$$\begin{aligned}
\mu_a &= \left(\frac{\partial G}{\partial N_A}\right)_{PTN_{B \neq A}} \\
&= \left(\frac{\partial F}{\partial N_A}\right)_{VTN_{B \neq A}} \\
&= -T \left(\frac{\partial S}{\partial N_A}\right)_{VEN_{B \neq A}}, \tag{4.13}
\end{aligned}$$

where G , F , and S are the Gibbs free energy, the Helmholtz free energy, and the entropy respectively. Using Eq. (4.5) and substituting for the partition function Eq (4.4), we have that

$$\begin{aligned}
\mu &= -k_B T \ln \left(\frac{Q_{N+1}}{Q_N}\right) \\
&= -k_B T \ln \frac{\int d\mathbf{s}^{N+1} \exp[-\beta U(\mathbf{s}^{N+1}; L)]}{\int d\mathbf{s}^N \exp[-\beta U(\mathbf{s}^N; L)]} \\
&= \mu_{id}(\rho) + \mu_{ex}. \tag{4.14}
\end{aligned}$$

The above equation is in a very useful form due the fact that the ideal gas contribution μ_{id} has been separated and it can trivially be evaluated analytically. Next we use the separation $\Delta U = U(\mathbf{s}^{N+1}) - U(\mathbf{s}^N)$ and we can write the excess part of the chemical potential μ_{ex} as

$$\mu_{ex} = -k_B T \ln \int d\mathbf{s} \langle \exp(-\beta \Delta U) \rangle_N, \tag{4.15}$$

where $\langle \dots \rangle_N$ is the canonical ensemble average over the configuration space of the N-particle system. When calculating the average inside the integral during a MC computer simulation, the above integral can be calculated straightforwardly. This calculation can be achieved by a brute force approach where we would uniformly and randomly generate a coordinate \mathbf{s} and then use it to calculate $\exp(-\beta \Delta U)$. Then by averaging this quantity over all the trial moves we essentially obtain the average that is in Eq. (4.15). Note that we never accept the trial insertions but we instead calculate the Boltzmann factor associated with the random insertion of an additional particle into a N-particle system. The above method is known as the Widom insertion method and as explained above it consists of the addition of a "ghost" particle with a randomly generated position inside the simulation box, and in the calculation of the corresponding energy change of the system in order to calculate $\exp(-\beta \Delta U)$. Obviously, for a purely hard-sphere system this

process will reduce to just calculating the average number of successful particle insertions into the N-particle system.

The Widom insertion method described so far was considered in the canonical (NVT) ensemble, but it can be easily adapted to other ensembles [103]. Since we compare our estimate of the chemical potential with some other ones reported in the NPT ensemble, it is worth of mentioning the differences with the formula reported in Eq. (4.15). In fact, by using the procedure adopted before in the NPT ensemble, it is possible to show that the same separation between an ideal and an excess contribution to the chemical potential holds (even though the ideal part contribution will be different [103]), and that the fluctuating quantity to be averaged out is no longer $\exp(-\beta\Delta U)$, but rather $V \exp(-\beta\Delta U)$.

4.2.2 Relating the Constant-NPT Ensemble Monte Carlo Results to a GEMC without Volume Changes

Simulation of the NPT ensemble Monte Carlo involves two trial moves which correspond to a particle displacement and a volume change. Both trial moves are either accepted or rejected according to their respective acceptance rules which are related to calculating the change in energy of the system. These simulations are calculated for a given pressure, temperature and number of particles. So we expect the corresponding extensive quantities, e.g. the volume of the system, to fluctuate around their average values throughout the simulation. Other average quantities obtained in the NPT ensemble are the density and the chemical potential of the different chemical species. In order to check the chemical potentials obtained with our GEMC code, we implemented a *fake* Gibbs ensemble simulation where we fixed the volume of the two boxes (not just the total volume of them), and in order to avoid any inhomogeneous situation to happen inside them because of a phase transition, the density was chosen below the critical one. Moreover, we initialized the densities of the two boxes at the beginning of the simulation to be the same (and be equal to the average densities reported in the article by Lomba *et al.* [109] in order to avoid that the densities in the two boxes could eventually change because of the particle exchanges between them implemented in the GEMC code. So by ensuring the correct input densities are in the two boxes at

the beginning of the simulation, we could effectively compare the results of the chemical potential from the constant-NPT results in the literature and the GEMC. As reported in Table (4.4), our results compare favourable with those reported in the literature and provided us with additional evidence of the reliability of the implemented GEMC code for NAHSMs.

4.2.3 Symmetric mixture with non-additive parameter $\Delta = 0.2$

$\beta P \sigma^3$	N	x_2	Lomba <i>et al</i>			Computer Simulation			
			$\rho \sigma^3$	$\beta \mu_1$	$\beta \mu_2$	$\beta \mu_1^I$	$\beta \mu_2^I$	$\beta \mu_1^{II}$	$\beta \mu_2^{II}$
0.60	500	0.500	0.268(2)	0.21(3)	0.21(3)	0.2029(20)	0.2044(25)	0.2019(22)	0.2032(19)
0.70	500	0.500	0.292(2)	0.56(2)	0.56(2)	0.5719(11)	0.5715(26)	0.5726(27)	0.5713(19)
1.20	500	0.500	0.384(2)	2.04(4)	2.04(4)	2.0497(35)	2.0530(33)	2.0512(21)	2.0494(35)
1.30	500	0.500	0.399(3)	2.29(3)	2.29(3)	2.2870(24)	2.2900(54)	2.2885(36)	2.2902(41)
1.50	1000	0.259	0.437(2)	2.78(2)	2.78(2)	2.7710(27)	2.7869(39)	2.7727(26)	2.7881(42)
2.00	1000	0.034	0.529(2)	3.79(3)	3.79(4)	3.7890(35)	3.8376(33)	3.7901(44)	3.8289(37)
2.50	1000	0.010	0.587(3)	4.67(4)	4.61(9)	4.5840(55)	4.5847(45)	4.5810(46)	4.6522(47)

Table 4.4: Chemical potential $\beta\mu$ results from NPT-Ensemble Monte Carlo simulations. (Lomba et al: Phase stability of binary mixtures) and $\beta\mu$ for both box *I* and *II* from GEMC simulation without volume change (Computer Simulation).

Chapter 5

Gibbs Ensemble Monte Carlo of Nonadditive Hard-Sphere

Mixtures

5.1 Theory

Due to absence of configurational energy (see section 4.1), the temperature T becomes an irrelevant parameter and the conditions for a binary mixture to be in a two-phase equilibrium are:

$$P^I = P^{II}, \quad \mu_i^I = \mu_i^{II}, \quad (5.1)$$

where I and II are the labels for the two coexisting phases and P , μ_i are, respectively, the pressure of the system and the chemical potentials of species labeled as i . In the rest of the chapter, we will use reduced units of pressure $P\sigma^3/\epsilon$ and chemical potential μ_i/ϵ , unless otherwise specified, where $\epsilon = k_B T = 1$. The pressure for a binary mixture of hard-spheres can be written as:

$$\frac{\beta P}{\rho} = 1 + \frac{2\pi}{3} \rho \sum_{ij} x_i x_j \sigma_{ij}^3 g_{ij}(\sigma_{ij}), \quad (5.2)$$

where $g_{ij}(\sigma_{ij})$ are the contact values of the radial distribution functions of the two species labeled as i and j , $x_i = \frac{N_i}{N_A+N_B}$ is the composition of species i , $\beta = 1/k_B T$, k_B is the Boltzmann constant, the total number density is $\rho = \frac{N_A+N_B}{V}$, N_i the number of particles of species i , V is the total volume, and $i \equiv A, B$. Thermodynamic conditions reported in Eq. (5.1) are studied by means of Gibbs ensemble Monte Carlo (GEMC [106, 105, 103]) simulations in order to facilitate comparison with results already published in the scientific literature, and to provide a benchmark to theoretical approaches not biased by the presence of the interface between the two coexisting phases. Simulations were performed by using not less than 2000 particles in two cubic boxes with periodic boundary conditions [103]. The chemical potentials μ_i of the two hard-sphere species in the Gibbs ensemble are given by (for a generic simulation box labelled as 1):

$$\mu_i = -k_B T \ln \frac{1}{\Lambda_i^3} \left\langle \frac{V_1}{N_i + 1} \right\rangle_{V_1}, \quad (5.3)$$

where V_1 and N_i are, respectively, the volume of one of the two boxes (V_1 in the formula) and the number of particles of species i , Λ_i is the symbol we use to represent the De Broglie wavelength of species i , with $\langle \dots \rangle$ denoting the statistical average over the fluctuating V_1 and N_i . In the rest of the thesis, when writing the chemical potentials we will always neglect the term $\ln \Lambda_i^3$, which is identical across the two coexisting phases. Initial configurations of particle positions in the two boxes were generated by performing a short simulation in the grand canonical Monte Carlo (GCMC [103]) ensemble, that was stopped upon reaching the desired density in the two boxes. GEMC simulations were performed by using not less than $2 \cdot 10^5$ cycles to equilibrate the system. Then, statistical averages and related errors were collected following 10 cumulation runs of 10^4 cycles. Each GEMC cycle consists of a number of attempts to displace particles in the two boxes equal to the total number of particles, an attempt to change the total volume of the two boxes, and a number of particle exchanges between the two boxes between 1% and 5% of the total number of particles. We also checked for finite-size effects at some state points on larger systems of 4000 particles.

Thermodynamic properties are invariant with respect to interchange of the compositions x_i of the two species for symmetrical mixtures ($\sigma_A = \sigma_B$), i.e. $P(V, x_A, x_B) = P(V, x_B, x_A)$ and

$\mu_i(P, x_A, x_B) = \mu_i(P, x_B, x_A)$, where $x_B = 1 - x_A$. Thus, the following relationship holds (for symmetrical mixtures):

$$\mu_A^I = \mu_A^{II} = \mu_B^I = \mu_B^{II} \quad (5.4)$$

and the coexisting compositions x_α^i of the α species in phase i are symmetrical with respect to the equimolar composition $x_A = x_B = 0.5$:

$$x_A^I = x_B^{II}, x_B^I = x_A^{II}. \quad (5.5)$$

Then, the critical density ρ^{cr} of the NAHSM can be estimated by using the critical power-law

$$x_A - x_A^{cr} \propto |\rho - \rho^{cr}|^\beta, \quad (5.6)$$

where β is the critical exponent related to the order parameter, that can be assumed as $\beta = 0.325$ for the Ising 3D universality class, to which NAHSMs are expected to belong to [41]. In the asymmetric case ($\sigma_A \neq \sigma_B$), Eq.s (5.4) and (5.5) do not hold anymore, and Eq. (5.6) must be used to estimate also the critical composition x_A^{cr} .

In the remainder of this section, we also provide some basic details about the way the theoretical methods we compare with have been implemented in the literature. In the MIX1 [44] approximation the excess Helmholtz free energy A_{ex} of the mixture is written as:

$$\beta A_{ex} = \frac{\eta(1-\eta)}{(1-\eta)^3} + \frac{12\eta(2-\eta)}{(1-\eta)^3} x_A x_B \Delta, \quad (5.7)$$

where $\eta = \pi/6\rho\sigma^3$. The first term represents the Carnahan Starling excess free energy for pure hard spheres [6], and the second term is a Δ first-order perturbation correction. Once the Helmholtz free energy of the NAHSM model is known, the quantities appearing in Eq. (5.1) can be easily calculated by standard thermodynamic manipulations, and the phase coexistence boundaries evaluated accordingly. The *EOS1N* [56] equation of state (EOS) is written in terms of $\eta_e = B_2\rho/4$, where B_2 is the second virial coefficient:

$$\frac{\beta P}{\rho} = 1 + 4 \frac{\eta_e(1 - c_1\eta_e + c_2\eta_e^2)}{(1 - c_3\eta_e + c_4\eta_e^2)^3}, \quad (5.8)$$

where the coefficients c_i are linked to the second (B_2) and third (B_3) virial coefficients and are calculated by fitting MC data for $\beta P/\rho$ of small systems [56]. Also in this case, the knowledge of EOS (Eq. (5.8)) is sufficient to calculate the Helmholtz free energy of the system by integration [6] (see also subsequent Eq. (5.9), for a NAHSM $U = 0$ so that $A = -TS$, where S is the entropy). Note that while *EOS1N* is devised so to reproduce correctly B_2 and B_3 of the model, the original version of *MIX1* [44] fails to reproduce even the second virial coefficient [27].

The residual multiparticle entropy (RPME) is the quantity $\Delta S = S_{ex} - S_2$, where S_{ex} is the excess entropy with respect to the ideal value, that is calculated upon integration of the MC EOS

$$S_{ex} = - \int_0^\rho \left(\frac{\beta P}{\rho} - 1 \right) \frac{d\rho'}{\rho'}, \quad (5.9)$$

and S_2 is the two-body term [45] written as an integral of a functional of the radial distribution functions

$$S_2 = -\frac{1}{2}\rho \sum_{ij} x_i x_j \int \{g_{ij}(r) \ln[g_{ij}(r)] - g_{ij}(r) + 1\} dr. \quad (5.10)$$

Additional details about the RPME method can be found in a paper by Saija *et al.* [20].

Integral-equation theories are approximate functional relationships linking $g_{ij}(r)$ to the direct correlation functions $c_{ij}(r)$, which are solved simultaneously to the Ornstein-Zernike equations [46] for both $g_{ij}(r)$ and $c_{ij}(r)$. Specifically, the modified-hypernetted chain (MHNC) closure [47, 21, 46] is written as

$$g_{ij}(r) = \exp[-\beta v_{ij}(r) + h_{ij}(r) - c_{ij}(r) + B_{ij}^{HS}(r; \sigma_{ij}^*)], \quad (5.11)$$

where $h_{ij}(r) = g_{ij}(r) - 1$, and $B_{ij}^{HS}(r; \sigma_{ij}^*)$ are the bridge functions as calculated within the Percus-Yevick approximation for an hard-sphere mixture of diameters σ_{ij}^* [48]. The RY closure [49, 21, 46] is written as

$$g_{ij}(r) = \exp[-\beta v_{ij}(r)] \left\{ 1 + \frac{\exp\{f_{ij}(r)[h_{ij} - c_{ij}]\} - 1}{f_{ij}(r)} \right\}, \quad (5.12)$$

where $f_{ij}(r) = 1 - \exp[\xi_{ij}r]$. The parameters σ_{ij}^* and ξ_{ij} appearing, respectively, in the MHNC and RY closures, are adjusted so to fulfill a thermodynamic self-consistency of the theories between the otherwise different values achieved by the two osmotic compressibilities, which are evaluated by differentiating Eq. (5.2) with respect to the partial densities $\rho_i = \rho x_i$, and by the fluctuation theory formula

$$\left(\beta \frac{\partial P}{\partial \rho_i} \right)_{T, \rho_j (j \neq i)} = 1 - \sum_j \rho_j \tilde{c}_{ij}(q=0), \quad (5.13)$$

where $\tilde{c}_{ij}(q)$ is the Fourier transform of $c_{ij}(r)$, and $i \equiv A, B$. To calculate the excess Helmholtz free energy the virial pressure is integrated according to Eq. (5.9). Additional details about the procedure followed in order to calculate the phase coexistence properties are reported in Ref. [21]. First-order thermodynamic perturbation theory is a well-known subject of liquid state theory [6]. In its application to NAHSMs, a one-component, depletion potential for the large spheres in contact with a reservoir of small spheres is taken into consideration [21], and its liquid-vapour coexistence line is mapped onto the liquid-liquid phase coexistence of the binary mixture (see Ref. [21] and references therein for details).

Within DFT calculations the grand-potential $\Omega[\rho_A, \rho_B]$ as a functional of the one-body density profiles ρ_i is written as

$$\Omega[\rho_A, \rho_B] = A[\rho_A, \rho_B] - \sum_{i \equiv A}^B \int d\mathbf{r} \rho_i(\mathbf{r}) (\mu_i - V_i^{ext}(\mathbf{r})), \quad (5.14)$$

where $V_i^{ext}(\mathbf{r})$ is the external potential that acts on particles of species i , and $A[\rho_A, \rho_B]$ is the intrinsic Helmholtz free energy that is separated into an ideal A_{id} and excess A_{ex} contribution:

$$A[\rho_A, \rho_B] = A_{id}[\rho_A, \rho_B] + A_{ex}[\rho_A, \rho_B], \quad (5.15)$$

where

$$A_{id}[\rho_A, \rho_B] = \sum_{i \in A}^B k_B T \int d\mathbf{r} \rho_i(\mathbf{r}) (\ln(\Lambda_i^3 \rho_i(\mathbf{r}) - 1)). \quad (5.16)$$

Then, the excess Helmholtz free energy functional is constructed from a set of weighted densities $n_\nu^{(i)}(id)$, which are formed by convolution of the density profiles $\rho_i(\mathbf{r})$, with a set of geometrically-based weight functions $\omega_\nu^{(i)}$:

$$n_\nu^{(i)}(\mathbf{x}) = \int d\mathbf{r} \rho_i(\mathbf{r}) \omega_\nu(|\mathbf{x} - \mathbf{r}|, \sigma_i/2), \quad (5.17)$$

where $\nu = 0, 1, 2, 3$. Details about the specific form for the $\omega_\nu^{(i)}$ are reported in Ref. [29]. In DFT calculations, $\Omega[\rho_A, \rho_B]$ is minimized as a functional of the one-particle densities to find the equilibrium density profiles $\bar{\rho}_A, \bar{\rho}_B$, and the direct correlation functions are obtained by functional differentiation as:

$$c_{ij}(|\mathbf{r} - \mathbf{r}'|) = - \frac{1}{k_B T} \frac{\delta^2 A_{ex}}{\delta \rho_i(\mathbf{r}) \delta \rho_j(\mathbf{r}')} \Bigg|_{\rho_A, \rho_B = const}. \quad (5.18)$$

5.2 Results and Discussion

The first test we made was trying to reproduce computer simulation data of phase coexistence already published in the literature. We started with the symmetrical mixtures ($\sigma_A = \sigma_B$). For this limiting case of NAHSMs, SGCMC simulations would be better suited since the phase diagram is symmetrical with respect to the equimolar composition (as it was discussed in the previous section), and SGCMC particle identity exchanges are able to sample the phase space of the system more efficiently [41]. Actually, our GEMC data reported in Fig. (5.1) for $\Delta = 0.1$ compare favourably with the GEMC [39] reported in the literature. The small differences between the GEMC curves are probably to be ascribed to finite-size effects (different number of particles adopted) and/or calculation of error bars over a different number of blocks. Unfortunately, there are no computational details in the original paper reporting the GEMC simulations by Rovere and Pastore [39], and we could not assess this point further. These results confirm that a simple first-order perturbation theory (MIX1 [50]) provides an overall satisfactory description of the demixing of symmetrical

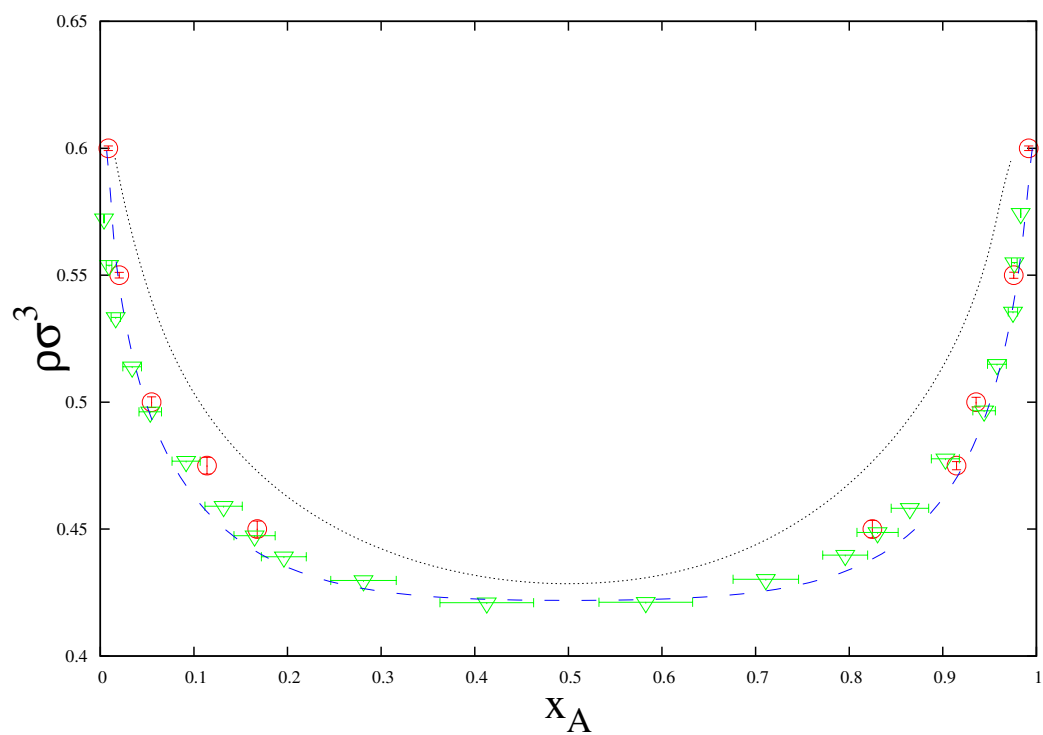


Figure 5.1: Fluid-fluid coexistence in the reduced total density-composition diagram for a symmetric mixture with $\Delta = 0.1$. Red circles with error bars: GEMC data - present work. Green triangles with error bars: GEMC data of Ref. [39]. Dotted line: MIX1 theory. Dashed line: EOS1N.

NAHSMs for $\Delta = 0.1$. On the other hand, an analytic equation of state called EOS1N [56], which is partly based on Monte Carlo data, provides a similar performance with the exception of the low / high composition regime where it slightly deteriorates in comparison to GEMC data.

P^I	P^{II}	μ_A^I	μ_B^I	μ_A^{II}	μ_B^{II}
1.3072(74)	1.3052(83)	2.3703(50)	3.6394(48)	2.3703(49)	3.6374(53)
1.3643(68)	1.3757(100)	2.5021(17)	3.8432(15)	2.5021(17)	3.8431(15)
1.4093(64)	1.4246(101)	2.6005(26)	4.0078(35)	2.6003(27)	4.0086(34)
1.4627(79)	1.4657(51)	2.7100(35)	4.1860(51)	2.7096(35)	4.1860(56)
1.6043(58)	1.5804(78)	2.9839(45)	4.5718(34)	2.9834(44)	4.5723(27)

Table 5.1: GEMC coexistence reduced pressures and chemical potentials of the two species in the two boxes for $y = 0.83$ and $\Delta = 0.182$.

The same assessment was done in Fig. (5.2) for $\Delta = 0.2$ Fig. (5.2). Again, there is an excellent agreement between our GEMC data and computer simulation data reported in the literature [51]. MIX1 agreement with computer simulation data is confirmed to be good but slightly deteriorating with respect to the case with lower nonadditivity. Considering the already mentioned problem of MIX1 in reproducing the correct second virial coefficient of the NAHSM model, and the fact it stems on a first-order expansion in the non-additivity parameter Δ , this happenstance is somewhat expected. A similar observation holds also for the EOS1N [56], though MIX1 still seems better performing at the low/high composition regime. It is interesting to note that while MIX1 appears to systematically underestimate GEMC data, the opposite is true for EOS1N, whose demixing line is always located above the GEMC data.

The only GEMC data available for the asymmetric NAHSMs were reported [39] for $y = 0.83$ and $\Delta = 0.182, 0.364$. In Figs. (5.3)-(5.4) we show the comparison of literature data at $\Delta = 0.182$ with the ones produced by us, and also a comparison with MIX1 theory. We note again that our simulation data are in very good agreement with GEMC data reported by Rovere and Pastore [39],

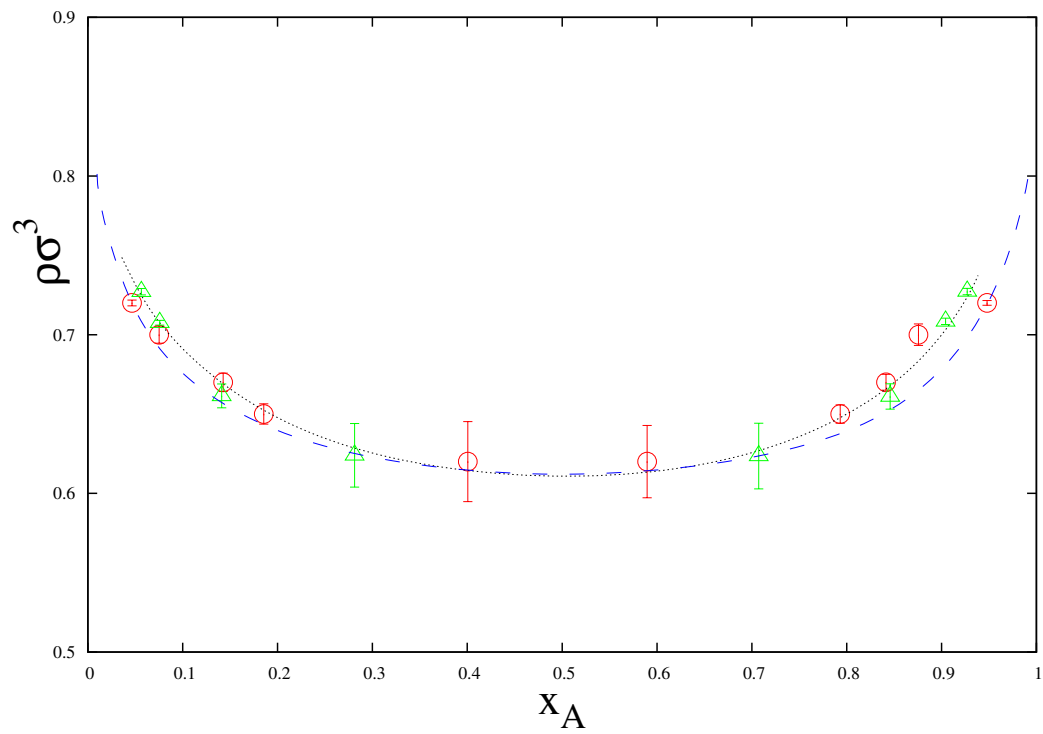


Figure 5.2: Fluid-fluid coexistence in the reduced total density-composition diagram for a symmetric mixture with $\Delta = 0.2$. Red circles with error bars: GEMC data - present work. Green triangles with error bars: GEMC data of Ref. [51]. Dotted line: MIX1 theory. Dashed line: EOS1N.

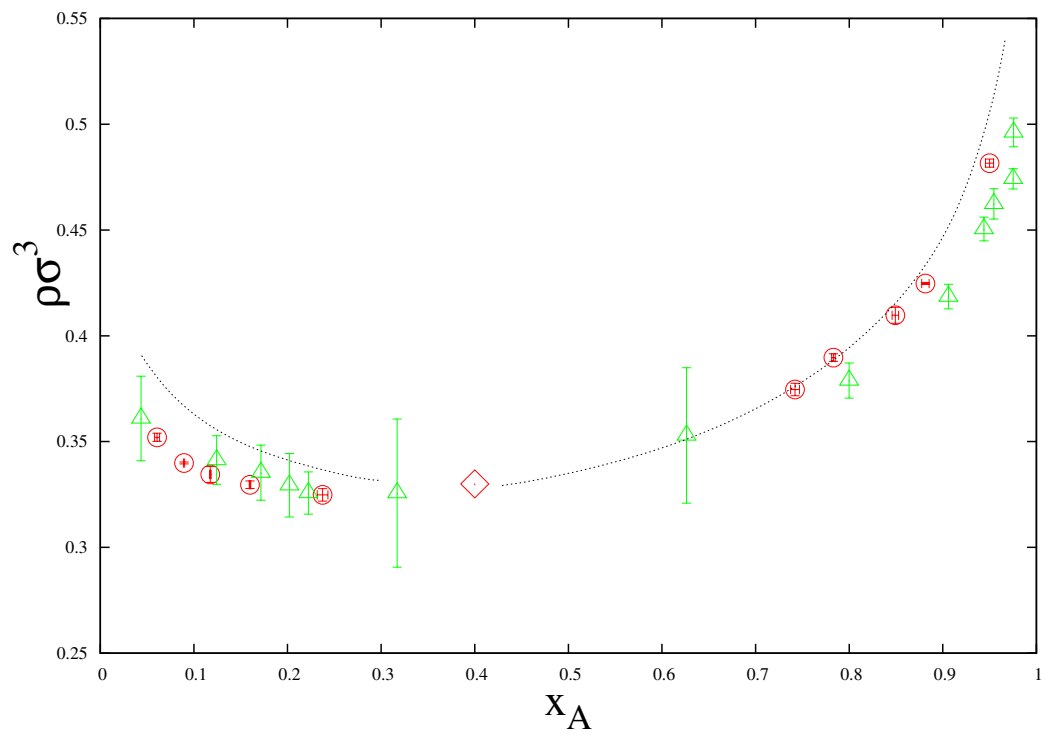


Figure 5.3: Fluid-fluid coexistence in the reduced total density-composition diagram for an asymmetric mixture with $y = 0.83$, $\Delta = 0.183$. Red circles with error bars: GEMC data - present work. Green triangles with error bars: GEMC data of Ref. [39]. Dotted line: MIX1 theory. Red diamond: GEMC critical point.

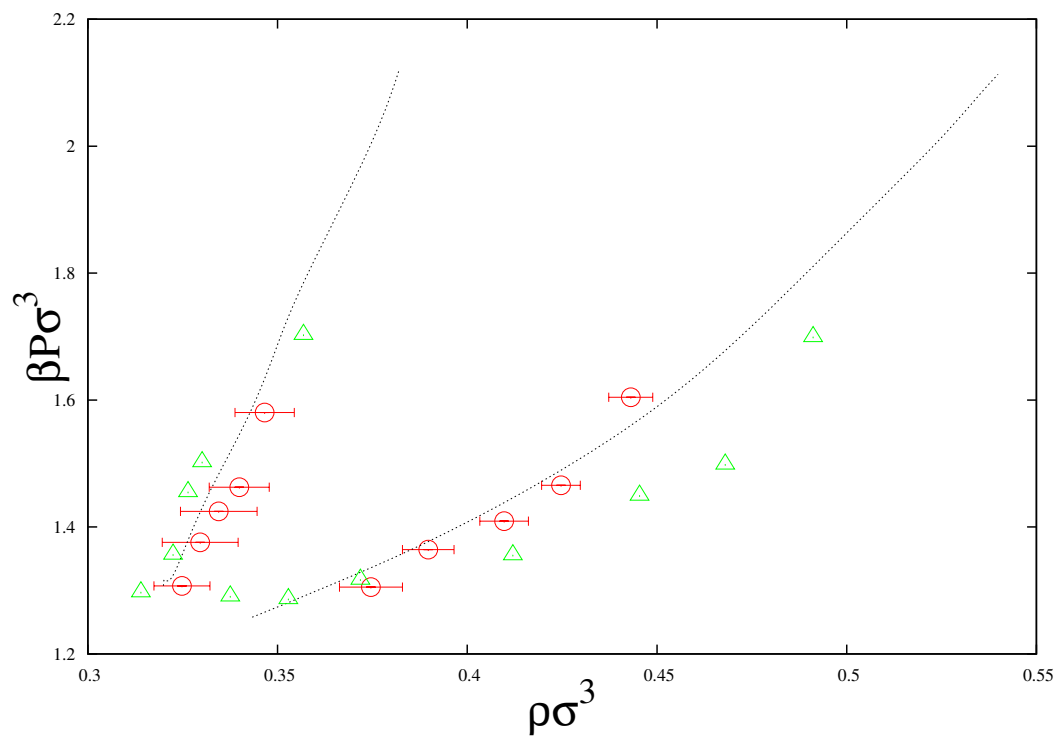


Figure 5.4: Fluid-fluid coexistence in the reduced pressure-density diagram for for an asymmetric mixture with $y = 0.83$, $\Delta = 0.183$. Legend: see Fig. 5.3.

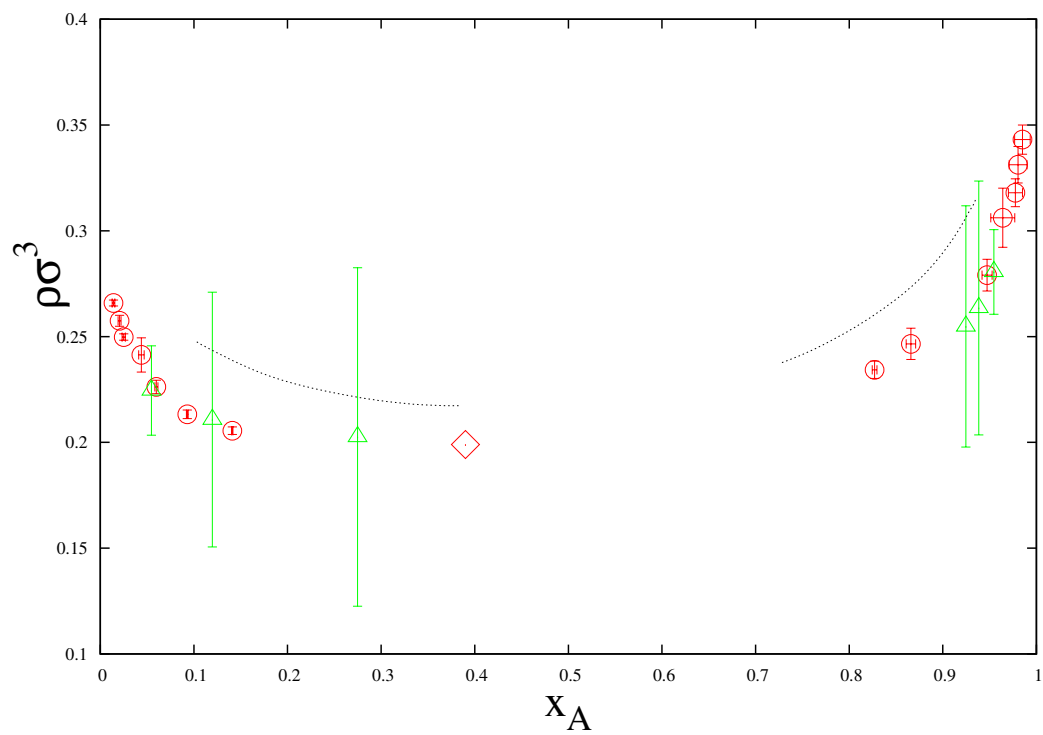


Figure 5.5: Fluid-fluid coexistence in the reduced total density-composition diagram for an asymmetric mixture with $y = 0.83$, $\Delta = 0.364$. Legend: see Fig. 5.3.

P^I	P^{II}	μ_A^I	μ_B^I	μ_A^{II}	μ_B^{II}
0.5202(57)	0.5203(24)	0.2618(15)	0.8712(26)	0.2616(15)	0.8712(26)
0.5431(32)	0.5469(34)	0.3472(40)	1.0008(56)	0.3459(40)	1.0009(55)
0.5987(15)	0.5887(37)	0.5382(58)	1.2394(15)	0.5371(56)	1.2388(19)
0.6683(49)	0.6670(71)	0.7770(97)	1.5330(62)	0.7763(04)	1.5341(54)
0.7072(48)	0.7003(47)	0.8796(92)	1.7072(82)	0.8802(98)	1.7026(74)
0.7457(70)	0.7446(87)	1.0110(12)	1.8621(11)	1.0096(109)	1.8659(276)
0.7875(57)	0.7956(73)	1.1338(112)	2.0591(302)	1.1314(127)	2.0547(296)

Table 5.2: GEMC coexistence reduced pressures and chemical potentials of the two species in the two boxes for $y = 0.83$ and $\Delta = 0.364$.

and the agreement with MIX1 is even improved at higher compositions of the smaller particle (see Fig. (5.3)). Also the coexistence pressures are reasonably reproduced, and MIX1 appears in slightly better agreement with the present GEMC data than with the previously reported ones.

In Fig. (5.5), we report the same comparison for $\Delta = 0.364$. Here the agreement between the GEMC simulations is very good, although the previously reported data are affected by a large error. As observed for the symmetric case, at the considered higher value of the non-additivity parameter there is a slight worsening of the predictions of MIX1 as compared to the computer simulation results. It is also worth to note that the smaller error we estimated with our simulations on the demixing region allows a more fair understanding of the theoretical predictions, than it was achieved in the past.

An approach that has been widely used to detect phase coexistence boundaries is based on the calculation of the zero of the residual multiparticle entropy (zero-RMPE) $\Delta S = S_{ex} - S_2$ (see previous section for details about the procedure to calculate this quantity). ΔS provides a quantitative measure of the weight of spatial correlations involving more than two particles in the configurational entropy of the system [52, 53, 54, 19, 20]. Since its validity was never assessed for asymmetric NAHSMs against true computer simulation results for the demixing region, we

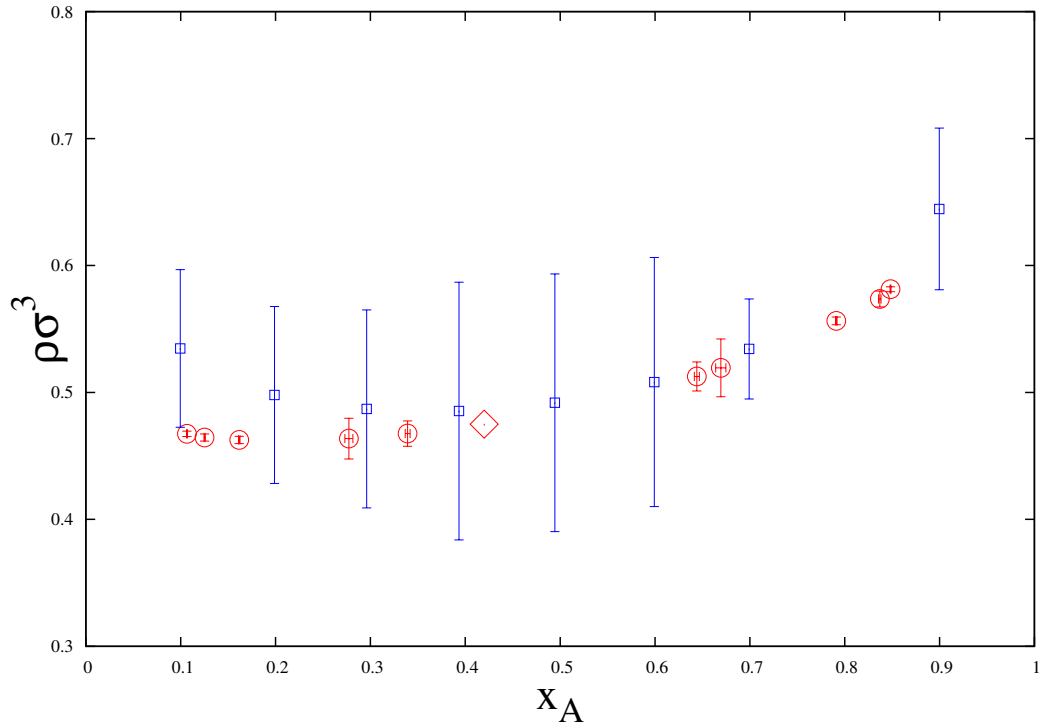


Figure 5.6: Fluid-fluid coexistence in the reduced total density-composition diagram for an asymmetric mixture with $y = 0.85$, $\Delta = 0.1$. Red circles with error bars: GEMC data - present work. Blue squares with error bars: zero-Residual Multi Particle Entropy ($\Delta S = 0$) of Ref. [20]. Red diamond: GEMC critical point.

P^I	P^{II}	μ_A^I	μ_B^I	μ_A^{II}	μ_B^{II}
2.8394(169)	2.8682(139)	5.2186(148)	7.3012(135)	5.2166(157)	7.2977(137)
2.8792(113)	2.8815(160)	5.2727(150)	7.4041(193)	5.2751(151)	7.3949(174)
3.0450(121)	3.0597(153)	5.5220(96)	7.7722(82)	5.5238(98)	7.7739(92)
3.1292(222)	3.1134(165)	5.6175(129)	7.9726(92)	5.6215(106)	7.9619(172)
3.1986(161)	3.1733(157)	5.7142(82)	8.1222(77)	5.7161(90)	8.1283(124)

Table 5.3: GEMC coexistence reduced pressures and chemical potentials of the two species in the two boxes for $y = 0.85$ and $\Delta = 0.1$.

P^I	P^{II}	μ_A^I	μ_B^I	μ_A^{II}	μ_B^{II}
2.4574(125)	2.4713(119)	4.5977(127)	8.4854(226)	4.5979(121)	8.4891(195)
2.4759(187)	2.4860(110)	4.6257(75)	8.5366(140)	4.6275(63)	8.5284(166)
2.5874(109)	2.5706(98)	4.8169(104)	8.9001(195)	4.8166(118)	8.8921(124)
2.7186(91)	2.7026(158)	5.0276(105)	9.3302(188)	5.0287(98)	9.3798(285)

Table 5.4: GEMC coexistence reduced pressures and chemical potentials of the two species in the two boxes for $y = 0.75$ and $\Delta = 0.1$.

considered the cases $\Delta = 0.1$ and $y = 0.85, 0.75$ for which some predictions of the $\Delta S = 0$ curve are reported in Ref. [20].

We show the comparison of the latter with GEMC simulations in Figs. (5.6) ($y = 0.85$) and (5.7) ($y = 0.7$) and in both cases we found a remarkable agreement between the theoretical and computer simulation demixing regions. However, the zero-RMPE is an intrinsically one-phase criterium, and it does not allow for an estimate of the critical point, so we could not assess this point. In Ref. [20], the spinodal points within the Martinov-Sarkysov (MS) integral-equation theory are also reported, and they are located at higher density than both the GEMC and $\Delta S = 0$ predictions. Even in this case, there is no estimate of the critical point since the building of the spinodal curve is not based on a calculation of the free energies of the two coexisting phases. The calculation of a binodal curve within MS theory poses a challenge because of its intrinsic thermodynamic inconsistency [46]. However, the correct qualitative behavior observed for MS theory prompted us to get additional insight into the ability of integral-equation theories (IETs) to provide reliable predictions also for the GEMC binodal line.

For this reason, we considered some results which have been reported for the fluid-fluid phase coexistence line in Ref. [21], by using such sophisticated IETs as the modified hypernetted-chain (MHNC), the Rogers-Young (RY) IETs [46]. These theories are expected to provide an even better prediction of the demixing region than the MS theory, since they implement a thermodynamic self-consistency between the virial and compressibility equations of state [46, 7]. Results for $\Delta = 0.1$

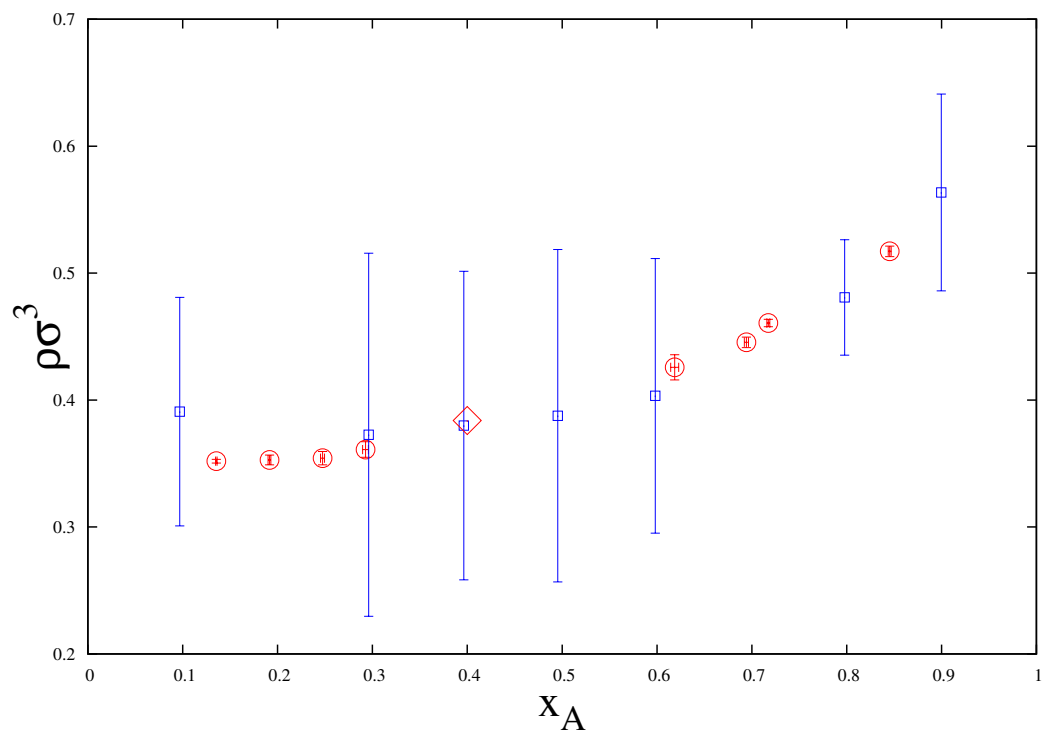


Figure 5.7: Fluid-fluid coexistence in the reduced total density-composition diagram for an asymmetric mixture with $y = 0.75$, $\Delta = 0.1$. Legend: see Fig. 5.6.

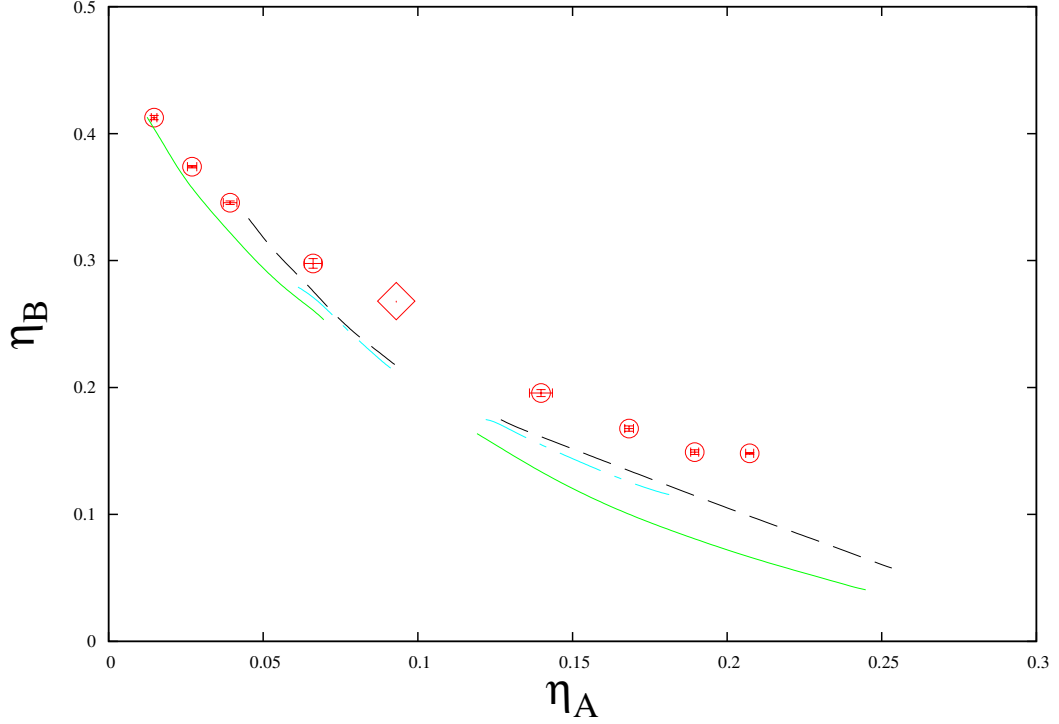


Figure 5.8: Fluid-fluid coexistence in the diagram of the packing fractions of the two species for an asymmetric mixture with $y = 0.75$, $\Delta = 0.1$. Red circles with error bars: GEMC data - present work. Dashed line: MHNC theory. Dot-dashed line: RY theory. Full line: first-order thermodynamic theory. All of the theoretical results taken from Ref. [21]. Diamond: GEMC critical point.

and $y = 0.75$ are reported in Fig. (5.8) on the diagram $\eta_A - \eta_B$ of the partial packing fractions of the two species, where $\eta_i = \frac{\pi}{6} \rho x_i \sigma_i^3$. We see that the two IETs provide a fair description of the demixing region, even though they fail to be quantitative especially in the region of higher packing fractions of the smaller species. However, the critical point prediction of the two theories (located in the empty region of the two coexisting branches) seems a reasonable one as compared to the GEMC estimate (diamond symbol in Fig. (5.8)). Not surprisingly, the two IETs perform much better than a mean-field approach based on a first-order thermodynamic perturbation theory, which is also reported in Fig. (5.8). Further decreasing y to 0.6 suggests that higher size asymmetries

P^I	P^{II}	μ_A^I	μ_B^I	μ_A^{II}	μ_B^{II}
2.4122(82)	2.4129(87)	4.5058(97)	8.3128(159)	4.5065(99)	8.3204(149)
2.5372(95)	2.5656(105)	4.7556(118)	8.7796(183)	4.7543(124)	8.7617(100)
2.7057(109)	2.6972(196)	5.0243(88)	9.3173(227)	5.0264(91)	9.2927(143)
3.1333(127)	3.1092(95)	5.6958(112)	10.529(244)	5.7015(130)	10.5691(425)

Table 5.5: GEMC coexistence reduced pressures and chemical potentials of the two species in the two boxes for $y = 0.75$ and $\Delta = 0.1$.

P^I	P^{II}	μ_A^I	μ_B^I	μ_A^{II}	μ_B^{II}
1.7010(39)	1.7036(56)	3.2357(63)	10.229(180)	3.2356(63)	10.224(200)
1.7739(40)	1.7603(44)	3.3793(55)	10.599(254)	3.3790(254)	10.626(244)
1.9013(71)	1.9156(98)	3.6662(76)	11.328(424)	3.6667(76)	11.298(669)

Table 5.6: GEMC coexistence reduced pressures and chemical potentials of the two species in the two boxes for $y = 0.6$ and $\Delta = 0.1$.

constitute a difficult test for IETs. In fact, as it is shown in Fig. (5.9) both IETs fail to reproduce the GEMC computer simulation data, and tend to underestimate the packing fractions at which demixing occurs. Also in this case, the situation is worse for the first-order perturbation theory, whose critical point region appears even below the one predicted by IETs.

Since the main output of microscopic theories are not thermodynamic quantities but structural functions, we also reported in Figs. (5.10)-(5.11) some NVT MC radial distribution functions (rdfs) for a couple of selected thermodynamic states in proximity of the boundary of the homogeneous phase with the two-phase region. Since we also performed some theoretical calculations within the MHNC integral-equation theory to be compared with the MC ones, we have been forced to select a state not too close to the two-phase region as predicted by MC computer simulation. The reason being that theoretical calculations tend to overestimate the extent of the two-phase region, and we had to select a state-point that was still in the stable region of the thermodynamic plane, as

P^I	P^{II}	μ_A^I	μ_B^I	μ_A^{II}	μ_B^{II}
0.5664(43)	0.5603(23)	0.4685(100)	5.5097(213)	0.4684(101)	5.5502(216)
0.6619(27)	0.6526(51)	0.8101(84)	6.6185(298)	0.8097(98)	6.5988(172)
0.7235(29)	0.7173(42)	1.0000(117)	7.3050(381)	1.0002(121)	7.2838(292)

Table 5.7: GEMC coexistence reduced pressures and chemical potentials of the two species in the two boxes for $y = 0.5$ and $\Delta = 0.2$.

P^I	P^{II}	μ_A^I	μ_B^I	μ_A^{II}	μ_B^{II}
0.3172(22)	0.3187(22)	-0.5451(51)	2.5740(82)	-0.5458(54)	2.5768(95)
0.3628(28)	0.3515(23)	-0.3547(45)	3.1580(65)	-0.3556(44)	3.1671(89)
0.4386(42)	0.4294(23)	-0.0327(42)	4.1507(102)	-0.0270(31)	4.1377(161)
0.4903(36)	0.5033(34)	0.0764(56)	0.1417(179)	0.0014(96)	0.3582(146)

Table 5.8: GEMC coexistence reduced pressures and chemical potentials of the two species in the two boxes for $y = 0.5$ and $\Delta = 0.3$.

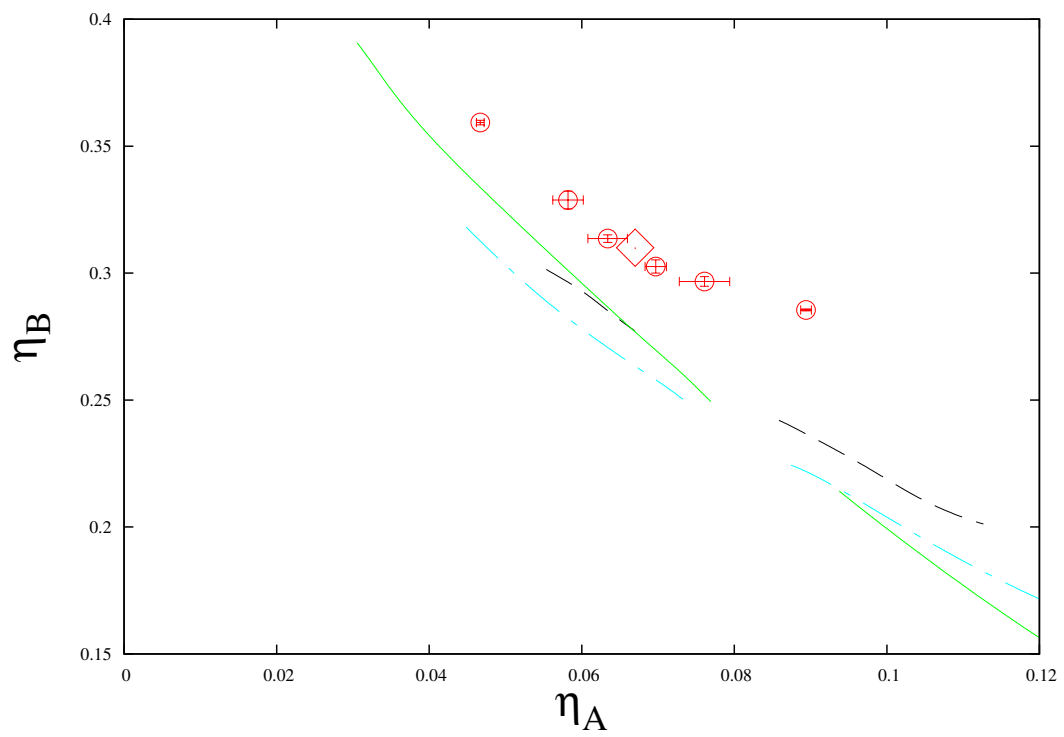


Figure 5.9: Fluid-fluid coexistence in the diagram of the packing fractions of the two species for an asymmetric mixture with $y = 0.6$, $\Delta = 0.1$. Legend: see Fig. 5.6.

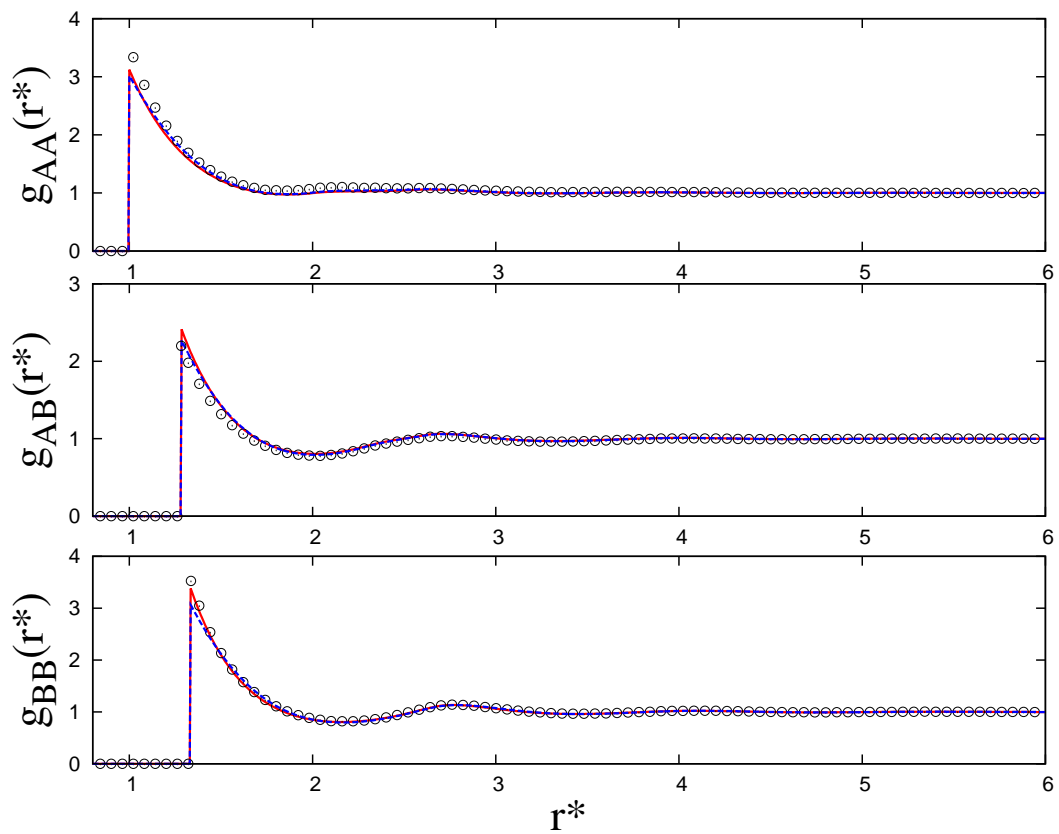


Figure 5.10: Radial distribution functions for an asymmetric mixture with $y = 0.75$, $\Delta = 0.1$, $\eta_A = 0.0905$, $\eta_B = 0.214$, as a function of reduced distance $r^* = r/\sigma$. Circles: NVT Monte Carlo simulation. Full, red line: MHNC theory. Dashed, blue line: PY theory.

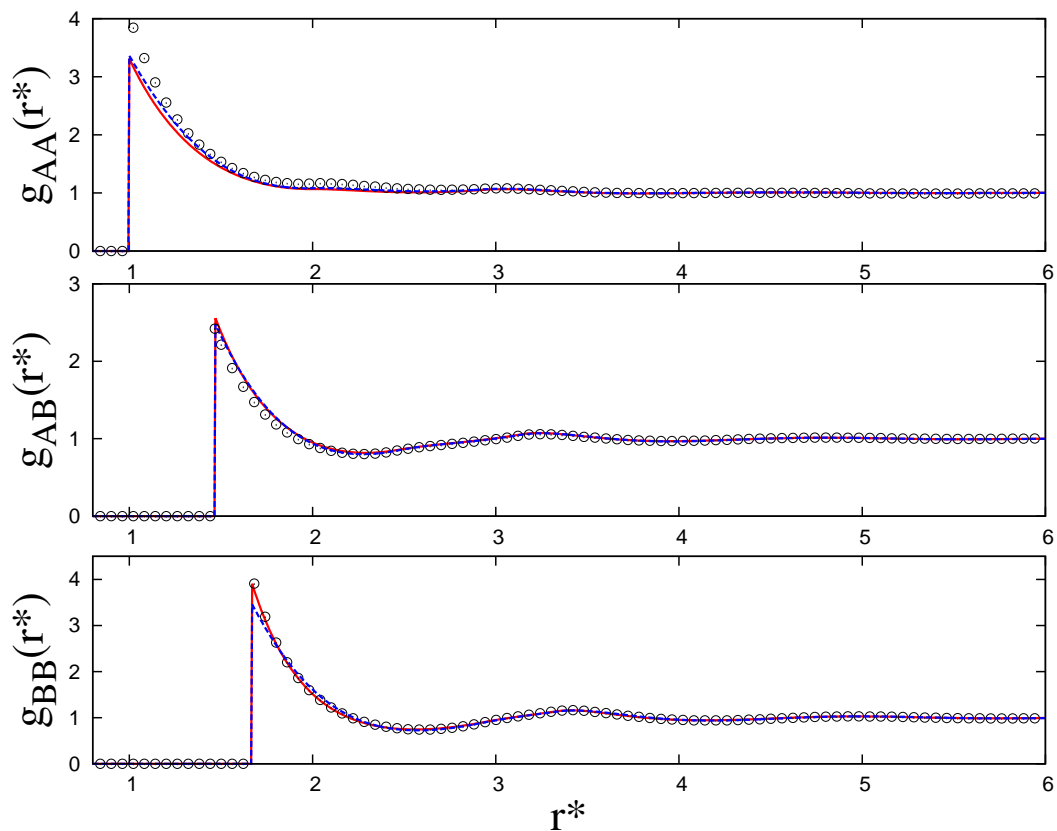


Figure 5.11: Radial distribution functions for an asymmetric mixture with $y = 0.6$, $\Delta = 0.1$, $\eta_A = 0.061$, $\eta_B = 0.284$ as a function of reduced distance $r^* = r/\sigma$. Circles: NVT Monte Carlo simulation. Full, red line: MHNC theory. Dashed, blue line: PY theory.

predicted by the microscopic theory. We also performed a similar calculation within PY theory [48], which allowed us to better understand the effect of the thermodynamic self-consistency constraints (the equality between the derivatives with respect to the partial densities of Eq. (5.2) and (5.13)) imposed within MHNC theory. In fact, PY theory is thermodynamically inconsistent [46] and it is remarkable to see how the imposed thermodynamic self-consistency is able to improve the reliability of MHNC rdfs between bigger particles in comparison to PY ones for $y = 0.75$ (see bottom panel of Fig. (5.10)), even though there is no sensible improvement for small particle-small particle and crossed rdfs (see top and middle panel of Fig. (5.10)). These features are even exacerbated for the higher size ratio $y = 0.6$ (see Fig. (5.11)). Another possibility to improve the reliability of IETs might be to force a global thermodynamic self-consistency, instead of a local one according to the derivatives of the virial and fluctuation theory pressures (see Ref. [55] for a discussion on this subject).

We concluded our investigation of the performance of theoretical approaches by also considering a weighted version of classical density functional theory (DFT), as reported in Ref. [29]. In Figs. (5.12)-(5.13), we show the comparison of DFT versus GEMC for the demixing region at $y = 0.5$ and $\Delta = 0.2, 0.3$. DFT tends to overestimate the extent of the two-phase region as compared to GEMC data, with the prediction of the critical point becoming less accurate as the non-additivity parameter is increased from $\Delta = 0.2$ (Fig. (5.12)) to $\Delta = 0.3$ (Fig. (5.13)). The tendency of DFT to underestimate the packing fractions of the demixing region has already been observed for IETs, and it was also reported for highly asymmetric mixtures with both DFT and a mean field theory due to Barboy and Gelbart [29].

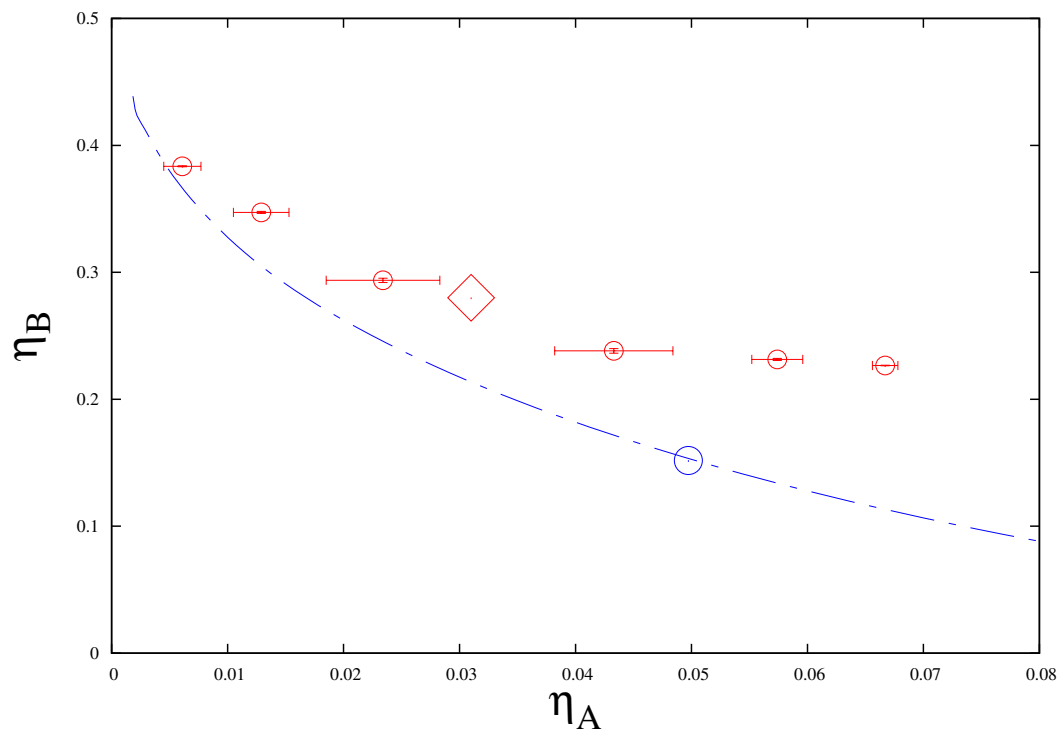


Figure 5.12: Fluid-fluid coexistence in the diagram of the packing fractions of the two species for an asymmetric mixture with $y = 0.5$, $\Delta = 0.2$. Red circles with error bars: GEMC data - present work. Dot-dashed line: DFT of Ref. [29]. Red diamond: GEMC critical point. Blue circle: DFT critical point.

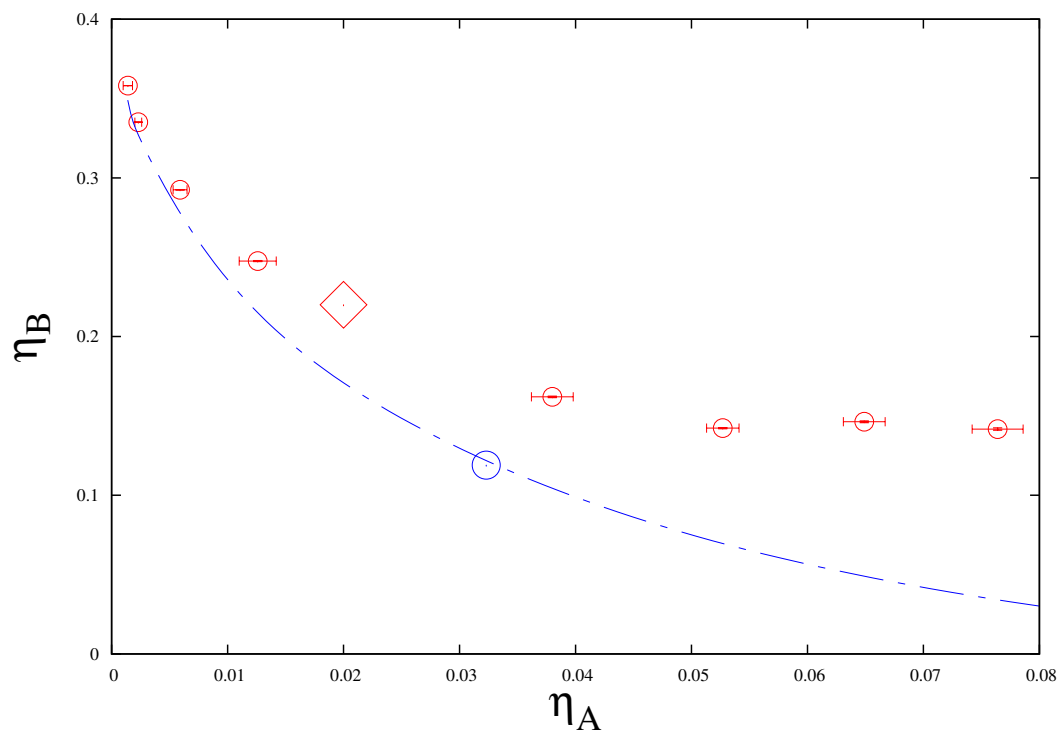


Figure 5.13: Fluid-fluid coexistence in the diagram of the packing fractions of the two species for an asymmetric mixture with $y = 0.5$, $\Delta = 0.3$. Legend: see Fig. 5.12.

5.3 Conclusion

Gibbs ensemble Monte Carlo simulations of nonadditive, binary hard-sphere mixtures were performed over a small to moderate range of size-asymmetry and non-additivity parameters. The GEMC fluid-fluid phase coexistence curves were used as a benchmark to test a number of theoretical approaches, including analytical equations of state, the zero-residual multi particle entropy approach, integral-equation theories, and classical density-functional theory. The results suggest that enhancing the asymmetry of the diameters of the two species and/or increasing the values of the non-additivity parameter, is a challenging condition for all of the theories considered. The only approach that proves to be able to provide a fully quantitative reproduction of the GEMC demixing region is the one based on the zero-RMPE. Thus, the calculation of the zero-RMPE to locate the demixing region appears as a promising approach to be implemented in liquid-state theories as applied to NAHSMs, and it would be interesting to see in the future some prediction of the entropic criterium based on the microscopic theories we considered here (IETs and DFT). Besides this accomplishment, GEMC data provide a novel and useful reference to be used in order to improve any existing liquid-state theory, or to assess the validity of new ones. It was also shown that thermodynamic self-consistency is able to improve the reliability of structural functions of integral-equation theories, even though a satisfactory reproduction of small particle-small particle and crossed correlation functions is still missing.

Chapter 6

EOS and GEMC of Nonadditive Hard-Disk Mixtures

6.1 Virial expansion

In this section, we consider explicitly the equation of state (EOS) of a binary hard-disk mixture. The model is a nonadditive binary mixture of disks consisting of disks from species A and B of diameter σ_A , σ_B , and $\sigma_A \leq \sigma_B$, so that the size ratio y is defined as $y = \sigma_A/\sigma_B$ (in what follows $\sigma = \sigma_A$ is the unit of length). The particles interact via hard-disk pair potentials as already reported for hard spheres in Eq. (4.1) with the difference being that we only consider interactions in two dimensions (x and y) since we are dealing with mixtures of hard-disks.

Now, we will report about a comprehensive investigation of both the EOS and the fluid-fluid phase transition, that was performed in collaboration with the National Council of Research (CNR) of Italy (Prof F. Saija), and with the University of Messina, Italy (Prof G. Fiumara). The virial expansion arrested to the fifth order can be written as:

$$\beta P = \rho + B\rho^2 + C\rho^3 + D\rho^4 + E\rho^5 + \dots \quad (6.1)$$

where P is the pressure, $\beta = 1/k_B T$ is a quantity (inverse of the temperature) expressed in units of the Boltzmann constant k_B . $\rho = \rho_1 + \rho_2 = \frac{N_1 + N_2}{V}$, with V being the volume and the ρ_i are,

respectively, the total and i -th species number densities. In the remaining part of the thesis, we shall refer to the virial expansion arrested to the third ($D = E = 0$ in Eq. (6.1)), fourth ($E = 0$ in Eq. (6.1)), and fifth order (see Eq. (6.1)) as, respectively, $Zvir3$, $Zvir4$, and $Zvir5$.

In a mixture, the virial coefficients B, C, D, E, \dots do also depend on the relative concentration of the two species. The fifth-order virial coefficient is given by the expression:

$$E = E_{11111}x_1^5 + 5E_{11112}x_1^4x_2 + 10E_{11122}x_1^3x_2^2 + 10E_{11222}x_1^2x_2^3 + 5E_{12222}x_1x_2^4 + E_{22222}x_2^5 \quad (6.2)$$

where for $i = 1, 2$, $x_i = \frac{N_i}{N_1+N_2}$ represents the mole fraction of each species respectively. The fifth virial coefficient with regards to a monodisperse fluid which consists of particles which have diameters σ_{11} or σ_{22} , can be used to calculate the terms E_{11111} and E_{22222} . As for the three dimensional case, ten classes of cluster integrals that cannot be reduced, account for this coefficient whose current best estimate is $E_{11111}/\sigma_{11}^8 = 2.03071192(25)$ [92]. The partial coefficients E_{11112} , E_{11122} are represented by twenty-four and forty-five classes of distinct cluster integrals, respectively. For sake of completeness they are thoroughly reported in Appendix 2. The remaining two coefficients E_{11222} , E_{12222} are obtained from the graphical expressions of E_{11112} , E_{11122} respectively, after the interchange of particles according to their sizes (i.e. larger particles with smaller particles as well as the reverse). In the symmetric case of equal size components ($\sigma_{11} = \sigma_{22}$) $E_{11112} = E_{12222}$ and $E_{11222} = E_{11122}$.

By the knowledge of the virial coefficients it is possible to build up some refined equations of state that in principle should improve over the accuracy of the virial expansion. Hence, we will consider the rescaled virial expansion (RVE) proposed by Baus and Colot [93] to obtain an (approximate) equation of state for a symmetric NAHD mixture. The RVE equation of state truncated to the fifth order has the following form: [93, 94]:

$$Z = \frac{\beta P}{\rho} = \frac{c_0 + c_1\eta + c_2\eta^2 + c_3\eta^3 + c_4\eta^4}{(1 - \eta)^2}, \quad (6.3)$$

where $Z = \beta P/\rho$ is the compressibility factor. Similarly as for the virial expansions related to Eq. (6.1), in the remaining part of the paper we shall refer to the rescaled virial expansions arrested to the third ($c_3 = c_4 = 0$ in Eq. (6.3)), fourth ($c_4 = 0$ in Eq. (6.3)), and fifth order (see Eq. (6.3)) as, respectively, $Zsc3$, $Zsc4$, and $Zsc5$.

The coefficients c_0 , c_1 , c_2 , c_3 and c_4 , depend only on the mole fraction and reproduce the first n virial coefficients exactly. In general we have [94]:

$$c_n = b_n - 2b_{n-1} + b_{n-2} \quad (6.4)$$

where b_n are the reduced virial coefficients so defined: $b_0 = 1$, $b_1 = \frac{B}{\xi}$, $b_2 = \frac{C}{\xi^2}$, $b_3 = \frac{D}{\xi^3}$, and $b_4 = \frac{E}{\xi^4}$ where, for a symmetric mixture $\xi = \frac{\pi}{4}$ and the packing fraction is $\eta = (\pi/4)\rho[x_1\sigma_{11}^2 + (1-x_1)\sigma_{22}^2] = (\pi/4)\rho\sigma^2$ ($\sigma_{11} = \sigma_{22} = \sigma$).

In order to trace the phase-coexistence curve, we calculated numerically the Helmholtz free energy according to the formula:

$$\begin{aligned} \frac{\beta A}{N} &= \int_0^\rho \left(\frac{\beta P}{\rho'^2} \right) d\rho' \\ &= [\ln(\rho' \Lambda^3) - 1] + \sum_{k=1}^2 x_k \ln(x_k) + \int_0^\rho \left(\frac{\beta P/\rho' - 1}{\rho'} \right) d\rho' \end{aligned} \quad (6.5)$$

Where $[\ln(\rho' \Lambda^3) - 1] + \sum x_k \ln(x_k)$ are representative of the contributions from the ideal gas. For a symmetric mixture, the condition required for the stability of a material (at equilibrium, chemical potentials of both distinct phases are equal) provides us with the identity

$$\left(\frac{\partial A}{\partial x_i} \right)_{T,\rho} = 0, \quad (6.6)$$

provided the mole fraction of the two coexisting phases satisfy that $x_1^I = x_2^{II}$ and $x_2^I = x_1^{II}$. The critical point falls at $x_1^c = x_2^c = 1/2$ and after fixing the value of Δ one can find a solution x_i (with $i=1,2$) of Eq. (6.6). We can then trace the coexistence lines by using a method such as the double tangent method (see Ref. [96, 56, 65] for details).

6.2 Monte Carlo simulation

The equations of state as obtained by means of the different theoretical approaches were assessed against NVT Monte Carlo (MC [103]) computer simulations, in which the virial pressure was calculated according to the formula as reported by Eq. (5.2). Initial *NVT* configurations were generated by performing a short simulation in the grand canonical Monte Carlo (GCMC [103]) ensemble, that was stopped upon reaching the desired density in the two boxes. Then, the system

was equilibrated along 10^6 MC cycles, where each cycle consisted in a number of attempts to displace a particle equal to the total number of particles $N = 1000$. The acceptance rate for particle displacements was fixed at 40% and cubic periodic boundary conditions were applied to the simulation box [103].

Phase coexistence properties were calculated by means of Gibbs ensemble Monte Carlo (GEMC [106, 105, 103]) simulations. The total number of disks in the two boxes was fixed to 2000, and the attainment of conditions of phase coexistence was checked by verifying the equality of the pressures in the two boxes according to Eq. (5.2), and the equality of the chemical potentials of the two species, as calculated according to the formula Eq. (5.3). The system was equilibrated by using $5 \cdot 10^5 - 10^6$ GEMC cycles. Subsequently, statistical averages were collected following 20 cumulation runs of 10^5 cycles. Each GEMC cycle consists of a number of attempts to displace particles in the two boxes equal to the total number of particles, an attempt to change the total area of the two boxes, and a number of particle exchanges between the two boxes between 1% and 5% of the total number of particles.

The critical density ρ^{cr} of the systems considered was estimated by using the critical power-law Eq. (5.6) with reference to β beta being the critical exponent related to the order parameter, whose exact value for the two-dimensional case is $\beta = 1/8$ [107], and $x_1^{cr} = 0.5$ for symmetrical mixtures.

6.3 Results and Discussion

A tabulation of E_{11112} and E_{11122} are represented in Table 6.1. If we take the limit as $\Delta \rightarrow 0$, it is seen that partial coefficients approach the value of the fifth virial coefficient of a mono component hard-disk fluid as found to be the quantity $2.03071192\dots$ (units of σ_{11}^8). We find that these quantities tend to behave in a manner that is qualitatively very similar to the nonadditive hard-sphere mixture case [65]. We will deal with the positive value of nonadditivity only. The behavior of $E(x_1)$ when $\Delta > 0$ is shown in Fig. 6.1. The cumulative fifth virial coefficient $E(x_1)$ is symmetric around $x_1 = 1/2$. When $\Delta < 0.4$, the curves representing $E(x_1)$ consist of a centralized maximum however this changes to a minimum, that is bound on both sides by maxima displaying a symmetry, when the nonadditivity parameter becomes larger. For $\Delta > 0.5$, $E(x_1)$ tends to be

Δ	E_{11112}	E_{11122}
0.05	2.368(2)	2.529(2)
0.10	2.730(2)	3.030(2)
0.15	3.120(2)	3.494(3)
0.20	3.535(2)	3.863(3)
0.25	3.977(2)	4.066(4)
0.30	4.444(2)	4.007(5)
0.35	4.938(2)	3.571(7)
0.40	5.458(2)	2.60(1)
0.45	6.001(3)	0.93(4)
0.50	6.569(3)	-1.67(2)
0.55	7.168(3)	-5.45(1)
0.60	7.789(3)	-10.778(6)
0.65	8.438(3)	-17.962(5)
0.70	9.113(3)	-27.464(4)
0.75	9.813(3)	-39.800(3)
0.80	10.538(3)	-55.561(2)
0.85	11.288(3)	-75.429(2)
0.90	12.066(3)	-100.200(2)
0.95	12.869(3)	-130.777(2)
1.00	13.698(3)	-168.195(2)

Table 6.1: The partial coefficients E_{11112} and E_{11122} for a symmetric NAHD mixture tabulated as a function of the nonadditivity parameter $\Delta > 0$. The numerical values are given in units of σ_{11}^8 . The error on the last significant figure is enclosed in parentheses.

negative for a given range of mole fractions that become deeper / wider for an increase in the Δ parameter.

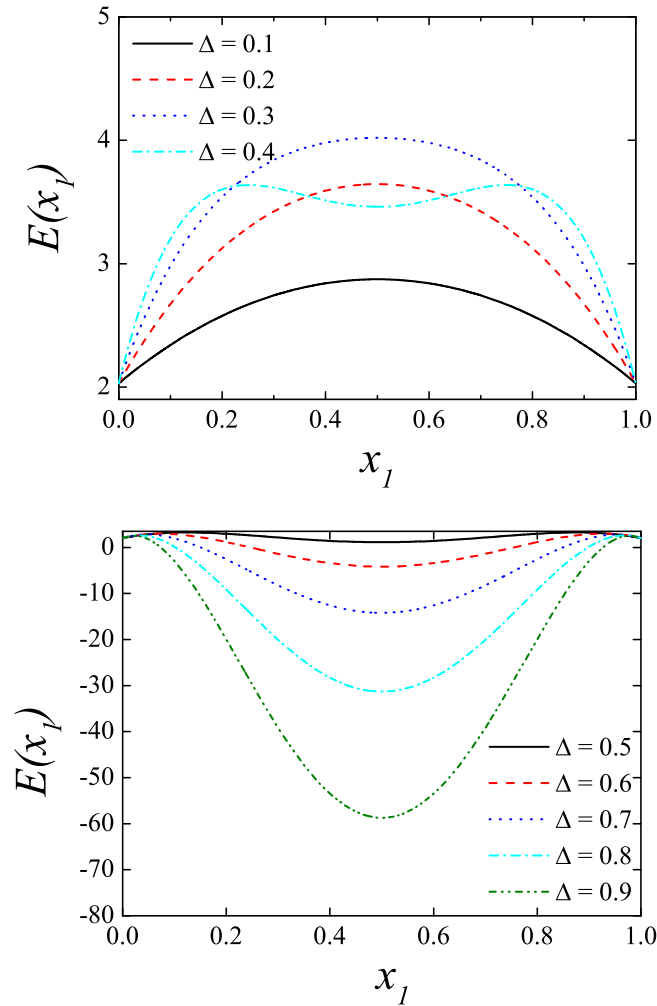


Figure 6.1: The fifth virial coefficient plotted as a function of the mole fraction for positive values of the nonadditivity parameter Δ .

In Figs. 6.2-6.6, the compressibility factor was plotted as a function of the packing fraction according to different values of mole fraction and Δ . As a general trend, we note that the rescaled EOS (RVE) provide the higher values for every considered value of Δ , and in general, they look very similar to each other for the low values of the nonadditivity parameter $\Delta \leq 0.2$. There is

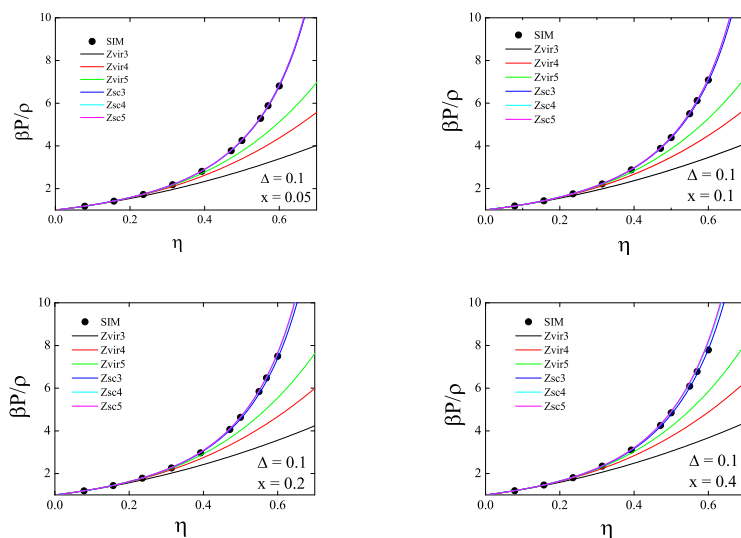


Figure 6.2: Compressibility factors as a function of the total packing fraction at different values of the Δ parameter and mole fraction x . Legend: SIM represents the NVT MC computer simulation; Zvir3 represents the virial expansion incorporating the first three virial coefficients; Zvir4 represents the virial expansion incorporating the first four virial coefficients; Zvir5 represents the virial expansion incorporating the first five virial coefficients; Zsc3 represents the scaled EOS incorporating the first three virial coefficients; Zsc4 represents the scaled EOS incorporating the first four virial coefficients; Zsc5 represents the scaled EOS incorporating the first five virial coefficients

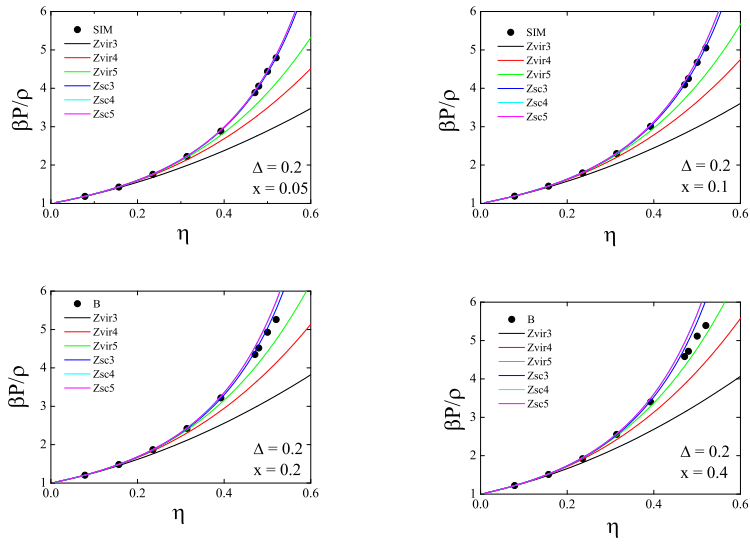


Figure 6.3: see Fig. 6.2

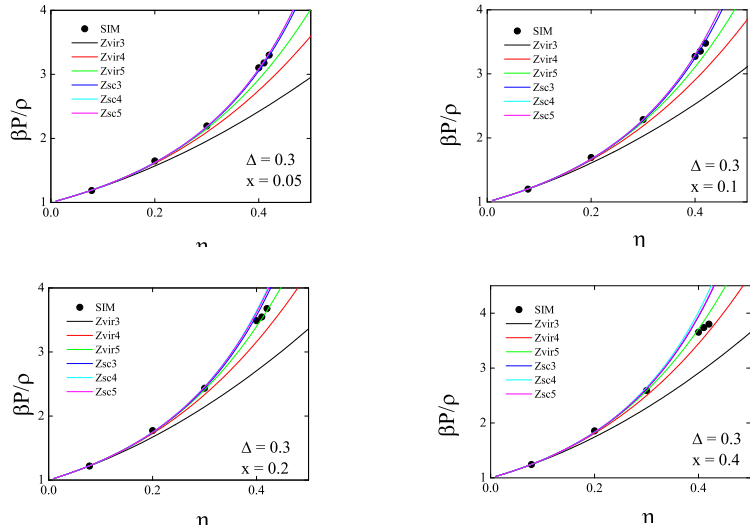


Figure 6.4: see Fig. 6.2

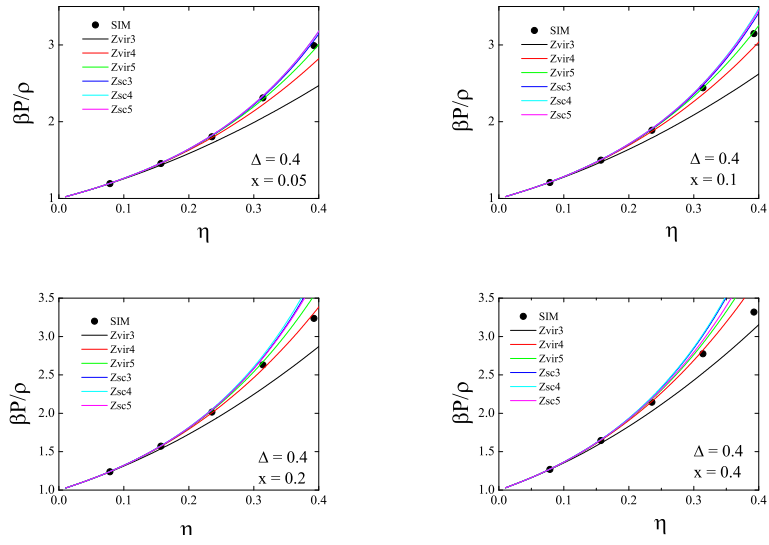


Figure 6.5: see Fig. 6.2

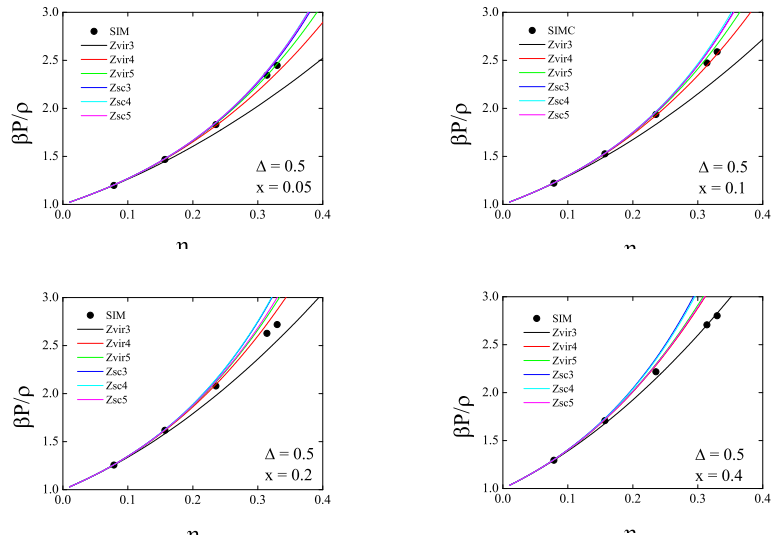


Figure 6.6: see Fig. 6.2

a moderate tendency of RVE to become slightly different by increasing the mole fraction, and also a non-monotonic behavior observed for the higher considered nonadditivity parameters, i.e. their predictions do not follow the series $Z_{sc3} < Z_{sc4} < Z_{sc5}$ (adding more virial coefficients to Eq. (6.1) does not necessarily bring to higher values of the compressibility factor Z), see for instance bottom panels of Figs. 6.4-6.6. It is interesting to note that for $\Delta \geq 0.3$ the predictions of Z_{sc5} are in better agreement with the exact MC result, which is a clear indication of a well-behaved convergence of the rescaled EOS when more virial coefficients are added to it. While this feature is somewhat expected and clearly shows how beneficial the rescaling procedure can be, this is still a non-trivial result due to the limitation of the RVE, which predicts an unphysical divergence of the compressibility factor when the total packing fraction becomes equal to 1. We argue that the reason of a clear emergence of well-behaved convergence of the RVE at the higher considered values of the nonadditivity parameter ($\Delta \geq 0.3$) is due to the fact that the binary mixture is found to be in a homogeneous state for smaller values of the packing fraction as compared to the cases where the nonadditivity parameter Δ is small (i.e. we are evaluating the RVE at quite smaller values of the packing fraction when Δ is increased). In fact, we note as a general rule that the critical packing fraction of the binary mixture tends to become smaller as the nonadditivity parameter is increased.

Now, it is interesting to assess the performance of the two schemes as compared to NVT MC computer simulation. At the lower values of the nonadditivity parameters $\Delta = 0.1, 0.2$ the virial EOS underestimates the MC EOS irrespective of the retained number of virial coefficients (see Figs. 6.2-6.3), while approaching the MC result monotonously, which means that Z_{vir5} is the most accurate one. Remarkably, for $\Delta = 0.1, 0.2$ all of the three rescaled EOS reproduce the MC EOS quantitatively. For $\Delta = 0.2$ the three rescaled EOS are still very accurate up to $x = 0.1$. Then, for the compositions closer to the equimolar one, they start to slightly overestimate the EOS at the higher densities (the higher the mole fraction, the larger the discrepancy). It is worth to note that even if all of the virial EOS underestimate the MC EOS, their predictions appear to improve when increasing the nonadditivity parameter and the mole fraction, so that Z_{vir5} reproduces the MC EOS better at $\Delta = 0.2$ than at $\Delta = 0.1$. This feature is a consequence of another effect:

the apparent shifting-up of the virial EOS predictions on increasing Δ and x . This effect can also be read as a progressive lowering of the MC EOS when increasing Δ and x , that makes the RVE predictions slightly overestimating the MC result.

The trend noted at $\Delta = 0.1 - 0.2$ persists when the nonadditivity parameter is increased to $\Delta = 0.3$, making $Z_{\text{vir}5}$ quantitative at $x = 0.2$, while at $x = 0.4$ the $Z_{\text{vir}4}$ EOS begins to approach the MC EOS (see Fig. 6.4). As a consequence, the MC EOS is located between $Z_{\text{vir}4}$ and $Z_{\text{vir}5}$, and $Z_{\text{vir}5}$ slightly overestimates the MC EOS at high packing fraction, whereas $Z_{\text{vir}4}$ is slightly underestimating it. The RVE predictions are still quantitative at the lower considered mole numbers $x = 0.05, 0.1$.

Then, at $\Delta = 0.4$, $Z_{\text{vir}5}$ becomes quantitative at $x = 0.1$, $Z_{\text{vir}4}$ becomes quantitative at $x = 0.2$, and the MC EOS is sitting between $Z_{\text{vir}4}$ and $Z_{\text{vir}3}$ for $x = 0.4$ at the high packing fraction (see Fig. 6.5). In this case, the RVE predictions are quantitative for the lowest mole number $x = 0.05$ only.

Finally, at $\Delta = 0.5$, $Z_{\text{vir}5}$ is predictive at the lowest composition $x = 0.05$, $Z_{\text{vir}4}$ becomes predictive at $x = 0.1$, $Z_{\text{vir}3}$ becomes predictive at $x = 0.4$, while at $x = 0.2$ the MC EOS sits in the middle between $Z_{\text{vir}3}$ and $Z_{\text{vir}4}$ (see Fig. 6.6). At this value of Δ , the RVE are clearly less predictive than the virial EOS, since even at low mole numbers they do not match the MC EOS profile.

The observed difficulty in finding a general trend arises because the convergence of the virial expansion is not well understood for binary mixtures. While for a pure system as e.g. the hard-sphere model, the virial coefficients are always positive and adding more of them to the virial expansion is expected to improve its convergence to the exact result, this in general does not hold true. In fact, as we showed in Fig. 6.1 for a binary mixture the virial coefficients do not necessarily get positive ones only, and this feature originates a non-monotonic convergence of the virial expansion to the exact result. In fact, it is no coincidence that the larger discrepancy for the virial expansions retaining more virial coefficients (i.e. $Z_{\text{vir}4} - Z_{\text{vir}5}$) is observed for the higher values of the nonadditivity parameter Δ , where the range of mole fractions for the negative values of $E(x_1)$ widens.

Now we have a look at the theoretical predictions for the fluid-fluid coexistence lines, which for a

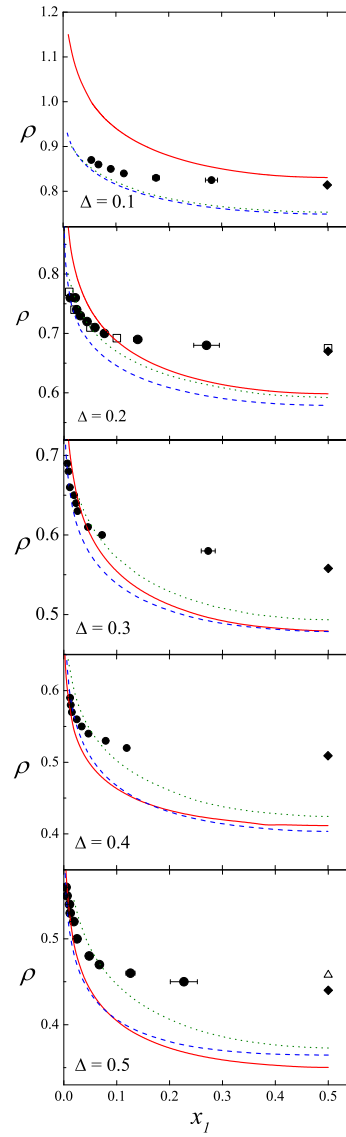


Figure 6.7: Phase coexistence boundary of a symmetric NAHD mixture for different values of Δ . In each panel the solid circles represent GEMC results and the diamond is the estimate of the critical density; the solid red line is the virial expansion truncated to the fifth order; the dashed blue line represents the rescaled virial expansion truncated to the fifth order [93]; the dotted green line is the prediction of the MIX1 implemented with the SPT equation of state for the reference fluid [81]; Open squares represent semigrand canonical Monte Carlo data [87].

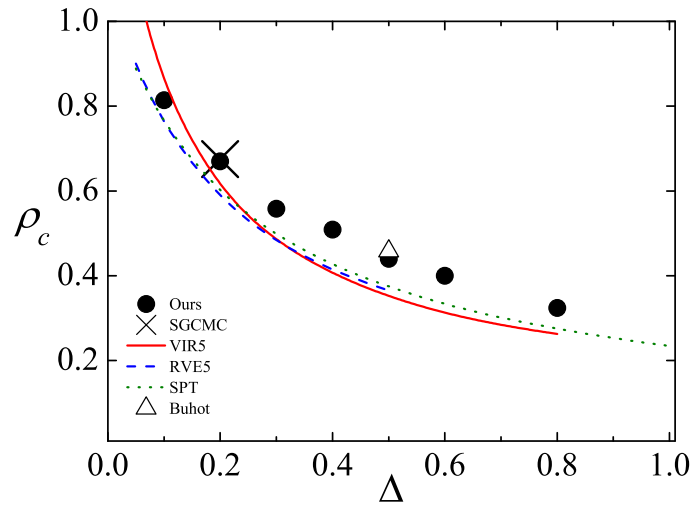


Figure 6.8: Critical density ρ_c plotted as a function of Δ for a symmetric NAHD mixture. The full circles are our GEMC simulations; the cross and the triangle represent the estimate of semigrand canonical ensemble MC simulations for $\Delta = 0.2$ [87] and the estimate of a cluster algorithm for $\Delta = 0.5$ [86], respectively. The solid red line and the dashed blue line are the predictions of the virial and the rescaled virial expansion truncated to the fifth order [93], respectively; The dotted green line is the prediction of the MIX1 implemented with the SPT equation of state for the reference fluid [81].

symmetric mixture are traced out just by examining the Helmholtz free energy. In fact, once the Helmholtz free energy is calculated by integrating the theoretical EOS according to Eq. (6.5), the binodal line for many Δ values can be calculated by using Eq. (6.6). In Fig. 6.7 the curves resulting from the virial expansion and the RVE approaches are shown. We also report the results obtained from a first-order perturbation theory, the so-called MIX1 approximation implemented with the SPT equation of state [76] of the pure fluid of hard-disks as a reference system [80, 81]. Actually, the SPT equation is not very accurate. There are available more accurate equations of state for the HD fluid [98, 99], but as a matter of fact their use does not seem to improve remarkably the theoretical estimates with respect to the simulation data. In order to avoid overburdening the figure with irrelevant information, we reported the virial expansion and RVE using the fifth virial coefficient only. An intricate scenario shows up: at $\Delta = 0.1$ (see top panel of Fig. 6.7), none of the theoretical approaches seem to be predictive, but the virial coexistence line on one side, and the RVE coexistence line/MIX1 on the other side, bracket the computer simulation GEMC data with the virial results overestimating, and the RVE/MIX1 underestimating them. At $\Delta = 0.2$ (see second panel from the top), theories generally tend to follow the GEMC data at mole fractions < 0.05 , with the exception of the virial binodal curve. Then, at $\Delta = 0.3 - 0.5$, both the virial and the RVE binodals tend to slightly overlap, while the MIX1 curve is always located at higher densities. In general, all of the considered theories tend to underestimate the critical density, and they can get quantitative only in the low composition regime. In order to better illustrate the ability of the different theoretical approaches to reproduce the critical density ρ_c of the mixture, we reported the latter as a function of the nonadditivity parameter explicitly in Fig. 6.8. Hence we clearly see that all of the theories tend to underestimate the GEMC critical density for $\Delta \geq 0.2$. However, for the lowest considered value of $\Delta = 0.1$ while the RVE and MIX1 binodals underestimate the computer simulation result, the virial expansion overestimates it. In Fig. 6.8, the GEMC predictions for the critical density are also compared with the available computer simulation results reported in the literature, including semi grand-canonical MC [87] and GEMC simulations based on a cluster algorithm [107].

6.4 Conclusion

The fifth virial coefficient of a symmetric mixture of hard-disks was numerically computed for a wide range of values of the nonadditivity parameter and the equation of state was built based on the virial expansion and on a resummation of the virial coefficients. Extensive Monte Carlo simulations were performed both in the Gibbs and canonical ensembles in order to estimate the fluid-fluid separation curves and the compressibility factors, respectively. Then, we used these numerical data to assess both the theoretical equations of state, and their predictions for the fluid-fluid phase coexistence. The agreement turned out to be reasonable good over the whole range of explored densities and concentrations for the equation of state, but not as satisfactory for the fluid-fluid binodals, especially in the proximity of the critical point.

Chapter 7

Bibliography

- [1] J. S. Rowlinson, *Liquids and liquid mixtures*, Butterworth, London, 1969.
- [2] J.A. Prins, *Physica*, **8**, 257-268, 1928
- [3] O.K. Rice, *Chem. Phys.*, **12**, 1-18, 1944
- [4] J.D. Bernal, The Bakerian lecture, 1962: The structure of liquids *Proc. R. Soc* , **280**, 299-322, 1964
- [5] N. Metropolis and A.W. Rosenbluth and M.N. Rosenbluth and A.N. Teller, and E. Teller *Chem. Phys.*, **21**, 1087-1092, 1953
- [6] J. P. Hansen and I. R. McDonald, *Theory of simple liquids* (Academic Press, London, 1976).
- [7] D. Costa, G. Pellicane, C. Caccamo, E. Scholl-Paschinger, and G. Kahl, *Phys. Rev. E* **68**, 021104 (2003).
- [8] C. Caccamo, G. Pellicane, and E. Enciso, *Phys. Rev. E* **56**, 6954 (1997).
- [9] P. Ballone, G. Pastore, G. Galli, and D. Gazzillo, *Mol. Phys.* **59**, 275 (1986).
- [10] A. Santos, M. L. de Haro, and S. B. Yuste, *J. Chem. Phys.* **122**, 024514 (2005).
- [11] J. Kalcher, J. C. F. Schulz, and J. Dzubiella, *J. Chem. Phys.* **133**, 164511 (2010).
- [12] S. Asakura and F. Oosawa, *J. Chem. Phys.* **22**, 1255 (1954).

- [13] M. Dijkstra, J. M. Brader, and R. Evans, *J. Phys.: Condens. Matter* **11**, 10079 (1999).
- [14] L. C. van den Bergh, J. A. Schouten, and N. J. Trappeniers, *Physica A* **141**, 524 (1987).
- [15] J. L. Barrat and W. L. Vos, *J. Chem. Phys.* **97**, 5707 (1992).
- [16] D. A. Zomick and J. L. Lebowitz, *Bulletin of the American Physical Society* **13**, 648 (1968).
- [17] J. L. Lebowitz and D. A. Zomick, *J. Chem. Phys.* **54**, 3335 (1971).
- [18] D. Gazzillo, *J. Chem. Phys.* **95**, 4565 (1991).
- [19] F. Saija, G. Pastore, and P. V. Giaquinta, *J. Phys. Chem. B* **102**, 10368 (1998).
- [20] F. Saija and P. V. Giaquinta, *J. Phys. Chem. B* **106**, 2035 (2002).
- [21] G. Pellicane, F. Saija, C. Caccamo, and P. Giaquinta, *J. Phys. Chem. B* **110**, 4539 (2006).
- [22] R. Fantoni and A. Santos, *Phys. Rev. E* **84**, 041201 (2011).
- [23] V. Ehrenberg, H. M. Schaink, and C. Hoheisel, *Phys. Rev. E* **84**, 041201 (2011).
- [24] H. Schaink, *Zeitschrift fur naturforschung section A-A journal of physical sciences* **48**, 889 (1993).
- [25] M. Al-Naafa, J. B. El-Yakubu, and E. Z. Hamad, *Fluid Phase Equilibria* **154**, 33 (1999).
- [26] G. Pellicane, C. Caccamo, P. Giaquinta, and F. Saija, *J. Phys. Chem. B* **111**, 4503 (2007).
- [27] A. Santos, M. L. de Haro, and S. B. Yuste, *J. Chem. Phys.* **132**, 204506 (2010).
- [28] A. H. Harvey and J. M. Prausnitz, *Fluid Phase Equilib.* **48**, 197 (1989).
- [29] P. Hopkins and M. Schmidt, *J. Phys.: Condens. Matter* **22**, 325108 (2010).
- [30] M. Schmidt, *Phys. Rev. E* **76**, 031202 (2007).
- [31] R. Roth, R. Evans, and A. A. Louis, *Phys. Rev. E* **64**, 051202 (2001).
- [32] A. Ayadim and S. Amokrane, *J. Phys. Chem. B* **114**, 16824 (2010).
- [33] R. Fantoni and A. Santos, *J. Chem. Phys.* **140**, 244513 (2014).

- [34] F. Jimenez-Angeles, Y. Duda, G. Odriozola, and M. Lozada-Cassou, *J. Phys. Chem. C* **112**, 18028 (2008).
- [35] O. Sierra and Y. Duda, *Physics letters A* **280**, 146 (2001).
- [36] G. Pellicane, C. Caccamo, D. S. Wilson, and L. L. Lee, *Phys. Rev. E* **69**, 061202 (2004).
- [37] W. Chen, *J. Chem. Phys.* **139**, 154712 (2013).
- [38] D. Gazzillo, *Mol. Phys.* **83**, 303 (1995).
- [39] M. Rovere and G. Pastore, *J. Phys.: Condens. Matter* **6**, A163 (1994).
- [40] R. Roth, R. Evans, and A. A. Louis, *J. Chem. Phys.* **118**, 7907 (2003).
- [41] W. Gózdź, *J. Chem. Phys.* **119**, 3309 (2003).
- [42] F. Saija, G. Fiumara, and P. V. Giaquinta, *J. Chem. Phys.* **108**, 9098 (1998).
- [43] M. Dijkstra, *Physical Review E*. **58**, 7523 (1998).
- [44] T. W. Melnyk and B. L. Sawford, *Mol. Phys.* **29**, 891 (1975).
- [45] R. E. Nettleton and M. S. Green, *J. Chem. Phys.* **29**, 1365 (1958).
- [46] C. Caccamo, *Phys. Rep.* **96**, 274 (1992).
- [47] Y. Rosenfeld and N. W. Ashcroft, *Phys. Rev. A* **20**, 1208 (1979).
- [48] Y. Rosenfeld and N. W. Ashcroft, *Phys. Rev.* **133**, A895 (1964).
- [49] F. J. Rogers and D. A. Young, *Phys. Rev. A* **30**, 999 (1984).
- [50] D. Henderson and P. J. Leonard, *Physical Chemistry: An Advanced Treatise* (vol VIII B, ed H. Eyring, D. Henderson and W. Jost, New York: Academic, 1971).
- [51] J. G. Amar, *Mol. Phys.* **67**, 739 (1989).
- [52] P. V. Giaquinta and G. Giunta, *Physica A* **187**, 145 (1992).
- [53] F. Saija, P. V. Giaquinta, G. Giunta, and S. P. Giarritta, *J. Phys: Condens. Matter* **6**, 9853 (1994).

- [54] F. Saija and P. V. Giaquinta, *J. Phys: Condens. Matter* **8**, 8137 (1996).
- [55] C. Caccamo and G. Pellicane, *J. Chem. Phys.* **117**, 5072 (2002).
- [56] J. Y. Jung, J. S. Jhon, and F. Ree, *J. Chem. Phys.* **102**, 1349 (1995).
- [57] J. A. Shouten, *Int. J. of Thermophys.*, 2001, **22**, 23.
- [58] E. Dickinson, *Mol. Phys.* **33**, 1463 (1977).
- [59] E. Dickinson, *Chem. Phys. Lett.* **66**, 500 (1979).
- [60] R. E. Pagano and N. L. Gershfeld, *J. Phys. Chem.*, 1972, **76**, 1238.
- [61] J. J. Gray and R. T. Bonnecaze, *Langmuir*, 2001, **17**, 7935.
- [62] D. D. Do, H. D. Do, and K. Kaneko, *Langmuir*, 2004, **20**, 7623.
- [63] D. Frenkel, *J. Phys.: Condens Matter*, 1994, **6**, A71.
- [64] T. Boublík and I. Nezbeda, *Collection Czechoslovak Chem. Commun.*, 1996, **51**, 2301.
- [65] F. Saija, G. Fiumara, and P. V. Giaquinta, *J. Chem. Phys.*, 1998, **108**, 9098.
- [66] J. A. Shouten, *Phys. Rep.*, 1989, **172**, 33.
- [67] C. C. Marti and B. J. Croset, *Surf. Sci.*, 1994, **318**, 229.
- [68] L. V. Yelash and T. Kraska, *Z. Phys. Chem.*, 1999, **211**, 159.
- [69] L. V. Yelash and T. Kraska, *Phys. Chem. Chem. Phys.*, 1999, **1**, 307.
- [70] Y. Duda and F. Vazquez, *Langmuir*, 2005, **21**, 1096.
- [71] M. Barcenas, P. Orea, E. Buenrostro-Gonzales, L. S. Zamudio-Rivera, and Y. Duda, *Energy Fuels*, 2008, **22**, 1917.
- [72] R. Faller and T. L. Kuhl, *Soft Materials*, 2003, **1**, 343.
- [73] R. Tenne and E. Bergmann, *Phys. Rev. A*, 1978, **17**, 2036.
- [74] R. J. Bearman and R. M. Mazo, *J. Chem. Phys.*, 1988, **88**, 1235.

- [75] R. J. Bearman and R. M. Mazo, *J. Chem. Phys.*, 1989, **91**, 1227.
- [76] R. J. Bearman and R. M. Mazo, *J. Chem. Phys.*, 1990, **93**, 6694.
- [77] V. Ehrenberg, H. M. Shaink and C. Hoheisel, *Physica A*, 1990, **169**, 365.
- [78] M. Al-Naafa, J. B. El-Yakubu, E. Z. Hamad, *Fluid Phase Equilibria*, 1999, **154**, 33.
- [79] E. Z. Hamad and G. O. Yahaya, *Fluid Phase Equilibria*, 2000, **168**, 59.
- [80] T. Melnyk and B. L. Sawford, *Mol. Phys.*, 1975, **29**, 891.
- [81] F. Saija and P. V. Giaquinta, *J. Chem. Phys.*, 2002, **117**, 5780.
- [82] A. Santos, M. Lopez de Haro, and S. B. Yuste, *J. Chem. Phys.*, 2010, **132**, 204506.
- [83] F. Saija, *Phys. Chem. Chem. Phys.* **13**, 11885 (2011).
- [84] P. Nielaba, *Int. J. of Thermophys.*, 1996, **17**, 157.
- [85] M. O. Ihm, F. Schneider, and P. Nielaba, *Progr. Colloid Polym. Sci.*, 1997, **104**, 166.
- [86] A. Buhot, *J. Chem. Phys.*, 2005, **122**, 024105.
- [87] L. Munoz-Salazar and G. Odriozola, *Mol. Simulat.*, 2010, **36**, 175.
- [88] F. Saija, G. Fiumara, and P. V. Giaquinta, *Mol. Phys.*, 1996, **87**, 991.
- [89] R. J. Wheatley, *Mol. Phys.*, 1998, **93**, 965.
- [90] R. J. Wheatley, *Mol. Phys.*, 1999, **96**, 1805.
- [91] J. S. Rowlinson and D. A. McQuarry, *Mol. Phys.*, 1987, **61**, 525.
- [92] A. Santos, S. B. Yuste, and M. Lopez de Haro, *Mol. Phys.* **96**, 1 (1999).
- [93] M. Baus and J. L. Colot, *Phys. Rev. A*, 1987, **36**, 3912.
- [94] J. L. Barrat, H. Xu, J. P. Hansen, and M. Baus, *J. Phys. C: Solid State Phys.*, 1988, **21**, 3165.
- [95] B. Barboj and W. N. Gelbart, *J. Chem. Phys.*, 1979, **71**, 3053; *J. Stat. Phys.*, 1980, **22**, 709.
- [96] D. Gazzillo, *J. Chem. Phys.*, 1991, **95**, 4565.

- [97] R. D. Mountain and A. H. Harvey, *J. Chem. Phys.*, 1991, **94**, (1991).
- [98] A. Mulero, I. Cachadina, and J. R. Solana, *Mol. Phys.*, 2009, **107**, 1457.
- [99] J. Tian, Y. Gui, and A. Mulero, *Phys. Chem. Chem. Phys.*, 2010, **12**, 5248.
- [100] C. H. Mak, *Phys. Rev. E*, 2006, **73**, 065104.
- [101] B. Břstnik, *Vestn. Slov. Kem. Drus.*, 1992, **39**, 145.
- [102] K. W. Kratky, *Physica A*, 1977, **87**, 584.
- [103] D. Frenkel and B. Smit, *Understanding Molecular Simulation*, (Academic Press, San Diego, 2001)
- [104] M. Matsumoto, T. Nishimura, *ACM Transactions on Modeling and Computer Simulation*, 1998, **8**, 3
- [105] A. Z. Panagiotopoulos, N. Quirke, M. Stapleton and D. J. Tildesley, *Mol. Phys.*, 1988, **63**, 527
- [106] A. Z. Panagiotopoulos, *Mol. Phys.*, 1987, **61**, 813
- [107] A. Buhot, *J. Chem. Phys.*, 2005, **122**, 024105.
- [108] M. Barošová, M. Malijeuský, S. Labík and W. R. Smith, *Mol. Phys.*, 1996, **87**, No. 2, 423
- [109] E. Lomba, M. Alvarez, L. L. Lee and N. G. Almarza *J. Chem. Phys.*, 1996, **104**, 4180

Appendix 1: Numerical integration

MC numerical integration was used to determine the coefficients $E_{\alpha\beta\gamma\delta\epsilon}$, in which each MC scheme consists of 4×10^{10} MC cycles. Since we are interested in evaluating the Mayer graph, we must produce an acceptable set of configurations according to the MC algorithm. The procedure was as follows: For a particle of say species α , fix it at the origin, then randomly place four other particles in a sequential manner such that the $(i+1)^{th}$ particle overlaps with the i^{th} particle ($i = 0, 1, 2, 3, 4$). This trial configuration that we have produced is an open chain of overlapping particles. If particle 5 and particle 1 overlap, and the residual cross-linked bonds are also retrieved (present in the calculated Mayer graph) and then we have a closed chain configuration and hence we call this a successful configuration. The ratio $\frac{N_s}{N_t}$ provides asymptotically the value corresponding to the cluster integral in relation to that of the open chain graph. Where (N_s) corresponds to the number of successful configurations and (N_t) is the total number of trial configurations. The accuracy of the MC, is dependent on the number of trail configurations and for the cluster integral J we have that

$$error = \left[\frac{J(J-1)}{N_t} \right]^{1/2}.$$

It is important to note that due to accumulating errors that are statistically independent, global uncertainty is greater than the error estimate for each specific cluster integral that makes up the expression for $E_{\alpha\beta\gamma\delta\epsilon}$. The number of moves in our MC runs is comparable with the period of the standard Fortran pseudorandom number generator (PRNG), namely 2^{32} . For this reason we decided to adopt the Mersenne Twister MT19937 pseudorandom number generator [104]. Some of the most interesting properties of MT19937 are: i) a very long period ($2^{19937} - 1$); ii) a very high equidistribution of points in spaces up to 623 dimensions and, iii) successful results in numerous tests for statistical randomness.

Appendix 2: Cluster integrals

Partition functions as well as particle densities are defined by multi-dimensional integrals over all the particle coordinates. Therefore it can be more desirable to conveniently represent these complex integrals as graphs or diagrams which then can be manipulated by theoretical-graph methods. It will be shown that this diagrammatic approach will lead to expansions of thermodynamic properties and particle distribution functions in powers of either the activity or density. Consider the case when the interparticle energy is the sum of the pair terms. If we write the Boltzmann factor in terms of Mayer functions $f(i, j)$, where

$$f(i, j) = \exp[-\beta\nu(i, j)] - 1 = e(i, j) - 1, \quad (7.1)$$

then as an example, we can consider an integral of the form ($N = 4$)

$$I = \int \int \int \int \left(\prod_{i=1}^4 z^*(i) \right) f(1, 2) f(1, 4) f(2, 3) f(3, 4) d2 d3 d4. \quad (7.2)$$

This is the sort of integral appearing in the definition of the particle density distributions. We can represent the above integral as a labeled diagram consisting of a number of circles linked by bonds, where the circles represent particle coordinates and have a specific label. We call these diagrams cluster diagrams and they contain two types of circles: white and black ones. The white circles are referred to as root points and correspond to coordinates held constant in the integration. The black circles are referred to as field points and represent the variables of integration. For a circle with the label i , we associate a function of coordinates $\gamma(i)$. We refer to these circles as a black or white γ -circles. If we have $\gamma = 1$, then we have a 1-circle. Bonds are drawn as lines between circles and with a bond between circles i and j we associate a function $\eta(i, j)$ and refer to it as a η -bond. When no pair of circles is linked by more than one bond we call it a simple diagram. The value of a labeled diagram is the value of the integral that the diagram represents. So if we were to represent Eq. (7.2) it would be as in Fig. (7.1). Since the black circles in the figure represent the dummy variables of integration, their labeling is irrelevant and therefore can be omitted. So an unlabeled diagram makes use of a combinatorial factor related to the topological structure of the diagram. This is explained as follows. Consider a cluster diagram constituting of m black γ -circles and any

number of white circles. Since there are m black circles, there are $m!$ possible permutations of the labels of the black circles and each one of these permutations leaves the values of the diagram unchanged. However there exists a subset of these permutations that are characterized by the same set of connections (circles labeled i and j in one diagram are linked by an η -bond if and only if they are similarly linked in the other). These diagrams are then said to be topologically equivalent.

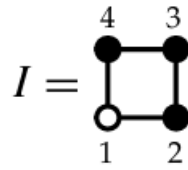


Figure 7.1: Cluster Diagram representing Eq. (7.2)

The coefficients E_{11112} and E_{11122} can be expressed by means of cluster integrals. Given that empty circles specify species 1 and full circles indicate species 2, the resulting two color graphs are the following:

$$E_{11122} = -\frac{1}{300V} \left[\begin{array}{ccccccccc} \text{Graph 1} & +60 & \text{Graph 2} & +60 & \text{Graph 3} & -120 & \text{Graph 4} & -120 & \text{Graph 5} & -120 \\ \text{Graph 6} & -60 & \text{Graph 7} & -60 & \text{Graph 8} & -120 & \text{Graph 9} & +120 & \text{Graph 10} & +120 \\ \text{Graph 11} & +60 & \text{Graph 12} & +120 & \text{Graph 13} & +120 & \text{Graph 14} & +60 & \text{Graph 15} & +60 \\ \text{Graph 16} & +60 & \text{Graph 17} & +30 & \text{Graph 18} & +60 & \text{Graph 19} & +60 & \text{Graph 20} & +30 \\ \text{Graph 21} & -60 & \text{Graph 22} & -60 & \text{Graph 23} & -30 & \text{Graph 24} & -60 & \text{Graph 25} & -60 \\ \text{Graph 26} & -30 & \text{Graph 27} & -30 & \text{Graph 28} & -30 & \text{Graph 29} & -15 & \text{Graph 30} & -30 \\ \text{Graph 31} & -30 & \text{Graph 32} & -15 & \text{Graph 33} & +20 & \text{Graph 34} & +20 & \text{Graph 35} & +10 \\ \text{Graph 36} & +20 & \text{Graph 37} & +20 & \text{Graph 38} & +10 & \text{Graph 39} & -10 & \text{Graph 40} & -30 \\ \text{Graph 41} & -60 & \text{Graph 42} & -10 & \text{Graph 43} & +30 & \text{Graph 44} & +60 & \text{Graph 45} & +10 \end{array} \right]$$

$$E_{111112} = -\frac{1}{150V} \left[\begin{array}{cccccc}
+60 & -60 & -120 & -120 & +60 & \\
\begin{array}{c} \text{Diagram 1} \\ \text{Diagram 2} \\ \text{Diagram 3} \\ \text{Diagram 4} \\ \text{Diagram 5} \end{array} & \begin{array}{c} \text{Diagram 6} \\ \text{Diagram 7} \\ \text{Diagram 8} \\ \text{Diagram 9} \\ \text{Diagram 10} \end{array} & \begin{array}{c} \text{Diagram 11} \\ \text{Diagram 12} \\ \text{Diagram 13} \\ \text{Diagram 14} \\ \text{Diagram 15} \end{array} & \begin{array}{c} \text{Diagram 16} \\ \text{Diagram 17} \\ \text{Diagram 18} \\ \text{Diagram 19} \\ \text{Diagram 20} \end{array} & \begin{array}{c} \text{Diagram 21} \\ \text{Diagram 22} \\ \text{Diagram 23} \\ \text{Diagram 24} \\ \text{Diagram 25} \end{array} & \\
+120 & +120 & +30 & +60 & +60 & \\
\begin{array}{c} \text{Diagram 26} \\ \text{Diagram 27} \\ \text{Diagram 28} \\ \text{Diagram 29} \\ \text{Diagram 30} \end{array} & \begin{array}{c} \text{Diagram 31} \\ \text{Diagram 32} \\ \text{Diagram 33} \\ \text{Diagram 34} \\ \text{Diagram 35} \end{array} & \begin{array}{c} \text{Diagram 36} \\ \text{Diagram 37} \\ \text{Diagram 38} \\ \text{Diagram 39} \\ \text{Diagram 40} \end{array} & \begin{array}{c} \text{Diagram 41} \\ \text{Diagram 42} \\ \text{Diagram 43} \\ \text{Diagram 44} \\ \text{Diagram 45} \end{array} & \begin{array}{c} \text{Diagram 46} \\ \text{Diagram 47} \\ \text{Diagram 48} \\ \text{Diagram 49} \\ \text{Diagram 50} \end{array} & \\
-30 & -60 & -60 & -15 & -30 & \\
\begin{array}{c} \text{Diagram 51} \\ \text{Diagram 52} \\ \text{Diagram 53} \\ \text{Diagram 54} \\ \text{Diagram 55} \end{array} & \begin{array}{c} \text{Diagram 56} \\ \text{Diagram 57} \\ \text{Diagram 58} \\ \text{Diagram 59} \\ \text{Diagram 60} \end{array} & \begin{array}{c} \text{Diagram 61} \\ \text{Diagram 62} \\ \text{Diagram 63} \\ \text{Diagram 64} \\ \text{Diagram 65} \end{array} & \begin{array}{c} \text{Diagram 66} \\ \text{Diagram 67} \\ \text{Diagram 68} \\ \text{Diagram 69} \\ \text{Diagram 70} \end{array} & \begin{array}{c} \text{Diagram 71} \\ \text{Diagram 72} \\ \text{Diagram 73} \\ \text{Diagram 74} \\ \text{Diagram 75} \end{array} & \\
-30 & +10 & +20 & +20 & -5 & \\
\begin{array}{c} \text{Diagram 76} \\ \text{Diagram 77} \\ \text{Diagram 78} \\ \text{Diagram 79} \\ \text{Diagram 80} \end{array} & \begin{array}{c} \text{Diagram 81} \\ \text{Diagram 82} \\ \text{Diagram 83} \\ \text{Diagram 84} \\ \text{Diagram 85} \end{array} & \begin{array}{c} \text{Diagram 86} \\ \text{Diagram 87} \\ \text{Diagram 88} \\ \text{Diagram 89} \\ \text{Diagram 90} \end{array} & \begin{array}{c} \text{Diagram 91} \\ \text{Diagram 92} \\ \text{Diagram 93} \\ \text{Diagram 94} \\ \text{Diagram 95} \end{array} & \begin{array}{c} \text{Diagram 96} \\ \text{Diagram 97} \\ \text{Diagram 98} \\ \text{Diagram 99} \\ \text{Diagram 100} \end{array} & \\
-30 & -20 & +30 & +20 & & \\
\begin{array}{c} \text{Diagram 101} \\ \text{Diagram 102} \\ \text{Diagram 103} \\ \text{Diagram 104} \\ \text{Diagram 105} \end{array} & \begin{array}{c} \text{Diagram 106} \\ \text{Diagram 107} \\ \text{Diagram 108} \\ \text{Diagram 109} \\ \text{Diagram 110} \end{array} & \begin{array}{c} \text{Diagram 111} \\ \text{Diagram 112} \\ \text{Diagram 113} \\ \text{Diagram 114} \\ \text{Diagram 115} \end{array} & \begin{array}{c} \text{Diagram 116} \\ \text{Diagram 117} \\ \text{Diagram 118} \\ \text{Diagram 119} \\ \text{Diagram 120} \end{array} & & \\
\end{array} \right]$$